UC San Diego
UC San Diego Electronic Theses and Dissertations

Title
Active Thermal Engineering using Nanostructures

Permalink
https://escholarship.org/uc/item/3812492v

Author
Shin, Sunmi

Publication Date
2019

Peer reviewed|Thesis/dissertation

UNIVERSITY OF CALIFORNIA SAN DIEGO

Active Thermal Engineering using Nanostructures

A dissertation submitted in partial satisfaction of the requirements
for the degree Doctor of Philosophy

in

Materials Science and Engineering

by

Sunmi Shin

Committee in charge:

 Professor Renkun Chen, Chair
 Professor Shengqiang Cai
 Professor Zhaowei Liu
 Professor Yu-Hwa Lo
 Professor Jeffrey Rinehart

2019

The Dissertation of Sunmi Shin is approved, and it is acceptable in quality and form for publication on microfilm and electronically:

_____

_____

_____

_____

Chair

University of California San Diego

2019

DEDICATION

Dedicated to my family for their unconditional love and supports.

TABLE OF CONTENTS

LIST OF FIGURES

ACKNOWLEDGEMENTS

My memories in San Diego are unforgettable and I believe the lessons I learned from them will make me a better person in my life. First of all, I greatly appreciate my advisor, Prof. Renkun Chen, who has always encouraged and believed me to be a sincere researcher. As much as he was a great PI who led multiple projects with his brilliant ideas, he was the best collaborator to me. It was my honor to be involved in ambitious research projects from my first year. I was surprised by his broad knowledge in general research areas that are not limited to his expertise. In addition, I could learn his honest and sincere attitude on research. He was an ideal example of an endless learner. During the past five years, I tried to knock his door almost every day and I very much appreciate the time he spent to mentor me and shared his honest comments. I could work on a very exciting topic, which constitutes the main part of this thesis, after long-lasting discussions for about six months. I cannot forget all the brainstorming steps until we made a final decision. After then, he gave me full supports to learn all the new things. In any single step of progress, there were unexpected hurdles, but he understood them as essential and inevitable challenges to overcome in research. His encouragement motivated me to proceed my topic with a strong belief in myself that I would be one of the experts as long as I invested my time and put effort into it. I enjoyed the scientific journey with his guidance. These discussion sessions, no matter how short or long they are, would become very precious moments in my research life. I believe it was the biggest fortune to have him as the advisor for my doctoral study.

I would also like to thank my collaborators and dissertation committee members. Dr. Ravi Prasher of Lawrence Berkeley National Laboratory guided me on coherent far-field

radiation study. He highly supported our collaboration. His great insight helped me develop the topic with an interesting physical picture as well as the support of optical modeling by his post doctor, Dr. Mahmoud Elzouka. I must acknowledge my collaborators who allowed me to characterize various interesting materials. Prof. Joseph Wang suggested ideas on screen-printing techniques.

I would like to thank Prof. Shengqiang Cai for his great ideas on soft matters. I appreciate his time for our collaborations. It was a great opportunity to broaden my research interests. He allowed me to measure the thermal property of bulk and nanostructured liquid crystal elastomers and hydrogels. I appreciate the help of his students and post doctor: Qiguang He who prepared polymer micro- and nanofibers with his extreme care, Yang Wang who fabricated hydrogels, Dr. Chi Hyung Ahn who synthesized bulk liquid crystal elastomers and Dr. Zhijian Wang who was very knowledgeable and had all the answers to my naive questions on polymers.

I also must thank Prof. Sheng Shen of Carnegie Mellon University who allowed me to measure high crystalline polymer nanofibers. It was a great opportunity to measure perfectly reversible phase change in the nanofibers provided by his student, Dr. Ramesh Shrestha. I appreciate every single material prepared by my collaborators. Thanks to them, I could learn different configurations of the measurement setup while modifying it for each sample. The experiences helped me to extend the capability of the measurement platform.

I would like to especially thank Prof. Zhaowei Liu who always had great and fresh ideas in the next directions. I appreciate our long discussions and the time that he showed his attention and interest. It was a great honor to get advice from him, and our collaboration led me to have more confidence in my research which had seemed to be never-ending. His

help and comments. As the first generation of our group members, they had built a great platform for junior students like me. I respect their sincere attitude in research and altruistic help to me. I enjoyed my research in the friendly-environment mixed with passions. Late night discussions in the lab and in the office gave me fresh moments to rethink, and I could learn many important skills that they had achieved from their experience. I also need to thank classmates and neighboring office mates, Dr. Shiteng Zhao, Dr. Mahmut Kavrik, Andy Zhao, and Prakrit Dhillon. I enjoyed our refreshing conversations with great enthusiasms in research. I also would like to thank my friends who encouraged me a lot, Yui Mikami, Woojoo Kim, Dayoung Kim, Kevin Lim, and Hanjoo Lee.

Finally, I would like to express my sincere thanks to my family for their support. They always believed me to be a good person, and pray for me. I must return their endless love.

I appreciate my collaborators allowing me to use the following publications in my dissertation:

Chapter 1, in part, is a reprint of the materials as they appears in S. Shin *et al*, "Role of Surfactant on Thermoelectric Behaviors of Organic-Inorganic Composites", *Journal of Applied Physics*, 123, 205106 (2018); S. Shin *et al.*, "High-Performance Screen-Printed Thermoelectric Films on Fabrics", *Scientific Reports*, 7, 7317 (2017); S. Shin *et al.*, "Hollow Photonic Structures of Transparent Conducting Oxide with Selective and Tunable Absorptance", Applied Thermal Engineering, 145, 416 (2018); S. Shin *et al.,* "Far-Field Coherent Thermal Emission From Polaritonic Resonance in Individual Anisotropic Nanoribbons", *Nature Communications*, 10, 1377 (2019); S. Shin *et al.*, "Plasmonically-Enhanced Thermal Radiation by Surface Phonon Polaritons"; S. Shin *et al.*, "Quasi-Ballistic

Polaritonic Heat Conduction: Shedding "Light" on Thermal Transport". The dissertation author was the primary investigator and the first author of the materials.

Chapter 2, in full, is a reprint of S. Shin, J. W. Roh, H.-S. Kim, R. Chen, "Role of Surfactant on Thermoelectric Behaviors of Organic-Inorganic Composites", *Journal of Applied Physics*, 123, 205106 (2018). The dissertation author was the primary investigator and the first author of the this paper.

Chapter 3, in full, is a reprint of S. Shin, R. Kumar, J. W. Roh, D.-S. Ko, H.-S. Kim, S. I. Kim, L. Yin, S. M. Schlossberg, S. Cui, J.-M. You, S. Kwon, J. Zheng, J. Wang, R. Chen, "High-Performance Screen-Printed Thermoelectric Films on Fabrics", *Scientific Reports*, 7, 7317 (2017). The dissertation author was the primary investigator and the first author of this paper.

Chapter 4, in full, is a reprint of S. Shin, S. Hong, R. Chen, "Hollow Photonic Structures of Transparent Conducting Oxide with Selective and Tunable Absorptance", Applied Thermal Engineering, 145, 416 (2018). The dissertation author was the primary investigator and the first author of this paper.

Chapter 5, in full, is a reprint of S. Shin, M. Elzouka, R. Prasher, R. Chen, "Far-Field Coherent Thermal Emission From Polaritonic Resonance in Individual Anisotropic Nanoribbons", *Nature Communications*, 10, 1377 (2019). The dissertation author was the primary investigator and the first author of this paper.

Chapter 6, in full, is currently being prepared for submission, S. Shin, R. Chen, "Plasmonically-Enhanced Thermal Radiation by Surface Phonon Polaritons". The dissertation author was the primary investigator and the first author of this paper.

Chapter 7, in full, is currently being prepared for submission, S. Shin, L. Chen, Z. Liu, R. Chen, "Quasi-Ballistic Polaritonic Heat Conduction: Shedding "Light" on Thermal Transport". The dissertation author was the primary investigator and the first author of this paper.

Sunmi Shin

San Diego, CA

June, 2019

VITA

2011	Bachelor of Science, Hanyang University
2014	Master of Science, Hanyang University
2019	Doctor of Philosophy, University of California San Diego

PUBLICATIONS

1. S. Shin, and R. Chen, "Plasmonically-Enhanced Thermal Radiation by Surface Phonon Polaritons" (To be submitted).

2. S. Shin, L. Chen, Z. Liu, and R. Chen, "Quasi-Ballistic Polaritonic Heat Conduction: Shedding "Light" on Thermal Transport" (To be submitted)

3. S. Shin, M. Elzouka, R. Prasher, and R. Chen, "Far-Field Coherent Thermal Emission from Polaritonic Resonance in Individual Anisotropic Nanoribbons", Nature Communications, 10:1377 (2019).

4. E. B. Rubin, S. Shin, Y. Chen, and R. Chen, "High-Temperature Stable Refractory Nanoneedles with over 99% Solar Absorptance", APL Materials, 7, 031101 (2019).

5. S. Shin, S. Hong, and R. Chen, "Hollow Photonic Structures of Transparent Conducting Oxide with Selective and Tunable Absorptance", Applied Thermal Engineering, 145, 416 (2018).

6. S. Shin, J. W. Roh, H.-S. Kim, and R. Chen, "Role of Surfactant on Thermoelectric Behaviors of Organic-Inorganic Composites", Journal of Applied Physics, 123, 205106 (2018).

7. M. Zebarjadi, G. Chen, Z. Ren, S. Shin, R. Chen, J. P. Heremens, B. Wiendlocha, H. Jin, B. Wang, and Q. Zhang, "Engineering of Materials", Book Chapter in 'Advanced Thermoelectrics: Materials, Contacts, Devices, and Systems', Taylor & Francis (2018).

8. S. Shin, R. Kumar, J. W. Roh, D.-S. Koh, H.-S. Kim, S. I. Kim, L. Yin, S. M. Schlossberg, S. Cui, J.-M. You, S. Kwon, J. Zheng, J. Wang, and R. Chen, "High-Performance Screen-Printed Thermoelectric Films on Fabrics", Scientific Reports, 7, 7317 (2017).

9. T. K. Kim, VanSaders, E. Caldwell, S. Shin, Z. Liu, S. Jin, and R. Chen, "Copper-alloyed spinel black oxides and tandem-structured solar absorbing layers for high-temperature concentrating solar power systems", Solar Energy, 132, 257 (2016).

10. M.-J. Park, J.-Y. Jung, S.-M. Shin, J.-W. Song, Y.-H. Nam, D.-H. Kim, and J.-H. Lee, "Photoelectrochemical oxygen evolution improved by a thin Al_2O_3 interlayer in a NiO_x/n-Si photoanode", Thin Solid Films, 599, 54 (2016).

11. J.-W. Song, Y.-H. Nam, M.-J. Park, S.-M. Shin, R. B. Wehrspohn, and J.-H. Lee, "Hydroxyl functionalization improves the surface passivation of nanostructured silicon solar cells degraded by epitaxial regrowth", RSC Advences, 5(49), 39177 (2015).

12. S.-M. Shin,* J.-Y. Jung,* M.-J. Park, J.-W. Song, and J.-H. Lee, "Catalyst-free hydrogen evolution of Si photocathode by thermovoltage-driven solar water splitting", Journal of Power Sources, 279, 151 (2015).
*Theses authors contributed equally to this work.

13. J.-W. Song, J.-Y. Jung, H.-D. Um, X. Li, M.-J. Park, Y.-H. Nam, S.-M. Shin, T.-J. Park, R. B. Wehrspohn, and J.-H. Lee, "Degradation mechanism of Al2O3 passivation in nanostructured Si solar cells", Advanced Materias Interfaces, 15, 1400010 (2014).

14. K.-T. Park,* S.-M. Shin,* A. S. Tazebay, H.-D. Um, J.-Y. Jung, S.-W. Jee, M.-W. Oh, S.-D. Park, B. Yoo, C. Yu, and J.-H. Lee, "Lossless hybridization between photovoltaic and thermoelectric devices", Scientific Reports, 3, 1 (2013).
*These authors contributed equally to this work.

15. S.-M. Shin, J.-Y. Jung, K.-T. Park, H.-D. Um, S.-W. Jee, Y.-H. Nam, and J.-H. Lee, "A novel wrap-around metal contact optimized for radial p-n junction Si wire solar cells", Energy & Environ. Sci., 6(6), 1756 (2013).

16. Y.-H. Nam, H.-D. Um, K.-T. S.-M. Shin, J.-W. Baek, M.-J. Park, J.-Y. Jung, K. Zhou, S.-W. Jee, Z. Guo, and J.-H. Lee, "Multi-layer Coating of SiO_2 Nanoparticles to Enhance Light Absorption by SI Solar Cells", J. Kor. Phy. Soc., 60, 1944 (2012).

17. S.-M. Shin, and J.-H. Lee, "Materials and Process Technologies of Silicon Solar Cells", Trends in Metals & Materials Engineering, the Korean Institute of Metals and Materials, 24, 8 (2011).

FIELD OF STUDY

Major Field: Engineering

Studies in Materials Science and Engineering

Professor Renkun Chen

ABSTRACT OF DISSERTATION

Active Thermal Engineering using Nanostructures

by

Sunmi Shin

Doctor of Philosophy in Materials Science and Engineering

University of California San Diego, 2019

Professor Renkun Chen, Chair

Active control of thermal transport is of significant interest for a wide range of applications, such as thermoregulation of individuals, buildings, vehicles and batteries, thermo-electric and solar-thermal energy conversion, bio/chemical sensing, and micro/nanomanufacturing. However, heat transfer processes are often difficult to actively control: heat conduction is usually diffusive in nature owing to the incoherence of heat carriers (phonons and electrons) and thermal radiation is generally broadband or have wide energy distribution. If one could engineer the transport of thermal energy, arguably the most

ubiquitous form of energy, with similar degree of controllability as electrical and optical energy, a variety of energy transport and conversion technologies can be improved or even revolutionized. This dissertation presents my work aiming to actively manipulate heat transport with multidisciplinary approaches, including thermo-electric and thermo-photonic engineering.

In the first part of my dissertation, I discuss the strategy for developing flexible thermoelectric materials, which can be used for active thermoregulation of individuals. The ongoing effort to reduce the energy consumption of climate control systems has mainly focused on the development of more efficient thermoregulation technologies. In particular, interests in personalized thermoregulation devices have inspired studies on high-performance flexible thermoelectric materials for integration with emerging wearable electronics. Towards this end, I have developed a generic screen printing strategy using nanostructured thermoelectric materials with optimized printing ink formulation, by considering and satisfying the complex requirements for the printability as well as electrical and thermal transport properties. I used two different approaches, 1) all-inorganic but printable inks and 2) organic-inorganic composite inks.

In the latter part, I introduce a thermo-photonic engineering approach to manipulate nanoscale heat transport by using surface phonon polaritons (SPhP). This dissertation mainly focuses on how the SPhP can be utilized to tailor thermal radiation properties, especially to achieve a coherent, near-monochromatic far-field thermal emission, which is a big departure from the classic textbook incandescent behavior as described by the Planck's law. The key feature of the design is to utilize nanoscale emitters whose dimension is comparable to or smaller than the thermal wavelength, a regime when the Planckian energy distribution no

longer holds (as Planck himself originally noted). Experimental and theoretical work quantify the far-field thermal radiation from these rationally-designed single nano-emitters.

Chapter 1

Multidisciplinary Active Thermal Engineering

1.1 Introduction

Heat dissipation has been an emerging issue along with rapid developments of high-performance electronics, daunting demands of computational power with big data, as well as the urgent needs for developing sustainable energy and environmental technologies. These diverse applications require understanding of individual operating environments and controllability of heat transport to meet such needs. Interdisciplinary concepts can expand the scope of enabling technologies by providing more flexibility of engineering. For instance, diffusive heat transport limits the invention of perfect thermal insulators and conductors, unlike photons and electrons with excellent controllability. It is an apparent drawback of thermal energy, compared to optical and electrical energy, although heat is the most ubiquitous form of energy. This dissertation introduces interdisciplinary methodologies for active thermal engineering, including thermo-electric engineering for energy conversion applications and thermo-photonic engineering for a novel concept of heat transfer with nanotechnology.

1.2 Thermo-Electric Engineering with Nanotechnology

The ongoing effort to reduce the energy consumption of climate control systems has mainly focused on the development of more efficient thermoregulation technologies. Typically cooling and heating represent the biggest part of residential and commercial building energy consumption in the United States and globally. Along the fact that traditional approaches to air conditioning the entire buildings waste substantial amount of energy, interests in personalized thermoregulation devices have been growing. It can deliver a precise thermal dose to target spots on individual and consequently reduce the cooling volume drastically. It also can be applied to enhance personal thermal comfort for outdoor activities and health care.

Thermoelectric (TE) devices have been considered as one of the promising approaches to realize compact and light-weight energy converters operated by electricity in solid-state. An electric current can cause an electrochemical potential change of charge carriers (i.e., electrons and holes) at the junctions of two different materials, so this thermo-electric phenomenon involves endothermic and exothermic reaction, so-called the Peltier effect. In short, the heat flux can be controlled by applying the electric current. However, the coefficient-of-performance (COP) of the TE devices has been far below that of the state-of-the-art refrigeration systems using vapor compression cycles, which is the most challenging issue to replace the traditional heat engine. The figure of merit (ZT) of the TE materials is determined by:

$$ZT = \frac{S^2 \sigma T}{\kappa} \qquad (1.1)$$

where S, σ, κ and T are Seebeck coefficient, electrical conductivity, thermal conductivity and temperature, respectively, and the COP is determined by:

$$COP = \left(\frac{T_c}{T_h - T_c} \right) \left(\frac{\sqrt{1 + ZT_m} - T_h/T_c}{\sqrt{1 + ZT_m} + 1} \right) \tag{1.2}$$

where T_c and T_h are temperature at the cold and hot sides and T_m is the average temperature $(= (T_h + T_c)/2)$. Since 1950s, the discovered compounds had showed ZT <1 over the five decades. The ZT of 1 corresponds to up to 17% of Carnot COP based on Eq. (1.2), where the existing vapor compression heat engines possess about 40% of Carnot COP. Even today, the commercial bulk TE devices still consist of materials with the ZT of around the unity.

To enhance the ZT value, electrically conductive but thermally insulated materials are preferred. However, the electronic and thermal transporting property is inherently interdependent in bulk materials. As a breakthrough, adopting nanostructures has been suggested to overcome the stagnant ZT value since the 2000s. For instance, low-dimensional materials such as nanowires, nanoparticles and superlattices have been suggested to achieve high power factor $(= S^2\sigma)$ and low thermal conductivity. The best material operating at room temperature is the nanostructured Bi_2Te_3 and its alloys. Using nanoscale dimensions effectively reduces the thermal conductivity while electronic property is unaffected. This is due to the distinct disparity in the mean free path between electrons (from 1 to 10 nm) and phonons (from 10 nm to 100s nm or even over 1 µm, dependent on the lattice property). Therefore, phonons can be preferentially scattered than the charge carriers. In this dissertation, low-dimensional Bi_2Te_3-alloy is used to develop efficient thermoelectric materials for personalized thermoregulation applications.

1.3 Thermo-Photonic Engineering with Nanotechnology

Classical heat transport by major heat carriers, electrons and phonons, in solids is governed by a diffusion process due to their short mean free paths (Λ). It impedes efficient thermal transmission, $\tau = \Lambda/(\Lambda + L)$, where L is a channel length connecting two thermal reservoirs. The upper limit of heat conduction per single mode, so-called quantum conductance ($G_0 = \pi k_B^2 T/6\hbar$) derived by Landauer formalism, can be achieved with ballistic transport. Although there have been a few attempts to observe the G_0, it only has been observed in the restricted system with a sufficiently long coherent length, such as either sub-Kelvin temperatures or atomic distances. Furthermore, under the limited conditions, only feeble amount of power can be involved, which prevents utilizing ballistic heat transport in the ubiquitous systems.

To overcome the diffusive nature of phonons with the short mean free path, this dissertation employs the coupled energy states of interdisciplinary carriers, photons (in free-space) and phonons (in solids) at the surface of polar dielectrics, so-called surface phonon polaritons (SPhPs). Electromagnetic waves in the IR regime can be resonated with the vibrating optical phonons when the resonance frequencies of the optical phonons are matched with the energy of photons. Efficient resonance requires a reflective surface where the real part of permittivity is negative with insignificant absorption loss, the nearly zero or relatively small imaginary prat. The regime can be described by characteristic frequencies, e.g., two optical phonon resonance frequencies in IR range for polar dielectrics. As phonons at room temperature (300 K) possess the thermal wavelength of ~10 μm, polar dielectric materials

with metallic behaviors in the IR regime close to 10 µm, such as SiO_2, SiC and h-BN have been considered as a promising candidate to study the influence of SPhPs on heat transfer.

The fact that the SPhPs can be excited in the selective spectral range within the Reststrahlen band, and also the energy dispersion is highly localized along the surface by forming an evanescent surface wave, allows higher tunability of thermal property by selecting different materials and designing structures. The coupling converts incandescent background thermal energy into a coherent source guided along the surface, which creates a novel approach to control the heat as light energy. It promises a feasibility of ballistic heat conduction in broad applications under various ambient temperatures, but experimental observation has yet to be explored.

This phenomenon blurs the boundary of radiation and conduction. The nature of radiation leads to wide spatial energy distribution which is not restricted by the physical size of a conductor, while the nature of conduction guides the thermal energy along the surface of medium. The existence of SPhPs can be controlled by modulating the optical property of the surrounding or heat carrying channel itself, so as to tune the thermal transport, which is otherwise very difficult, if not impossible, to achieve within the diffusive thermal transport paradigm.

More interestingly, heat transfer mediated by SPhP is expected to be more important at high temperature, similar to radiation heat transfer. Therefore, the polaritonic thermal transport phenomena could be used for thermal management of a wide range of high-temperature electronic devices such as laser diodes, light emitting diodes (LEDs), and high-power inverters, which are increasingly more widely used in many industries such as defense, aerospace, and energy.

1.4   Organization of the Thesis

The first part of this dissertation (Chapter 2) details a methodology of developing high-efficient TE inks using hybrid organic-inorganic materials. The hybrid composites have recently attracted intensive interests as a promising candidate for flexible TE devices using inherently soft polymers as well as for increasing the degree of freedom to control TE properties. Experimentally, however, enhanced TE performance in hybrid composites has not been commonly observed, primarily due to inhomogeneous mixing between the inorganic and organic components which leads to limited electrical conduction in the less conductive component and consequently a low power factor in the composites compared to their single-component counterparts. This study investigated the effects of different surfactants on the uniformity of mixing and the TE behaviors of the hybrid composites consisting of $Bi_{0.5}Sb_{1.5}Te_3$ (BST) and poly(3,4-ethylenedioxythiophene) polystyrene sulfonate (PEDOT:PSS). Compared to dimethyl sulfoxide, which is the most commonly used surfactant, Triton X-100 (TX-100) can lead to homogenous dispersion of BST in PEDOT:PSS. By systematically studying the effects of the surfactant concentration, we can attribute the better mixing capability of TX-100 to its non-ionic property, which results in homogenous mixing with a lower critical micelle concentration. Consequently, simultaneous increase in electrical conductivity and Seebeck coefficient in the BST/PEDOT:PSS composites was observed with the TX-100 surfactant.

In addition to the hybrid organic/inorganic TE inks discussed in Chapter 2, the next section (Chapter 3) details the fabrication and thermoelectric characterization of the high-performance printed thermoelectric (TE) films with all-inorganic inks. Printing techniques

could offer a scalable approach to fabricate thermoelectric devices on flexible substrates for power generation used in wearable devices and personalized thermo-regulation. However, typical printing processes need a large concentration of inactive binder additives, which often render a detrimental effect on electrical transport of the printed TE layers. Here, this dissertation introduces scalable screen printing of TE layers on flexible fiber glass fabrics, by rationally optimizing the printing inks consisting of TE particles (p-type $Bi_{0.5}Sb_{1.5}Te_3$ or n-type $Bi_2Te_{2.7}Se_{0.3}$), binders, and organic solvents. A suitable binder additive, methyl cellulose, was identified, which offers suitable viscosity for printability at a very small concentration (0.45–0.60 wt.%), thus minimizing its detrimental impact on electrical transport. Following printing, the binders were subsequently burnt off via sintering and hot pressing. We found that the nanoscale defects left behind after the binder burnt off became effective phonon scattering centers, leading to low lattice thermal conductivity in the printed n-type material. With the high electrical conductivity and low thermal conductivity, the screen-printed TE layers showed high room-temperature ZT values of 0.65 and 0.81 for p-type and n-type, respectively.

Chapter 4 deals with optically-engineered thermal radiation. Hollow 3D structures of transparent conducting oxides (TCO) were adopted for efficient emission control. TCO has high transmittance in the solar spectrum and tunable optical properties in the infrared regime due to their plasmonic property. The IR emissivity can be further adjusted by the geometry. Here, using solid and hollow triangles as an example, the spectral absorptance of 3D TCO structures was modeled with various carrier concentrations and geometrical factors. It was shown that hollow triangular structures enhance the spectrally selective absorption, namely, high emittance in IR and low absorptance in the solar spectrum. This is because the large

primary sizes of the triangles can interact strongly with the longer wavelength mid-IR while the small wall thickness of the hollow structures reduces the overall absorption volume for the shorter wavelength light in the near-IR and visible regimes. Further, by changing their angles, the hollow features can be used to tune the IR emissivity within a large range (from 0.14 to 0.8). The selective and tunable absorptance of 3D hollow structures of TCO may find applications in passive radiative cooling, solar thermal absorbing, and tunable windows glazing.

Next (Chapter 5 and 6), the first experimental attempt to employ heat transfer measurement to study the contributions of SPhPs in a single nano-object is discussed. Coherent thermal emission deviates from the Planckian blackbody emission with a narrow spectrum and strong directionality. While far-field thermal emission from polaritonic resonance has shown the deviation through modelling and optical characterizations, an approach to achieve and directly measure dominant coherent thermal emission has not materialized. By exploiting the large disparity in the skin depth and wavelength of surface phonon polaritons, anisotropic SiO_2 nanoribbons can be designed to enable independent control of the incoherent and coherent behaviors, which exhibit over 8.5-fold enhancement in the emissivity compared with the thin-film limit. Importantly, this enhancement is attributed to the coherent polaritonic resonant effect, hence, was found to be stronger at lower temperature. A thermometry platform is devised to extract, for the first time, the thermal emissivity from such dielectric nanoemitters with nanowatt-level emitting power. The result provides new insight into the realization of spatial and spectral distribution control for far-field thermal emission. In Chapter 6, this dissertation further develops the methodology

shown in Chapter 5 to expand its applications in more complicated emitter structures, for instance, Au particles on SiO_2 nanoribbons with unknown thermal conductivity.

The last section, Chapter 7, deals with an experimental investigation of SPhPs contributions to heat conduction. The low loss property of SPhPs can lead to distinguishable long mean free path, even at the centimeter scale, with highly confined energy along the surface. Unlike the fact that optical phonons by themselves rarely deliver thermal energy due to their negligible group velocity, SPhPs can be effective heat carriers with light-like energy dispersion. To experimentally investigate heat transport by SPhPs, structures exhibiting distinct thermal conductance by SPhPs needs to be designed, out of other mechanisms through phononic conduction and radiation. Highly anisotropic SiO_2 nanowires were fabricated with narrow cross-section (50 nm and 250 nm in thickness and width, respectively). The controlled length covers the window to observe dominant contributions by SPhPs. With the minimized parasitic conduction, we studied length-dependent apparent thermal conductance. It showed a length-independent behavior measured up to 300 μm length, implying longer mean free path than the sample length. This work, as the first demonstration of non-diffusive heat conduction mediated by SPhPs, could pave the way for active manipulation of thermal energy using surface waves.

Acknowledgements

Thermoelectric Films on Fabrics", *Scientific Reports*, 7, 7317 (2017); S. Shin *et al.*, "Hollow Photonic Structures of Transparent Conducting Oxide with Selective and Tunable Absorptance", Applied Thermal Engineering, 145, 416 (2018); S. Shin *et al.,* "Far-Field Coherent Thermal Emission From Polaritonic Resonance in Individual Anisotropic Nanoribbons", *Nature Communications*, 10, 1377 (2019); S. Shin *et al.*, "Plasmonically-Enhanced Thermal Radiation by Surface Phonon Polaritons"; S. Shin *et al.*, "Quasi-Ballistic Polaritonic Heat Conduction: Shedding "Light" on Thermal Transport". The dissertation author was the primary investigator and the first author of the materials.

Chapter 2

Role of Surfactant on Thermoelectric Behaviors of Organic-Inorganic Composites

2.1 Introduction

There is an increasing interest in hybrid organic-inorganic thermoelectric (TE) materials for flexible devices to be integrated into wearable electronics.[1-3] Inorganic components are typically rigid and their performance and reliability could be compromised by thermal stress. Therefore, using inherently soft polymers could help achieve flexibility while still sustaining high performance by the inorganics.[3-9] In addition, employing the hybrid could lead to novel properties not available in the constituent materials, as the intrinsic properties of a given material tend to have relatively small variations, such as crystallographic structures, energy level distribution, etc.[1-3,10-14] Composite property can be generally determined using the rule-of-mixtures based on the effective medium theory, where the hybrid property is assumed to have an averaged value of the individual constituents.[15,16] However, interestingly, there have been studies showing that interfacial interactions contribute to distinguishable properties, by considering the interface or boundary as a separate phase.[17,18] It implies that the combination of two dissimilar materials has the potential to greatly enhance the controllability of the material properties. For TE application,

this system allows selective control of often conflicting parameters, e.g., thermal and electrical transport.[9,19] For example, introducing interfaces across the boundary between two different phases will limit phonon transport by boundary scattering.[20] The disparity in length scales, i.e., mean free path, between charge carriers and phonons enables preferential scattering of phonons without significantly affecting charge transport.[21-23] Especially, hybrid systems with highly mismatched acoustic impedance as in soft organic and hard inorganic components also have the potential to possess ultralow thermal conductivity due to the thermal boundary resistance.[24] Furthermore, hybrid organic/inorganic composites provide an opportunity for enhanced TE performance by taking the advantages of low thermal conductivity and high Seebeck coefficient (S) from the organic and inorganic components, respectively.[3-7,25,26]

Despite the relative simplicity of this concept, it has been rare to achieve high TE performance in hybrid organic/inorganic TE materials. In particular, most studies that demonstrated high TE performance often employed special sample preparation techniques rather than simple mixing of the constituent materials. For instance, Wan *et al.*[3] electrochemically intercalated hexylammonium (HA) and dimethyl sulfoxide (C_2H_6OS, or more commonly known as DMSO) into TiS_2 single crystals and formed $TiS_2[(HA)_x(H_2O)_y(DMSO)_z]$ hybrid superlattice, which exhibited a high n-type power factor of 450 $\mu W/m\text{-}K^2$. Zhang *et al.*[27] demonstrated high power factor exceeding 100 $\mu W/m\text{-}K^2$ in Bi_2Te_3 and poly(3,4-ethylenedioxythiophene) polystyrene sulfonate (PEDOT:PSS) where the inorganic and organic materials were deposited layer-by-layer. Yee *et al.*[2] achieved high power factor in Te nanowires /PEDOT:PSS where the PEDOT:PSS was polymerized in the solution with Te nanowires. However, simple physical mixing of the organic and inorganic

components, which would provide a more facile and generic fabrication process for a wide range of materials, has often resulted in relatively low power factor ranging from 2.86 μW/m-K^2 to 47.70 μW/m-K^2, which is mostly due to the low S.[11,12,22,28-31]. However, the exact reasons behind these relatively low power factor values were not thoroughly studied in these reports.

We hypothesized that the low performance in the physically mixed hybrid TE materials could be attributed to phase separation between the organic and inorganic components, where different phases from the composite mixture are not uniformly distributed. Specifically, if the two materials are not homogeneously mixed, the charge transport would be dominated by the more conducting phase, which is the conducting polymer in the case of $Bi_{0.5}Sb_{1.5}Te_3$ (BST)/PEDOT:PSS, leading to a low S and power factor that are characteristics of polymers[11,22,28]

To test our hypothesis, we systematically studied the homogeneity of the mixture of p-type PEDOT:PSS and BST and its impact on TE transport by varying the types and concentrations of surfactants. We chose BST and PEDOT:PSS, the most commonly used room-temperature inorganic and organic TE materials, respectively. Also, the ionization energy of BST (5.3 eV) is similar to the work function of PEDOT:PSS (5.2 eV)[32,33], yielding a small energy barrier at their interface. Conduction among PEDOT:PSS is mediated by phonon-assisted hopping that requires an activation energy due to the localized carriers within the backbones of PEDOT, where conductive PEDOT grains are surrounded by PSS.[34,35] PSS is an insulator but it is required to dope EDOT, the monomer of PEDOT, as an oxidizing agent during the polymerization process of EDOT as well as render PEDOT processability in water owing to the hydrophilicity of PSS.[34] The presence of PSS increases

the energy barrier between neighbouring PEDOT chains. Therefore, effective phase separation of PEDOT and PSS and removal of excess PSS are the keys to enhance electrical property of PEDOT:PSS.[36]

DMSO has been widely used as a surfactant to enhance the conductivity of PEDOT:PSS [37]. As an ionic surfactant, DMSO induces phase separation between PEDOT and PSS, resulting in the rearrangement between the conducting PEDOT and insulating PSS chains.[38-40] Negatively charged DMSO, $(CH_3)_2$-S=O$^-$, repulses PSS molecules against PEDOT, and makes larger grains of PEDOT groups, which is more conductive. It is a common process to add DMSO of about 5 wt.% to PEDOT:PSS to achieve a σ of ~1000 S/cm.[38-40]

DMSO has also been widely used as the surfactant for composites consisting of PEDOT and BST composites [11,22,28] or other inorganic TE materials [10,12,31]. Due to its strong ionicity, DMSO could also lead to phase separation between PEDOT:PSS and BST in the hybrid composites, , as shown schematically in Fig. 2.1(a) and (b). However, the influence of the ionic DMSO surfactant on the degree of mixing in the PEDOT:PSS/BST composites has not been studied, nor has there been any report suggesting an alternative surfactant.

In this work, we aim to elucidate the electrical and thermoelectric transport mechanisms in the widely studied organic/inorganic PEDOT:PSS/ BST composites, and to understand how the iconicity of the surfactants can impact the mixing and consequently the thermoelectric transport properties. Specifically, we studied ionic surfactant DMSO and an nonionic counterpart, Triton X-100 (TX-100, or $(C_{14}H_{22}O(C_2H_4O)_n$, where n=9 or 10). We found that DMSO can indeed lead to heterogeneous mixing and phase separation, and consequently a low Seebeck coefficient and power factor, whereas TX-100 led to a more

homogenous mixing and significantly enhanced Seebeck coefficient and power factor in the physically mixed composites of PEDOT and BST.
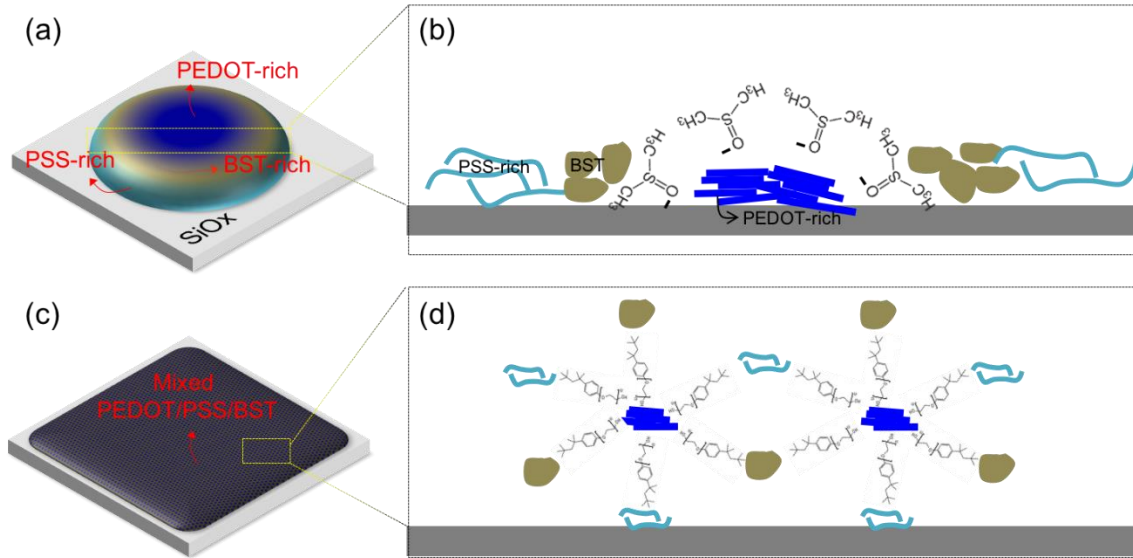
Figure 2.1   Schematics of (a) drop-casted PEDOT:PSS/ BST and (b) a zoomed side view of the dispersions with DMSO, and (c) drop-casted PEDOT:PSS/BST and (d) a zoomed side view of the dispersions with Triton X-100 (TX-100).

2.2   Experimental

BST particles were fabricated using a spark erosion process, as shown in supplementary Figs. 2.3 & 2.4 and described in our prior publications [41,42]. The starting bulk BST pellets, from which the particles were made, have has a power factor of about 40 μW/cm-K^2 and thermoelectric figure of merit (ZT) of about 0.8.[42] The composition of the spark-eroded particles was confirmed to be the same as the staring pellets, namely, $Bi_{0.5}Sb_{1.5}Te_3$, as analyzed by Energy dispersive X-ray (EDX, supplementary Figure 2.5) and X-Ray Diffraction (XRD, supplementary Fig. 2.6). The particles were subsequently rinsed

15

with 5 vol.% of hydrochloric (HCl) acid solution in deionized (DI) water to remove surface oxides. The particles (60 wt.%) were then mixed with PEDOT:PSS (CLEVIOS PH1000) and either types of the surfactants (DMSO or TX-100). The solution was then sonicated for 15 mins and ball milled for 12 hours for thorough mixing. It was then drop-casted onto Si wafers covered with a thin thermal SiO_2 layer.   Finally, the sample was cured at room temperature under vacuum. The vacuum curing was used in order to avoid delamination induced by rapid solvent evaporation that would have occurred if high temperature curing were used. This procedure typically resulted in films of tens of micron thick. To improve σ, the drop-casted films were rinsed with a polar solvent, methanol, to wash out excess amount of PSS and to increase the ratio of PEDOT to PSS.

The degree of mixing between PEDOT:PSS and   BST was evaluated based on the SEM images, as shown in Fig. 2.2(a-e). Furthermore, EDX mapping of S and Te element was use to further illustrate the uniformity of the distribution of BST in PEDOT:PSS (Fig. 2.2(f) and (g)). Additionally, AFM imaging was carried out to show the homogeneity of the mixing in the TX-100 samples.

The influence of the surfactant concentration was studied from the critical micelle concentration (CMC) and electrical conductivity (σ) measurement. The CMC was determined from the contact angle measurements and was defined as the surfactant concentration at which the contact angle drops sharply.[43] σ was measured using the van der Pauw method as a function of the weight fraction of the surfactant of either DMSO and TX-100, as shown in Fig. 2.11(e) and (f). The exact thickness of the films was measured by a film surface profiler (Dektak 150). Furthermore, σ at varying temperatures was measured

to determine the slopes of σ *vs.* temperature ($d\sigma/dT$), which is shown in Supplementary Fig. 2.10.
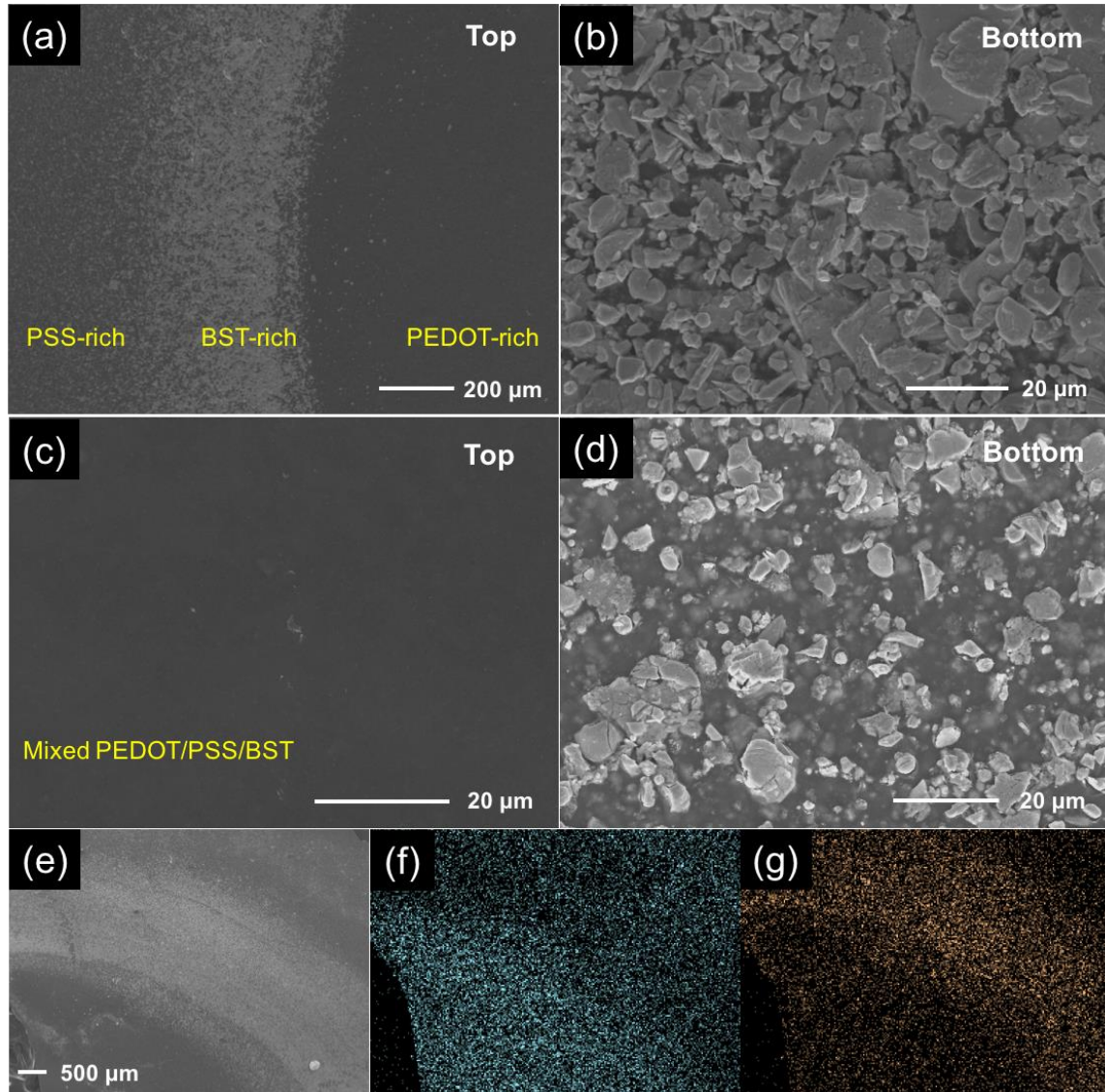
Figure 2.2   SEM images of (a) top surface and (b) bottom surface of PEDOT:PSS/ BST with DMSO (5wt%), and (c) top surface and (d) bottom surface of PEDOT:PSS/ BST with TX-100 (1wt%). (e) SEM image (top view) (f) EDX mapping of S element and (g) EDX mapping of Te element with DMSO.

Seebeck coefficient (S) of the thin film samples were measured using a custom-made setup. A sample (hybrid film coated on a substrate) was placed between two thermoelectric devices, with one heating and the other cooling to generate a temperature gradient along the sample. Two pairs of T-type thermocouples, approximately 8 mm apart, were used to measure the temperature difference (ΔT) between the hot and cold sides of the sample, while the Cu probes of the same thermocouples were used to measure the voltage (ΔV) (Supplementary Fig. 2.8). During the measurements, the ΔT was swept from 0 to ~10 K, and the S was determined from the slope of ΔV vs. ΔT. For polymer based thermoelectric films that have low thermal conductivity, we found that extreme care must be taken to avoid non-negligible heat leakage from the sample to the thermocouple probes, which would cause discrepancy between the measured temperature and the real temperature at the voltage probes and consequently a systematic error in the measured S. We have eliminated this error source by using fine (70 µm wire gauge) thermocouple probes, high thermal conductivity substrates (Si wafer covered with a thin SiO_2 layer), and high conductivity eutectic InGa solder. We also calibrated our setup by measuring the S of pure BST particles and pure PEDOT:PSS (Fig. 2.9).

2.2.1 Particle Preparation: Spark Erosion Process

Spark erosion is a method producing fine powders from metals, semiconductors and alloys. In the spark-erosion system, a charged capacitor is attached to two electrodes, which are made of the same material with charges (starting material) to generate sparks by applying an electrical field larger than the dielectric breakdown field of the gaps between two chunks

of the material. The entire system including the electrodes and the charges is immersed in a dielectric liquid, which was liquid nitrogen in this study to avoid oxidation of BST, as shown in Fig. 2.3. This process involves repetitive spark discharges among chunks, leading to extremely high temperature (i.e. 10000 K). The molten droplets or vaporized material caused by the spark discharge are frozen in the dielectric liquid, yielding the production of fined particles. Furthermore, 'shaker-pot' was utilized by adopting a vibrating motor in order to enhance the production rate, by continually providing gaps between the neighboring charges and/or between the charge and electrode. Here, a 10-cm diameter spark erosion cell was mounted in a double walled, vacuum-jacketed glass container that holds the dielectric liquid, so as to avoid breakage of the glass container due to huge difference in temperature between the air and dielectric liquid. As particles were produced, they drifted down through the screen to be collected at the bottom of the container, as shown in Fig. 2.3(d). Spark-eroded particles had a broad range of sizes from nm to μm scales.
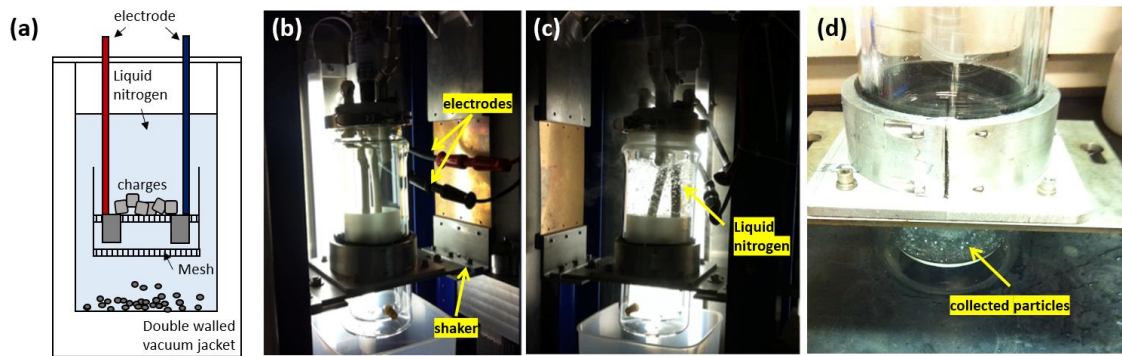
Figure 2.3   Spark erosion apparatus. (a) Schematic of the spark erosion apparatus. (b) Two electrodes of the cell in the shaker-pot are connected to the electrodes for pulsed power and the shaker-pot is placed on a motor driver shaker. (c) Liquid nitrogen is filled in the shaker-pot. (d) An optical image of spark-eroded BST powders on the bottom of the shaker-pot after 30 min. operation of the spark erosion process.
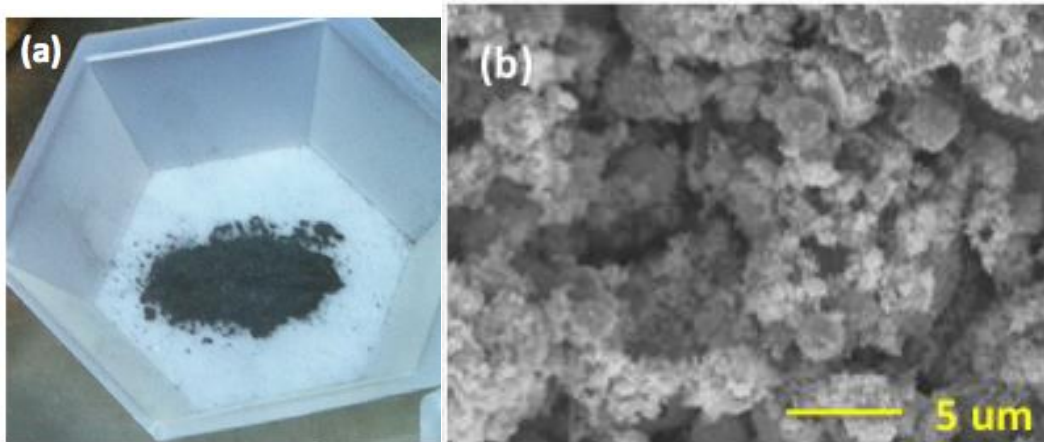
Figure 2.4   (a) Photograph of BST particles after sieving through 45 μm mesh. (b) SEM image of the same powders.
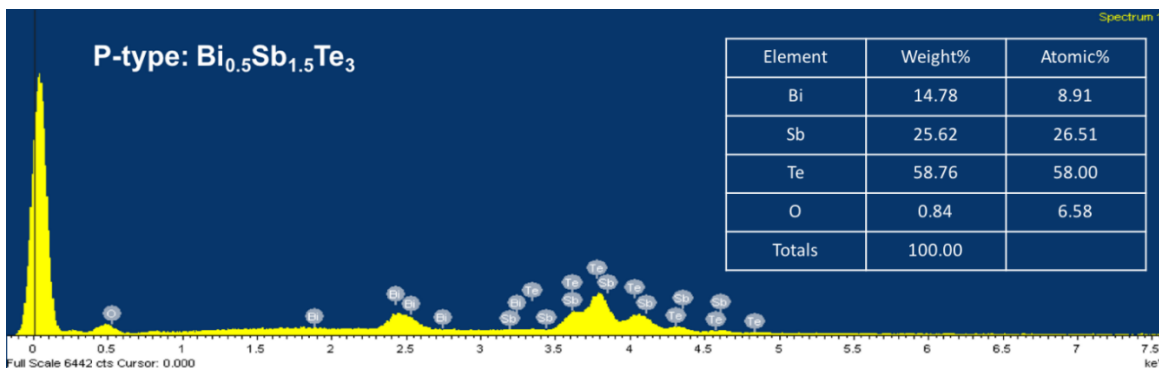
Figure 2.5　Energy dispersive x-ray (EDX) analysis of spark-eroded BST powders showing that the composition was the same as the bulk value.
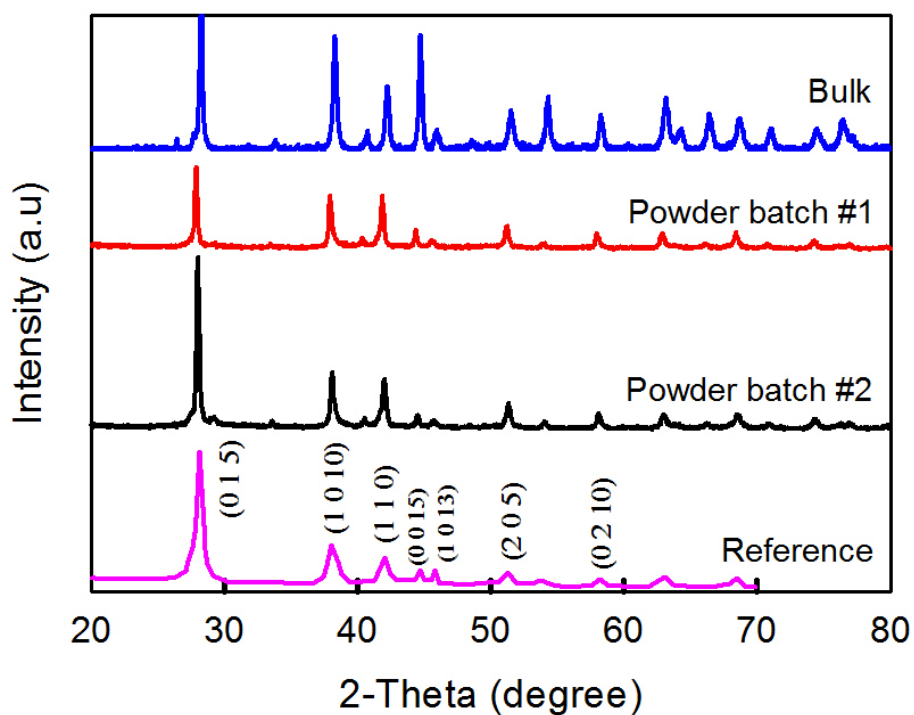
Figure 2.6　XRD patterns of the spark-eroded powder of $Bi_{0.5}Sb_{1.5}Te_3$, starting bulk ingot of $Bi_{0.5}Sb_{1.5}Te_3$, and the reference sample.

2.2.2　Seebeck Coefficient Measurement

Measurement of Seebeck coefficient (S) requires temperature and voltage measurements. For thin film samples, as in our case of the hybrid thermoelectric films, the temperature difference is measured by two thermocouples and the voltage is measured from the metal wires in the same thermocouples or from separate metal probes. While this measurement may seem very straightforward, significant error would be caused if heat transfer of the setup was not properly considered. In particular, samples having low thermal conductivity can experience significant heat leakage through the metal wires in thermocouples and/or voltage probes. Fig. 2.7 shows presentative temperature profile along the lines of two metal probes for different cases: (a) glass substrate; (b) Si wafer substrate covered with SiO_2 coating; (c) glass and Si substrates but with InGa eutectic applied at the contacts between the metal probes and the samples.　The two curves in Fig. 2.7(a) represent metal wires of two different thickness: 70 μm (corresponding to the thinnest thermocouple wires used in this study) and 300 μm. The figure shows that the heat leakage to the highly conductive metal wires could be significant with the thicker wires on a substrate with low thermal conductivity (i.e., glass). As a result, the thermocouples could disturb the local temperature profile, leading to a measured temperature difference that is lower than the actual value, and consequently an over-estimated Seebeck coefficient. It is worth noting that glass substrates have been widely used for Seebeck measurement of thermoelectric thin films, including conducting polymer films and hybrid thermoelectric films. Therefore, extreme care must be taken in order to avoid measuring over-estimated Seebeck coefficients.

After recognizing this potential source for systematic error, we devised a few strategies to reduce the heat leakage through the metal probes relative to heat conduction through the substrate. First, thinner metal and thermocouple wires would reduce the heat leakage (Fig. 2.7(a)). Also, replacing the glass with more thermally conductive substrates would essentially eliminate the error caused by the heat leakage, as show in the case of a Si wafer covered with SiO_2 (Fig. 2.7(b)). In our experiment, we adopted thermally oxidized Si wafer with 100 nm of SiO_2 on the surface and also used thin thermocouples (wire gauge is 70 μm) to suppress the relative heat leakage within the metal wires. In addition, we used the Cu wires in the T-type thermocouples to measure the voltage and avoided using additional metal probes (Fig. 2.8). The S of Cu was added subsequently to yield the S of the samples. To avoid adverse electrical contact associated with the thin wires, small amount of eutectic InGa was applied at the contacts between the wire and the samples. confirmed through the COMSOL modeling that the eutectic contacts would not affect the temperature profile, as shown in Fig. 2.7(c).
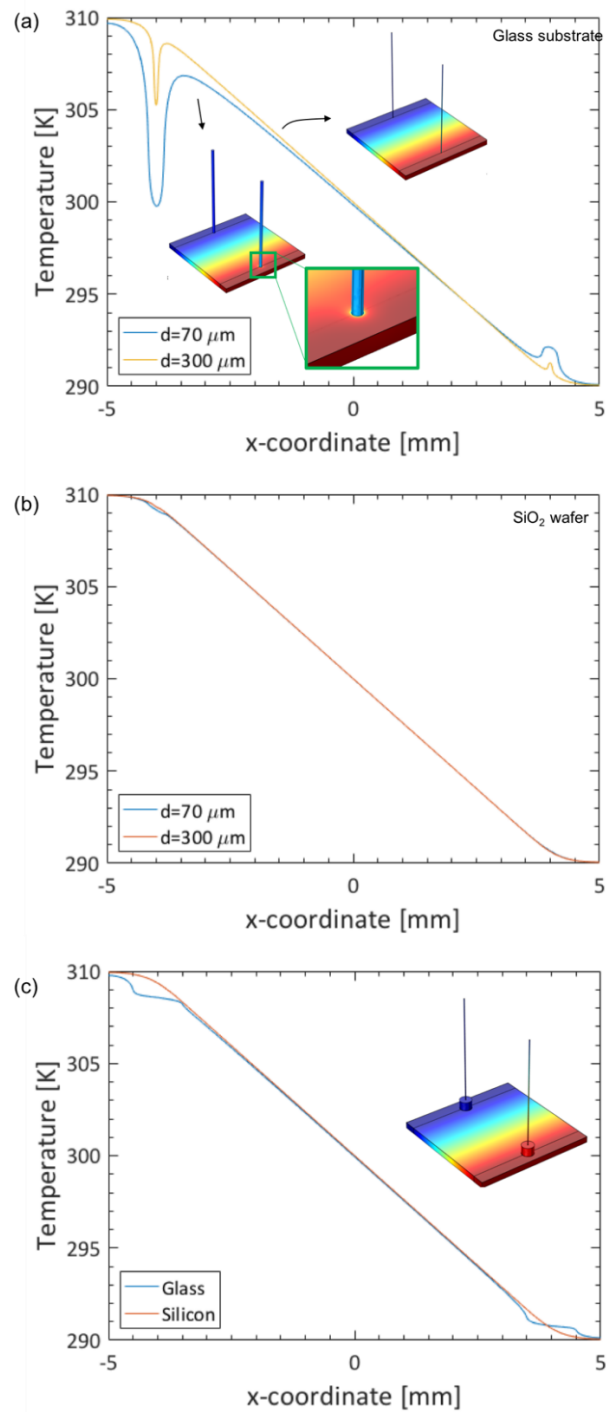
Figure 2.7   COMSOL modeling of temperature profiles when metal wires (70 µm and 300 µm in diameter) are in contact with samples: (a) glass substrate; (b) Si thermal oxide wafer; and (c) with additional contacts made of InGa eutectic alloy on both types of the substrates.
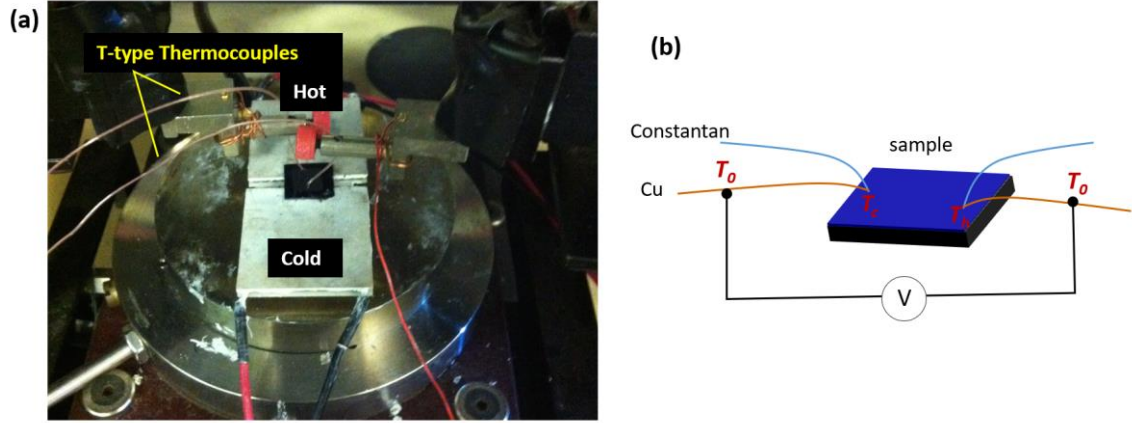
Figure 2.8   (a) Optical image and (b) Schematic of Seebeck coefficient measurement system.

To calibrate the measurement, we measured S of sole BST particles and PEDOT:PSS. Seebeck voltages (V_{TE}) were measured as a function of temperature difference (ΔT). The slope ($=dV_{TE}/dT$) represents the Seebeck coefficient (S), which are 197 µV/K and 21 µV/K for the sole BST particles and sole PEDOT:PSS, respectively, as shown in Fig. 2.9. The slope includes the contribution of the Cu wires which have S of 1.78 µV/K[44] and the S of Cu was added to determine the value of the samples (i.e., 199 µV/K and 23 µV/K for BST and PEDOT:PSS, respectively). These observed values are in close agreement with the respective bulk values (i.e., ~200 µV/K for BST particles and 20 µV/K for PEDOT:PSS)[27].

The measured apparent voltage ($V_{app} = S_{app}\Delta T$, where S_{app} is the apparent Seebeck coefficient) is determined as following equations and our measurement schematic is described in Fig. 2.8.

$$V_{app} = S_{Cu}(T_c - T_0) + S_{sample}(T_h - T_c) + S_{Cu}(T_0 - T_h) \tag{2.1}$$

$$S_{app}(T_h - T_c) = (S_{sample} - S_{Cu})(T_h - T_c) \tag{2.2}$$

$$S_{app} = S_{sample} - S_{Cu} \tag{2.3}$$

$$S_{sample} = S_{app} + S_{Cu} \tag{2.4}$$

where T_0, T_c and T_h are temperature of ambient, cold and hot sides. The measured Seebeck coefficient (S_{app}) is not the true Seebeck coefficient of the sample. Therefore, we added the Seebeck coefficient of the Cu wire (S_{Cu}) to the measured value to achieve the Seebeck coefficient of the sample (S_{sample}). In case of inorganic thermoelectric materials with much higher Seebeck coefficient (e.g. 200 uV/K for BST) than metals (e.g. 1. 78 uV/K for Cu), the error by electrodes can be negligible. However, intrinsic PEDOT:PSS has Seebeck coefficient of ~20 uV/K , so the contribution of the metals is not negligible.
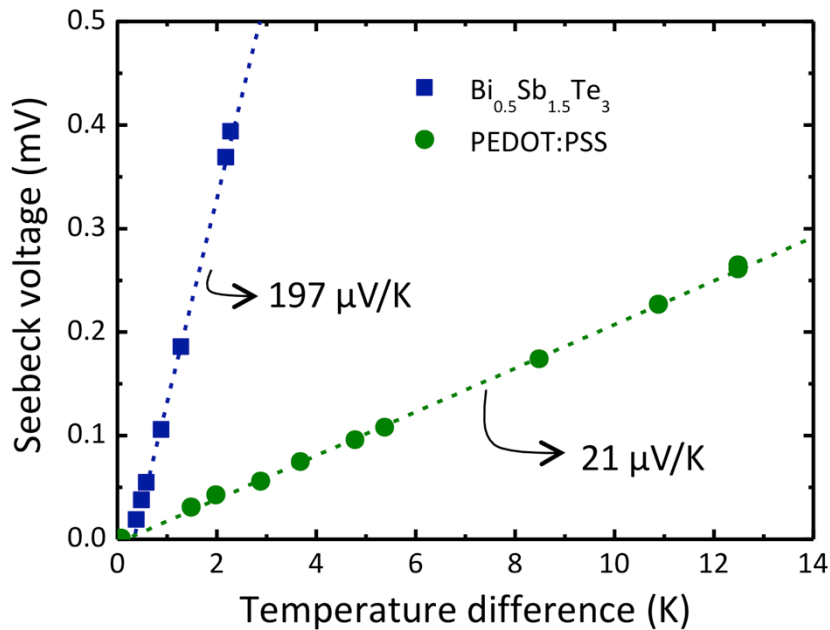
Figure 2.9   Seebeck voltage of BST (blue square) and PEDOT:PSS (green circle) as a function of temperature difference.

2.2.3 Electrical Conductivity Measurement

We measured the electrical conductivity by using the standard van der Pauw method. PEDOT:PSS without any surfactants (i.e. DMSO or TX-100) or polar solvent treatments (i.e. washing with methanol) had low conductivity, which showed a positive slope in electrical conductivity vs. temperature because of the phonon-assisted hopping mechanism.[2] On the other hand, PEDOT:PSS treated with surfactants represented nearly zero or negative slopes (see Fig. 2.10). This metallic behavior suggests that electron-phonon scattering is more dominant than phonon-assisted hopping as thermal energy increases. We attribute the absence of hopping to the removal of excess PSS after the treatments with the surfactant and/or polar solvent. PEDOT:PSS samples treated with TX-100 showed more negative slopes than those with DMSO, implying a more metallic behavior, which is consistent with the higher conductivities of the samples treated with TX-100 than those with DMSO. In addition to the higher conductivity, higher concentration of TX-100 led to an increase in the contribution of BST to thermoelectric transport, as manifested from the higher Seebeck coefficient. As a result, the slopes in TX-100 samples became more positive with a higher amount due to enhanced hopping between BST-PEDOT; while the DMSO samples showed more negative slopes with increasing amount of DMSO, indicating more dominant conduction routes through PEDOT, as the phase separation became more severe.
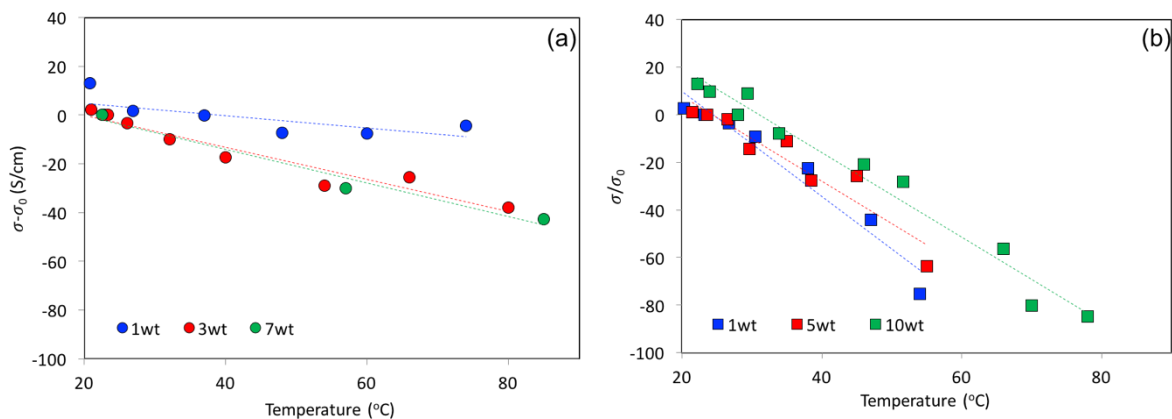
Figure 2.10   Plots of electrical conductivity as a function of temperature with (a) DMSO and (b) TX-100, where σ_0 is the electrical conductivity at room temperature.

2.2.4   Delamination Issue with DMSO

Mixed solution of BST and PEDOT:PSS was not stable while drying. PEDOT:PSS solution consists of water (~99%) and solid PEDOT:PSS (~1%); thus, the volume shrinks dramatically with the evaporation of water. In case where the weight fraction of BST was high, the mixture film was detached from glass substrate (or Si wafer with SiO_2 coating) due to the dramatic volume contraction and the opposite surface polarity between BST and PEDOT:PSS, as shown in Table S1.

After introducing TX-100 instead of DMSO, more stable layers could be formed. As displayed in Table S2, the mixed solution with 1 wt% TX-100 showed lower surface tension compared to the samples with 5 wt.% DMSO, and even after the drying process, the layers were not delaminated from substrate.

Table 2.1   Optical images of BST/PEDOTLPSS composite with 5 wt.% DMSO (non-ionic surfactant) and various amount of BST in the course of experimental process.
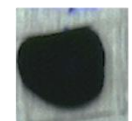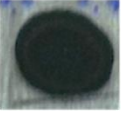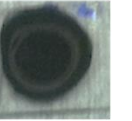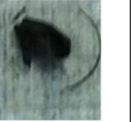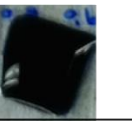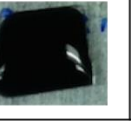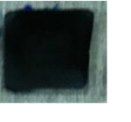
BST contents	0 wt%	2.4 wt%	6 wt%	13 wt%	29 wt%	47 wt%
PEDOT:PSS w/ DMSO	After drop-casting					
	After drying					

Table 2.2   Optical images of BST/PEDOT:PSS composite with 1 wt.% TX-100 (ionic surfactant) and various amount of BST in the course of experimental process.

BST contents	0 wt%	2.4 wt%	6 wt%	13 wt%	29 wt%	47 wt%
PEDOT:PSS w/ TX-100	After drop-casting					
	After drying					

2.2   Results and Discussion

In general, the electronic carriers in the organic-inorganic composites transport via the hopping mechanism. The different mixing behaviors of the drop-casted films between DMSO and TX-100 are shown schematically in Fig. 2.1 and in the SEM images in Fig. 2.2. As shown in Fig. 2.1(b), DMSO has short chains, C_2H_6OS, requiring a large concentration to form micelles to fully surround the surface of the solutes. The excess amount of the surfactant would increase the hopping barrier and deteriorate the mobility, which lead to degradation of the thermoelectric performance. The excess amount of the surfactant increases the hopping percolation pathways of electrons. As a result, the electron transport is expected to be less effective. In addition, both DMSO and BST have negative charges, which could lead to BST particle movements driven by columbic repulsive forces.[45,46] These factors caused the BST particle to form ring patterns on top of the liquid droplet surface, as shown schematically in Fig. 2.1(a) and in the SEM image in Fig. 2.2(a), which indicated that the particles were not effectively mixed with the polymer. More concentrated BST particles at the edge of the drop-casted film (Fig. 2.2(a)) were formed during the drying process as the outward capillary flow from the center of the droplet moved the suspended particles to the edge.[47,48] This was further evidenced from the SEM image in Fig. 2.2(e) and the energy-dispersive X-ray spectroscopy (EDX) mapping in Figs. 2.2(e) and (f), which showed that the core part is PEDOT-rich and the gray ring is BST-rich. This lack of uniformity may result in reducing the thermoelectric performance due to less amount of electronic pathways for electron hopping.

Although TX-100 also rearranges the PEDOT:PSS and forms large PEDOT domains, as in the case of DMSO, the hydrophobic tail of TX-100 leads to more randomized mixtures

with BST and PSS as well as a better adhesion on glass substrates by reducing the surface tension, whereas in the DMSO case delamination was observed after drying, as displayed in Supplementary Table S1. These distinguishable properties in TX-100 resulted in more uniform distribution of BST particles into the PEDOT matrix, as clearly shown in Fig. 2.2(c) and (d). Furthermore, the bottom-side of the hybrid films also showed different morphologies: the particles were clearly separated from the polymer matrix with DMSO while they were still embedded into the matrix with TX-100, as shown in Figs. 2.2(b) and (d), respectively.

Figure 2.11 shows the effect of surfactant concentration on CMC and conductivity. Figure 2.11(c) and (d) showed the measured contact angles as a function of the surfactant concentrations up to 10 wt.%, for DMSO and TX-100, respectively. Fig. 2.11(d) shows that TX-100 had a CMC of 0.5 - 1 wt%. However, DMSO rarely showed rapid change in the contact angle even up to 10 wt%. This implies that it is easier to form micelles with a small concentration of TX-100, which is beneficial for charge transport as a large amount of surfactant would degrade the mobility of charge carriers. Figs.2.113(e) and (f) show the measured σ as a function of the weight fraction of surfactant with DMSO and TX-100. As increasing the amount of surfactant, the σ increased because of the removal of PSS from PEDOT, as commonly observed in enhancing conductivity of PEDOT:PSS using surfactants and/or polar solvents. However, excess amount of DMSO degraded conductivity because of the reduced mobility of carriers, as shown in Fig. 2.11(e). On the other hand, samples treated with TX-100 exhibited an initial increase in σ and then reached a plateau. Interestingly, the concentration of TX-100 at which σ reached the plateau (0.5-1 wt.%) corresponds well to the CMC determined from the contact angle measurements in Fig. 2.11(d). Therefore, the

TX-100 showed a higher σ at a lower surfactant concentration, demonstrating the advantage of forming homogeneous mixture using the non-ionic surfactant.

The slopes (*dσ/dT*) of σ *vs.* temperature, as shown in Fig. 2.11(g), was used to reveal the transport mechanism: a negative slope represents a metallic behavior because σ decreases due to carrier scattering with phonons, and a positive slope implies a hopping process since it requires thermal energy to overcome the activation energy barrier. Owing to the efficient contribution of the long chain surfactant on the dispersion, the composites with TX-100 showed a more metallic behavior, or a more negative value of *dσ/dT*, as shown in Fig. 2.11(g), which is consistent with the higher σ obtained with TX-100. Interestingly, the opposite temperature dependence was observed with TX-100 in Fig. 2.11(g). To be specific, more metallic property was shown with the composites when more DSMO was added, whereas TX-100 resulted in a more hopping behavior. It indicates that the charge transport in the DMSO samples is dominated via PEDOT:PSS due to the phase separation between BST and PEDOT:PSS. On the other hand, a more uniform dispersion of BST in PEDOT:PSS assisted by the TX-100 surfactant due to inputting TX-100 indeed allowed the enhanced contributions from inorganic pillars. Consequently, we could observe less metallic but more hopping property.
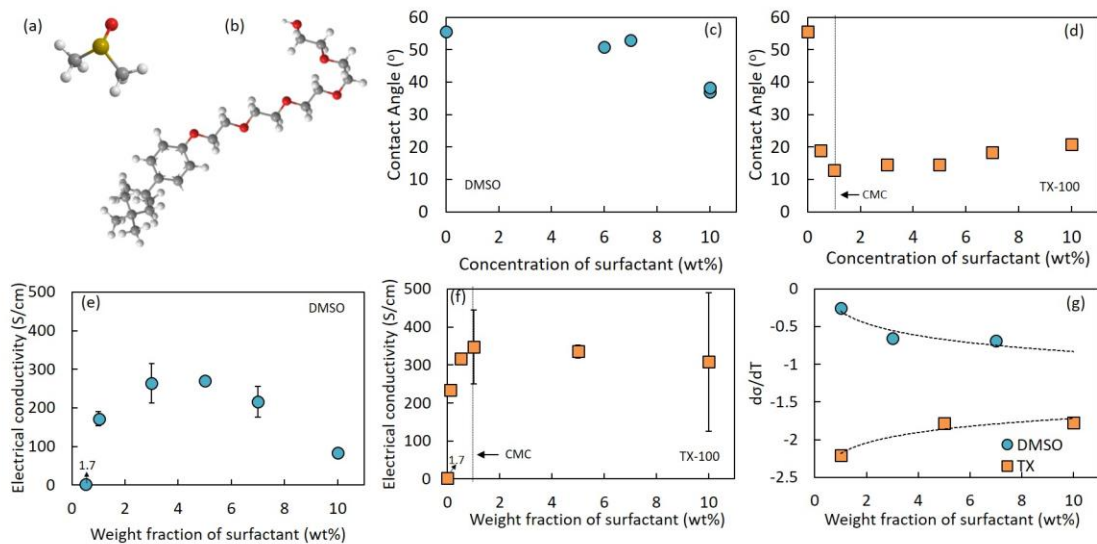
Figure 2.11 Schematics of molecular structures of (a) DMSO (C_2H_6OS) and (b) TX-100 ($C_{14}H_{22}O(C_2H_4O)_n$, where n=9 or 10), where gray, white, yellow and red spheres represent C, H, O and S, respectively. Contact angles as a function of the concentration of surfactant with (c) DMSO and (d) TX-100. The vertical line in (d) shows the CMC that leads to a sharp decrease in the contact angle. (e) and (f) plots of electrical conductivity as a function of the weight fraction of surfactant with DMSO and TX-100, respectively. (g) Plots of the derivative of electrical conductivity vs. temperature as a function of the weight fraction of surfactant.
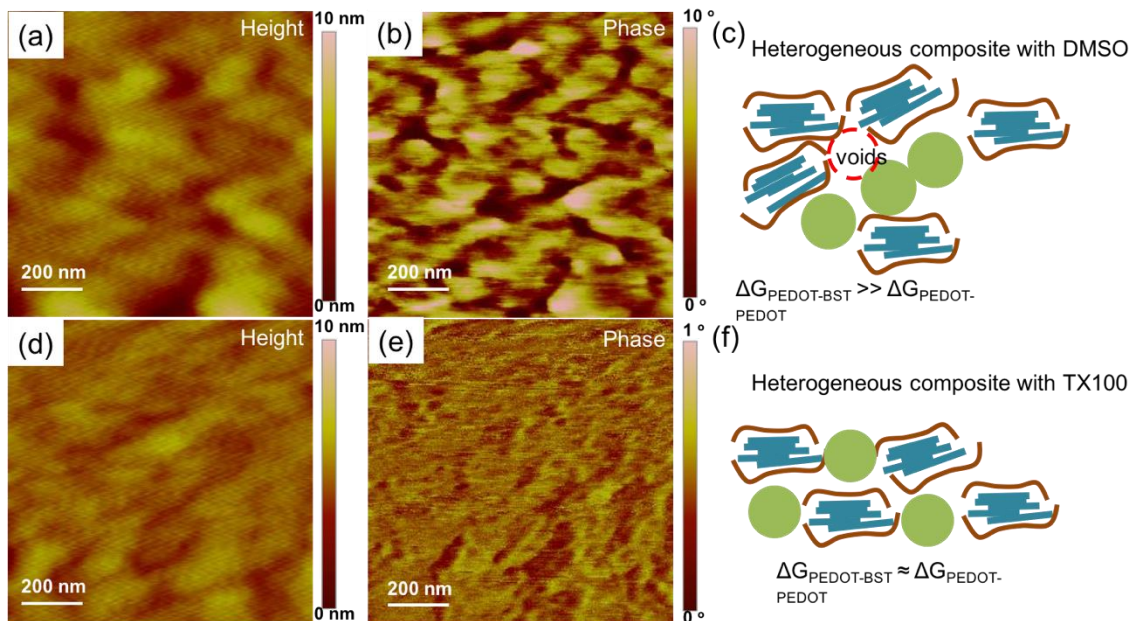
Figure 2.12 AFM images in (a) height and (b) phase and (c) a schematic of the dispersion with DMSO and (d), (e), and (f) with TX-100.

The better homogeneity in the TX-100 samples was also revealed in the AFM images shown in Fig. 2.12. The images clearly show the different dispersions between the DMSO and TX-100 surfactants: more homogeneous dispersion was observed with TX-100, which implies close displacement between PEDOT and BST, as schematically described in Figs. 2.12(c) and (f). In hopping process with localized states, when increasing the distance between the two neighbor states, the energy barrier height is exponentially increased. Therefore, carriers prefer transferring through the states which are closely located. As PEDOT:PSS has a more continuous form as a matrix, the preference transport via PEDOT:PSS caused dominant contribution in both σ and S from PEDOT:PSS, as we shall discuss later.

With the larger contribution of BST to charge transport, it is expected that S would be higher in the TX-100 case. Indeed, Fig. 2.13 shows different trends of S as a function of weight fractions of DMSO and TX-100. Optical images in the inset reveals how drastically DMSO induced the heterogeneous dispersion by expelling the BST particles from the PEDOT:PSS matrix. The particle ring (gray color) became bigger as increasing the amount of surfactant, where the amount of surfactant was insufficient to be homogeneous by forming micelle formation, as discussed earlier. The heterogeneous dispersion caused lowered S and the values were saturated at the S of pure PEDOT:PSS (~20 µV/K) (Supplementary Fig. 2.9). On the other hand, TX-100 samples showed enhanced S as increasing the amount of surfactant until the negative influence of excess surfactant outweighed the positive influence of micelles. Further, the improvement in the S will be maximized as enlarging the surface area by reducing the particle size, resulting in more contribution from the inorganic component; while we employed relatively large-sized particles by spark-erosion process to

emphasize the feasibility of easy and high-yield fabrication. As a result, as shown in Fig. 2.13, the improved S resulted in a higher peak power factor from 10 $\mu W/mK^2$ in DMSO to 40 $\mu W/mK^2$ in TX-100. We could obtain efficient interfacial charge transport by adopting a non-ionic surfactant with a long chain and controlling the micelle concentration, and observed simultaneous increase in σ and S. Therefore, the strategy developed here is promising for controlling interfacial properties of organic and inorganic hybrid TE.

The positive impact of TX-100 can be clearly seen from the increased Seebeck coefficient with the increasing concentration of TX-100, even at the expense of lower conductivity compared to pristine PEDOT:PSS. On the other hand, the DMSO samples exhibited nearly constant Seebeck coefficient and decreasing conductivity with increasing DMSO concentration. This difference between TX-100 and DMSO suggests that TX-100 does contribute to facilitate the charge transport through the inorganic coefficient to obtain a higher Seebeck coefficient, as we initially hypothesized.
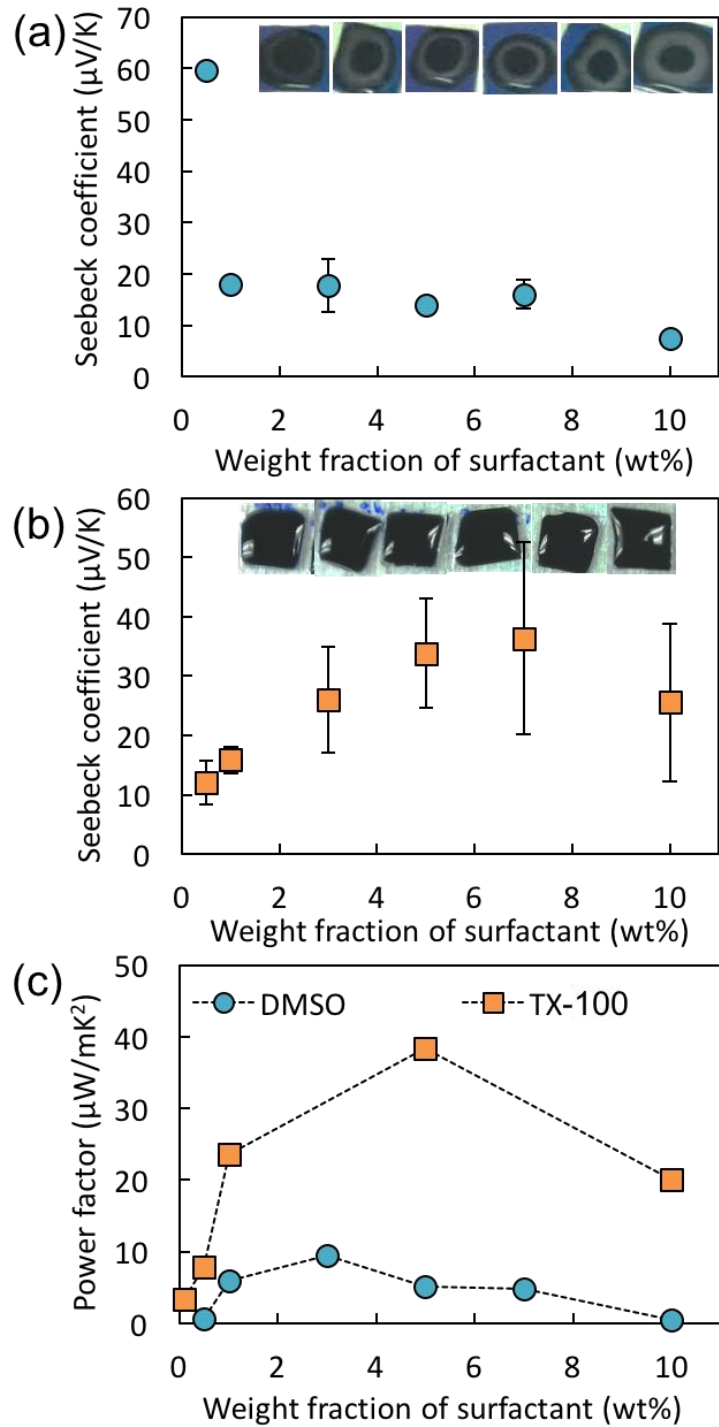
Figure 2.13　Seebeck coefficient as a function of the weight fraction of surfactant with (a) DMSO and (b) TX-100, where insets shows optical images with varying surfactant concentration and (c) power factors as a function of the weight fraction of surfactant in PEDOT:PSS(40%)/ BST (60%) with DMSO and with TX-100.

2.4 Conclusions

In summary, we have demonstrated a simple and generic physical mixing strategy to create organic-inorganic TE hybrid materials by using a novel non-ionic surfactant, TX-100, which improves the charge carrier transport from a conducting polymer (PEDOT:PSS) to BST particles through more homogeneous mixing. By using TX-100 instead of the commonly used DMSO as the surfactant and controlling the micelle concentration, we formed uniform dispersions of BST particles in the polymer matrix and observed enhanced contribution of BST to carrier transport. As a result, we achieved efficient interfacial charge transport between BSTand PEDOT and obtained simultaneous increase in σ and S. Therefore, this strategy has broad implication for interface engineering of physically mixed hybrid organic/inorganic thermoelectric materials.

Acknowledgements

Chapter 3

High-Performance Screen-Printed Thermoelectric Films on Fabrics

3.1 Introduction

Thermoelectric (TE) devices have garnered tremendous interests recently due to their promise for energy harvesting and solid-state refrigeration[49-59]. Traditional approaches to fabricate TE typically involve ingot fabrication and dicing, which could be time consuming, energy intensive, and often results in rigid devices. On the other hand, there is increasing interest to fabricate TE devices on flexible substrates and using more scalable approaches, for emerging applications such as wearable TE power generation and personalized thermo-regulation[3,13,37,60,61]. Toward this end, high-throughput and inexpensive printing has emerged as a promising fabrication route and has been widely explored in recent years[62,63]. Interesting applications have thus been demonstrated with printed TE devices, such as printed TE generators for harvesting human body thermal energy[64], energy harvesting for wireless sensor network applications[65,66], integration with energy storage devices[67], as wearable TE generator on glass fabric[7].

The bottleneck of the printed TE devices still lies in the low performance of the printed TE materials. In most processes, the TE particles were often mixed with insulating

polymeric binders to make the mixture suitable for printing. A high mass loading of the polymer binders would hinder the electrical conductivity. For instance, Madan and coworkers [65,66,68-72] developed a series of printed thermoelectric-epoxy composite films and showed TE figure of merit (ZT) up to 0.31 and 0.41 for n-type Bi_2Te_3[65,69-71] and p-type Sb_2Te_3 or $Bi_{0.5}Sb_{1.5}Te_3$ based materials[65,66,69,72], respectively. The mass loading of the polymer binders was up to ~20%. The mixtures were typically cured at 250-350 $^\circ$C to solidify the films. Lu *et al.*[73] demonstrated inkjet printing of nanoparticles to fabricate TE films which yielded maximum TE power factor of ~77 and 183 μW/m-K^2 at 75 $^\circ$C for films based on $Sb_{1.5}Bi_{0.5}Te_3$ and $Sb_{1.5}Bi_{0.5}Te_3$ nanoparticles, respectively. The relatively low power factor values were attributed to the low electrical conductivity[73]. Navone *et al.*[74,75] used screen printing and uniaxial densification at 350 $^\circ$C to fabricate TE micro-modules on polyimide substrates with p- and n-type pillars with 4 and 6 μW/m-K^2 in power factor, respectively. Recently, Varghese *et al.*[76] screen printed n-type $Bi_2Te_{2.8}Se_{0.2}$ nanoplate crystals and achieved a peak ZT of 0.43. We *et al.*[77] used screen printing to fabricate n-type Bi_2Te_3 thick films. They optimized the annealing process and achieved a high ZT of 0.61 with 500 $^\circ$C annealing for 15 mins. Similarly, Kim *et al.*[78] achieved a ZT of 0.41 in p-type Sb_2Te_3 thick film processed by screen-printing followed by thermal annealing.

Apart from electrically inactive binders, several teams have also attempted to add conductive polymers as binders into active TE materials to improve the electrical conductivity. For example, Kato *et al.*[79] prepared a mixture of $Bi_{0.4}Te_3Sb_{1.6}$ particles, conductive PEDOT:PSS and PAA (Poly (acrylic acid)), and other organic additives, and then spin-coated the mixture to yield thin films with a ZT of 0.2 at 300 K. Bae *et al.*[80] enhanced

the TE properties of PEDOT:PSS by adding Te nanorods and using chemical treatment. However, the Seebeck coefficient (S) of the printed films was usually low due to the low S of the conductivity polymers. In addition to Bi-Te based materials, other materials have also been printed. Lee *et al.*[81,82] screen-printed ZnSb films and yielded a power factor of 1.06 mW/m-K^2. They further fabricated a TE module using p-type ZnSb and n-type CoSb$_3$ films[82]. Hong *et al.*[83] used inkjet printing to fabricate TE ZnO and ZnFe$_2$O$_4$ thin films.

Despite the tremendous efforts on printed TE films, most printed devices are still limited by a relatively low ZT compared to those made from commercial bulk processes: the highest reported ZT of printed TE materials are 0.61 for n-type[77] and 0.41 for p-type[78]. As mentioned earlier, the primary reason behind the low ZT is the presence of the organic additives, such as binders, needed to make TE slurries with suitable viscosity for printing. If a large amount of these additives were used and not effectively removed, the resultant TE films would be limited by low electrical conductivity, as reported in prior work. One feasible approach to remove the organic binders is thermolysis, namely, decomposition of the organic species via burning. This process typically requires sufficient oxygen at elevated temperatures. However, exposing the TE slurries to oxygen could also oxidize the TE materials and consequently impact the TE properties. Therefore, in order to achieve a high ZT in printed TE films, it is important to: (1) use as little amount of binder as possible while maintaining the suitable viscosity for printability; (2) remove the binder as much as possible without oxidizing the TE components.

In this work, we developed a screen printing process to fabricate high-performance TE layers. We have identified a suitable binder from a class of methyl cellulose or more known for its trade name, Methocel, to make printable TE slurries with a low concentration

(0.45-0.60 wt.%), thus minimizing its detrimental effect on electrical transport. Also, it is advantageous that Methocel, which is cellulose ether, can be decomposed in an inert atmosphere, such as Ar, at a temperature that is below the typical hot pressing temperature for Bi-Te alloys (~400-450 °C)[84]. We also achieved high-quality printing of the TE layers on rough and porous fabric substrates by introducing an interface layer before printing the TE layer on the fabrics. Following printing, the binders were subsequently burnt off via sintering and hot pressing. We found reduced thermal conductivity in the n-type printed layer, which can be attributed to phonon scattering by the nanoscale defects formed after burning off the binder. With the high electrical conductivity and low thermal conductivity, the screen-printed TE layers displayed high room-temperature ZT values of 0.65 and 0.81 for p-type $Bi_{0.5}Sb_{1.5}Te_3$ and n-type $Bi_2Te_{2.7}Se_{0.3}$, respectively. These ZT values are among the highest for printed samples, and indicate considerable promise for developing wearable TE devices.
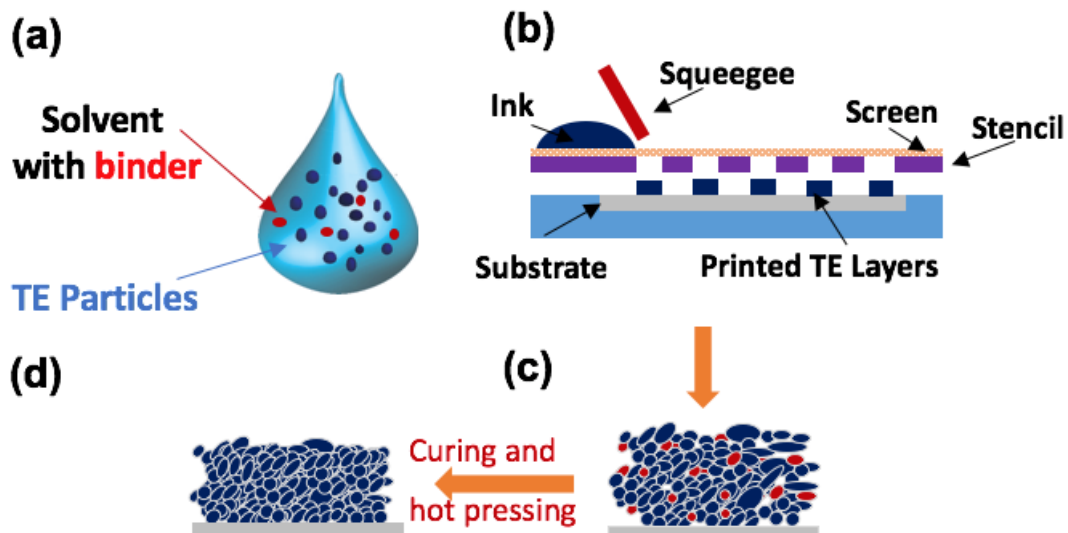
Figure 3.1 Schematic illustrations of (a) printable ink, (b) screen printing, (c) a screen-printed thermoelectric layer and (d) a hot-pressed layer after printing.

3.2   Screen Printing Process

Figure 3.1 shows the schematic of the screen printing process. We started with the fabrication of the TE particles using the spark erosion process, which can effectively break bulk TE materials into micro- and nano- particles, as reported in our prior publications [85,86]. The starting bulk TE ingots have the compositions of $Bi_{0.5}Sb_{1.5}Te_3$ for p-type (referred to as "BST" hereafter) and $Bi_2Te_{2.7}Se_{0.3}$ for n-type (referred to as "BTS" hereafter), where ZT values at room temperature are 0.77 and 0.75, respectively (see Fig. 3.15). After spark erosion, the resultant particles display a bimodal size distribution consisting of large particles with > 10 µm size and smaller particles with < 1 µm size, as shown in Fig. 3.2. The particles used for printing were sieved through 45-µm meshes by taking the consideration of particle production yield and the uniformity of the printed layers.

We then prepared the printing slurries by mixing the active TE particles, organic binders, and solvent. We selected Methocel as the binder because the cellulose ethers resulted in slurries with a viscosity of 3.3-3.5 Pa·s, which is within the optimal range to achieve uniform printing while minimizing the concentration of the binders (see Table S2 including the optical images of printed samples with various binders).[87] Also, its low decomposition temperature makes it easier to be burnt out during sintering process (see Table S1). After printing and pre-heat treatment, TE powders and the binder were left on the fabric, as shown in Fig. 3.2(c). The as-printed TE layers had poor conductivity due to the loose contacts between the TE particles. Therefore, we used uniaxial hot pressing to densify the films, which reduced the thickness of the as-printed layers by approximately three times and greatly improved the conductivity. After hot pressing the printed layer on the fabric substrate, TE

properties, including the Seebeck effect (S), electrical conductivity (σ), and thermal

conductivity (κ), were evaluated at room temperature.
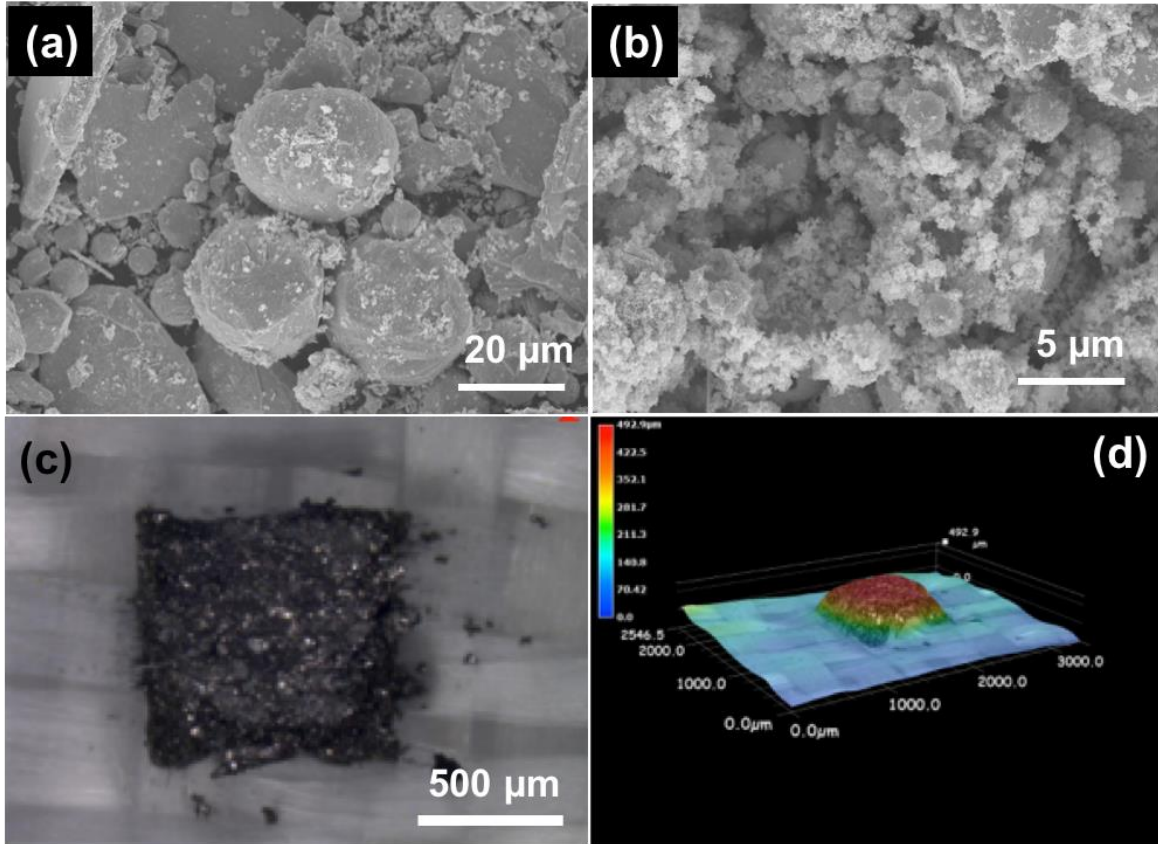
Figure 3.2   SEM images of particles with (a) large (> 20 µm) and (b) small diameter (≪ 1 µm). Optical images of (c) printed thick thermoelectric ink for high aspect ratio TE pillars before the hot-pressing process, with 1 mm^2 in area and 500 µm in thickness, on glass fiber fabric, and (d) Keyence 3D optical image of printed TE on the fabric.

3.2.1   Methods

We used the spark erosion method[85] to fabricate TE particles. P-type and n-type bulk TE ingots were purchased from Thermonamic Inc. (China) with the nominal compositions of $Bi_{0.5}Sb_{1.5}Te_3$ for p-type and $Bi_2Te_{2.7}Se_{0.3}$ for n-type. The bulk ingots were shaped into two electrodes and smaller 'charge' pieces (~2 cm in diameter) that were immersed in a spark erosion cell filled with liquid nitrogen. The electrodes were connected to a charged capacitor that discharged high pulsed current and created sparks (micro-plasmas) between two 'charge' pieces with suitable distance. Large amount of particles could be collected at the bottom of the spark erosion cell.
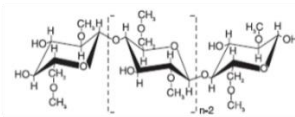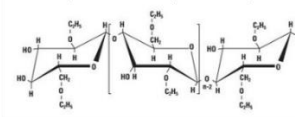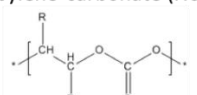
The TE particles were mixed with binder solvent which consists of methyl cellulose as the binder (METHOCEL HG 90, commercially available from DOW Wolff Cellulosics), in a mixture of ethanol 60 wt.% and water 40 wt.%. The concentration of the Methocel in the solvent was varied between 1.5 and 2.0 wt.%.   The mass ratio between the TE particles and the solvent was 7:3, so Methocel is 0.45-0.6 wt.% in the final TE inks. This mass loading of the Methocel was found to offer suitable viscosity for screen printing. The slurry was thoroughly mixed using gentle ball milling for a day. Once ink is prepared, the ink can be applied to stainless steel stencil with a pre-design pattern laser cut with holes to deposit ink onto any substrate. The stainless stencil was design through computer aid design (CAD) software (AutoCad, from Autodesk). The designed pattern in AutoCAD was defined though a laser cutting service (Metal Etch Services, San Marocs, CA). The slurry was applied to the fiberglass fabric substrate (Fiberglass #00543 from Fibre Glast Development Corporation), through a stencil using an applicator. In some experiments, a Chitosan layer was printed first

as the interface layer to smoothen the woven surface. The printed layer was cured at 250-300 ºC for 30 mins to solidify the sample and also burn off the polymeric binders. Finally, the layer was hot pressed with a uniaxial pressure of 90 MPa at 450 ºC for 5 min. The hot pressing was carried out in an Argon-filled glove box with oxygen concentration less than 80 ppm to prevent the oxidation of the TE layers.

3.2.2   Selection of Binders

We would like to choose a binder that would lead to a suitable viscosity in the resultant ink with the minimal binder concentration. In addition, a low decomposition temperature is desirable, as it would mean effective binder removal during the sintering and hot pressing processes. According to these criteria, we chose Methocel. Table. S1 shows the related properties of three binders we considered.

Table 3.1   Characteristics of potential binders for TE inks having low decomposition temperatures.

Name	Decomposition Temperature	Vehicle Composition
Methylcellulose (Methocel)	260-300 ºC	1-2% in water/ethanol
Ethylcellulose (Ethocel)	260-300 ºC	5% in α-terpineol 10% in toluene
Polypropylene carbonate (Novomer)	220 ºC	15% in dibasic ester
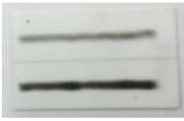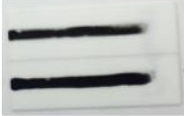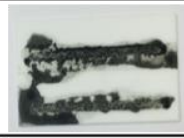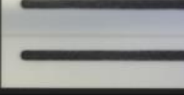
3.2.3 Optimization of Ink Composition

We optimized the ink compositions, including the types of solvents and binders as well as their concentrations, in order to achieve suitable printability, which is assessed by inspecting the uniformity and morphology of the printed layers, as shown in Table S2.

The first binder used was polyvinylidene fluoride (PVDF), which has been commonly used in printable battery applications. We initially tried to have a concentration of 70% TE particles in a polar solvent, N-methyl-2-pyrrolidone (NMP), but the ink was almost entirely solid. In order to have a screen print ink, the concentration of solvent and binder needed to increase, which diminished the concentration of the TE particles to 30% with 50% of solvent and 20% binder. Table S2 shows the printability of the inks after screen printing and curing.

We then used a cellulose ether, trademarked as Methocel from DOW Wolff Cellulosics. This binder was used because of its low decomposition temperature, and the ability to solubilize in various solvents. We tried to replace the PVDF binder with Methocel at the desired lower concentration, but it required 20% of Methocel with TE particles remained at 30% and 50% solvent (NMP) to obtain the desired viscosity. We did notice an improvement of printing as shown in Table S2.

Table 3.2   The compositions of different inks using different solvents and binders, and images of their printability.

TE	Solvent	Binder	Image
70%	30% NMP	-	
30%	50% NMP	20% PVDF	
30%	50% NMP	20% METHOCEL™ HG 90	
30%	50% NMP	20% PVDF	
30%	50% NMP	20 METHOCEL™ HG 90	
70%	25% NMP	2.5% METHOCEL™ HG 90	
70%	25% EG	2.5% METHOCEL™ HG 90	
70%	25% NMP	5% METHOCEL™ HG 90	
50%	50% (60% EtOH/40% H_2O)	2.5% METHOCEL™ HG 90	
70%	30% (60% EtOH/40% H_2O)	2.5% METHOCEL™ HG 90	
50%	50% (60% EtOH/40% H_2O)	1.5% METHOCEL™ HG 90	

3.3 Measurement Setup

3.3.1 Electrical Conductivity and Seebeck Coefficient Measurement

The TE layers after screen printing and hot pressing were approximately 1 cm^2 and with thickness ranging from 10-700 μm. We used the van der Pauw method [88,89] to measure the in-plane electrical conductivity and a custom-made setup to measure the in-plane Seebeck coefficient. For the Seebeck measurement, the sample was placed across two thermoelectric blocks maintained at two different temperatures. Two T-type thermocouples were located near the two ends of the samples to measure the temperature. The temperature difference between the thermocouples was varied from 0 to 5 K, and the resultant Seebeck voltage was recorded with the two Cu probes in the thermocouples (Fig. 3.3). The Seebeck coefficient of the TE layers was corrected with the S of Cu (1.8 μV/K) [44]. This method was calibrated with bulk BST and BTS samples (Fig. 3.15) as well as a Ni foil sample (Fig. 3.4).

We calibrated the Seebeck measurement by measuring the S of a 0.5 mm thick Ni foil. The Ni foil with 99.994% purity was purchased from Alfa Alsea. As shown in Fig. 3.4, the slope of the ΔV vs ΔT data is -20.6 μV/K. After subtracting the contribution of the Cu wires, the S of Ni is determined to be -18.8 μV/K, in excellent agreement with the literature value of -19 μV/K for Ni [44].
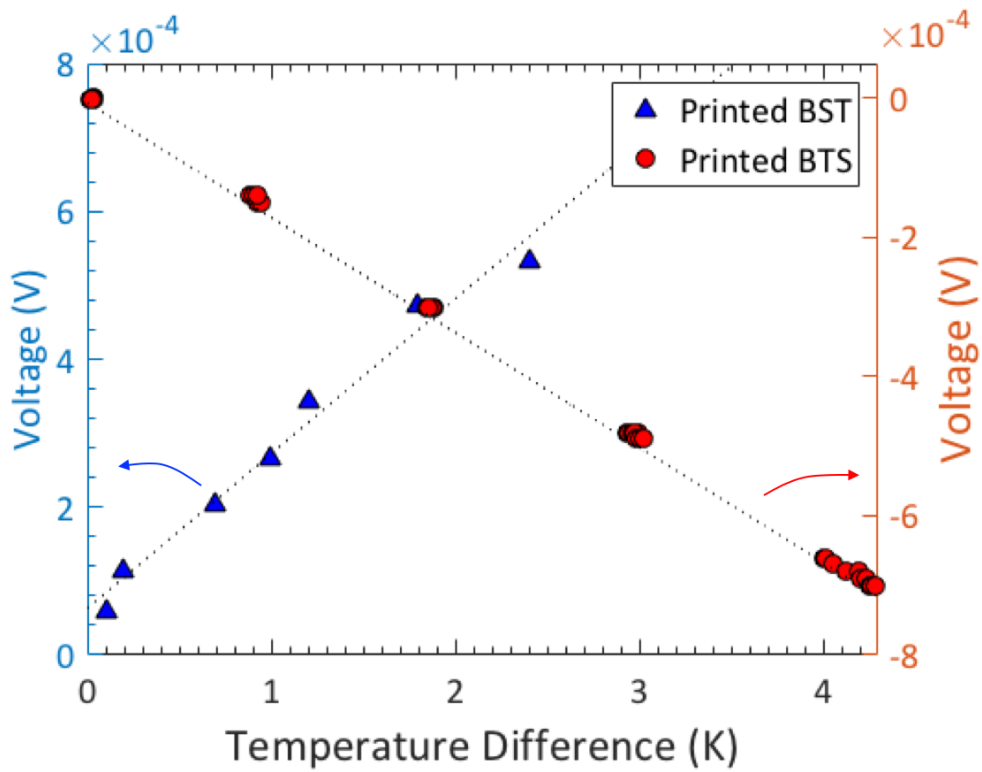
Figure 3.3 Plots of voltages as a function of temperature difference to obtain the Seebeck coefficient from the slops with p-type BST and n-type BTS.
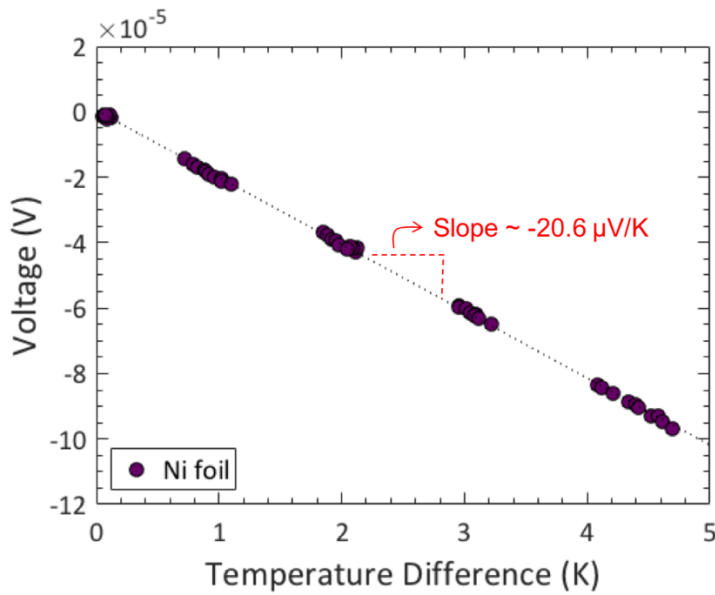
Figure 3.4 Open-circuit voltage as a function temperature difference for a Ni foil.

3.3.2   In-Plane Thermal Conductivity: Angstrom Method

The Angstrom method [90] involves the periodic heating at one end of the sample and the detection of the amplitude and phase of the resultant temperature wave at two different locations along the sample. In our setup, one end of the printed layer (approximately 1 cm long) was anchored to a Cu block, which was periodically heated using a thermoelectric module powered by a sinusoidal current. Two small thermocouples, one located near the heat source (near-side) and the other located further away (far side), were used two detect the temperature wave. The frequency range of the AC current was chosen such that the thermal penetration depth is as large as possible (to ensure a large and detectable temperature oscillation on the far end of the sample) but shorter than the distance between the two thermocouples. Under this condition, the thermal conductivity (κ) can be obtained as [90]:

$$\kappa = \frac{L^2}{2 \cdot dt \cdot \ln\left(\frac{M}{N}\right)} \rho C_P \tag{3.1}$$

where $L = x_2 - x_1$, M and N are the amplitudes of the temperature wave at x_1 and x_2, dt is the phase difference (in seconds) between x_1 (near-side) and x_2 (far-side). The measured thermal diffusivity was then converted to in-plane thermal conductivity ($\kappa_\parallel = \alpha\rho C_p$) using the bulk specific heat values ($\rho C_p = 1.26 \times 10^6$ and 1.22×10^6 J/m^3.K for Bi$_{0.5}$Sb$_{1.5}$Te$_3$ and Bi$_2$Te$_{2.7}$Se$_{0.3}$, respectively, based on data of Bi$_2$Te$_3$ and Sb$_2$Te$_3$ reported in Ref. [91]), where the contribution of the remained binders could be negligible owing to their little amount. Since the substrates are porous fiber glass having low thermal conductivity, we can assume that the measured sample κ is equal to that of the TE layers.

We calibrated the Angstrom method using borosilicate and polyethylene samples, as shown in Table S3 and S4, respectively. To yield accurate measurement results, it is important

to ensure a short thermal penetration depth (high heating frequency) as well as a short distance between the two thermocouples, compared to the length of the sample.
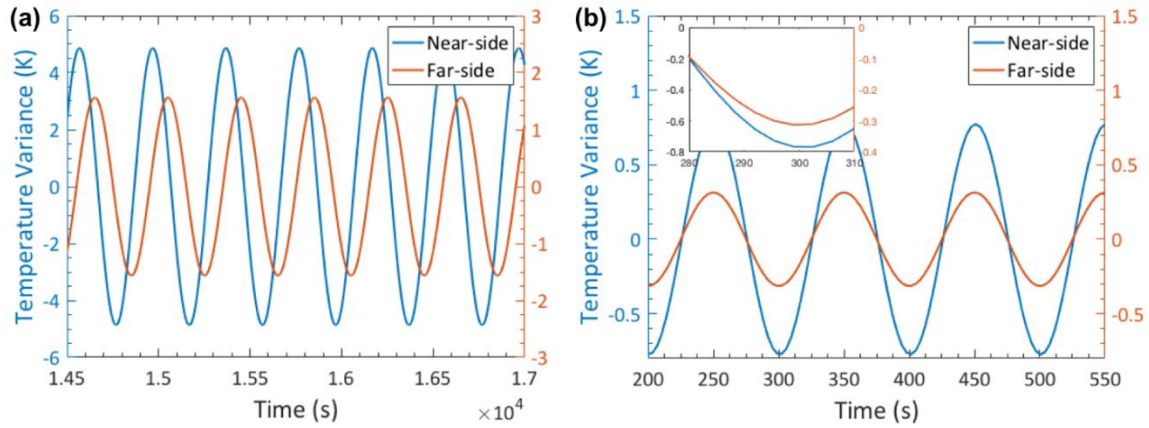
Figure 3.5   Temperature wave of borosilicate (a) and polyethylene (b).

Table 3.3   Summary of fitted values from Angstrom measurement on *borosilicate*

	@T$_H$	@T$_C$
Amplitude (K)	4.866	1.564
Ratio of Amplitude	3.111	
Frequency (Hz)	0.0025	0.0025
Phase (s)	68.067	151.700
Phase delay (s)	83.633	
Distance btw two thermocouples (m)	0.012	
Diffusivity (W/Jm^2)	7.586x10^{-7}	
Thermal conductivity (W/mK)	1.35	

Table 3.4   Summary of fitted values from Angstrom measurement on *polyethylene*

	@T_H	@T_C
Amplitude (K)	0.773	0.314
Ratio of Amplitude	2.461	
Frequency (Hz)	0.01	0.01
Phase (s)	25.840	125.111
Phase delay (s)	99.271	
Distance btw two thermocouples (m)	0.006	
Diffusivity (W/Jm^2)	2.01x10^{-6}	
Thermal conductivity (W/mK)	0.354	

Table 3.5   Summary of fitted values from Angstrom measurement on *p-type BST*.

	@T_H	@T_C
Amplitude (K)	5.485	2.504
Ratio of Amplitude	2.191	
Frequency (Hz)	0.005	0.005
Phase (s)	5.408	19.891
Phase delay (s)	14.483	
Distance btw two thermocouples (m)	0.005	
Diffusivity (W/Jm^2)	1.101x10^{-6}	
Thermal conductivity (W/mK)	1.29	

Table 3.6   Summary of fitted values from Angstrom measurement on *n-type BTS*.

	@T_H	@T_C
Amplitude (K)	9.696	7.614
Ratio of Amplitude	1.273	
Frequency (Hz)	0.001	0.001
Phase (s)	14.388	23.141
Phase delay (s)	8.754	
Distance btw two thermocouples (m)	0.00167	
Diffusivity (W/Jm^2)	6.59x10^{-7}	
Thermal conductivity (W/mK)	0.77	

3.3.3 Cross-Plane Thermal Conductivity: 3ω Method

We used the standard 3ω method to measure cross-plane thermal conductivity [92] (see Fig. 3.6(a)). The printed layers were first polished to a smooth finish as in Fig. 3.6(b) and then a thin (600 nm thick) parylene dielectric layer was deposited using the atomic layer deposition. Cr/Au 3ω heaters of 5 μm wide and 1mm long were fabricated through photolithography, sputter deposition, and liftoff (Figs. 3.7(c,d)). During the measurement, an AC current, $I(\omega)$, was applied onto the 3ω heater line which resulted in heat flux with a frequency of 2ω, accompanying with the generated thermal wave diffusing into the specimen. The penetration depth is determined by the thermal diffusivity of the specimen and the frequency of the AC current. Because the resistance of the heater depends almost linearly on the temperature, the resistance is also modulated at a frequency of 2ω. The voltage drop across the heater thus contains a third harmonic ($V_{3\omega}$) that depends on the AC temperature rise (T_2) of the heater, expressed as,

$$V_{3\omega} = \frac{I_0}{2}\frac{dR}{dT}T_{2\omega}\sin(3\omega t + \phi)$$

(3.2)

By extracting $T_{2\omega}$ from the measured $V_{3\omega}$ signal, we can obtain the thermal conductivity of the TE layers by the slope method [92],

$$k_s = -\frac{P}{2\pi L}\left(\frac{d(\Delta T)}{d(\ln(2\omega))}\right)^{-1}$$

(3.3)

where P is the heating power, L is the heater length, ΔT is the temperature rise. A length scale known as the thermal penetration depth can be defined from dimensional considerations,

$$L_P \equiv \left(\frac{\alpha}{2\omega} \right)^{1/2} \tag{3.4}$$

which physically represents the distance the thermal wave travels over the period of the heat oscillation. In order to satisfy the approximations made in the slope method, the fitting must be applied within a somewhat restricted frequency regime. To approximate an infinitely small line source experimentally, the penetration depth should be larger than the line width (which is finite in reality), and in order to justify the semi-infinite substrate approximation, the penetration depth should be shorter than the thickness of the substrate (which is finite in reality). The frequency range chosen for thermal conductivity analysis is from 1000 to 8000 Hz, which corresponds to the thermal penetration depth of 10 μm - 40 μm, smaller than the 3ω heater strip width (~5μm) used here.

Figures 3.7(e) and (f) show the measured 3ω voltage and the inferred temperature rise of the 3ω heaters on the p- and n- type samples, respectively. The responses at lower and higher frequency were related to thermal conductivity of the epoxy substrate and the TE samples, respectively. Based on the slope of the temperature rise in the higher frequency range, thermal conductivity of BST and BTS is 1.06 W/mK for p-type and 0.83 W/mK for n-type, respectively.
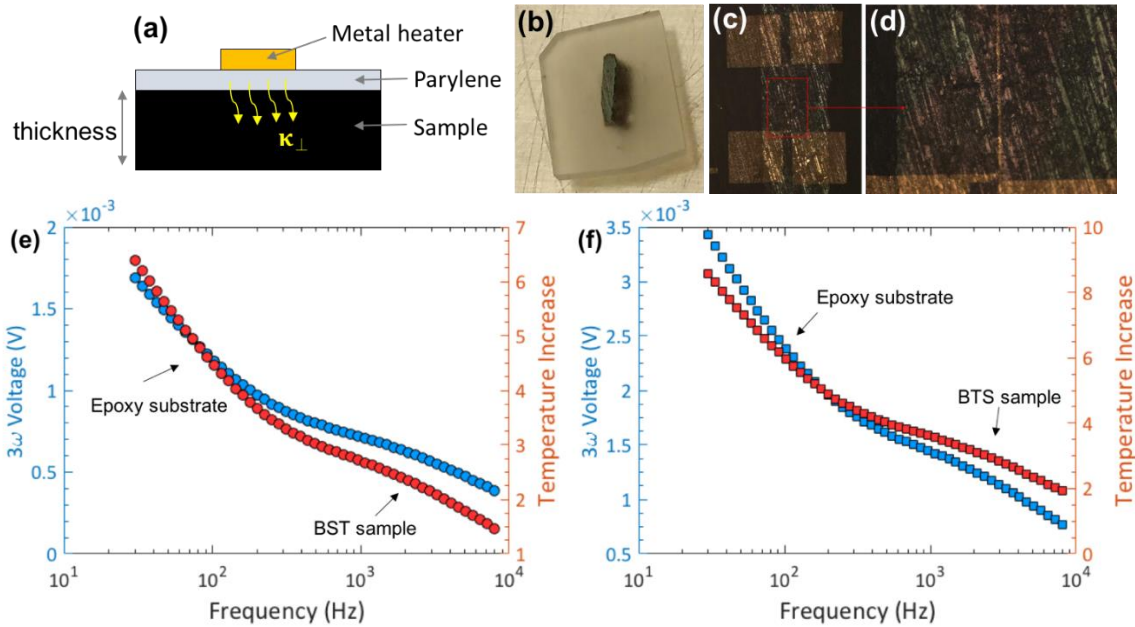
Figure 3.6 (a) Schematic of 3ω method for cross-plane thermal conductivity measurement. (b) Optical images of BST embedded in epoxy. (c,d) Optical images of the metal electrodes. Plots of measured voltages and temperatures of (e) p-type BST and (f) n-type BTS as a function of heating frequency using 3ω method.

3.4 Thermoelectric Property

3.4.1 Seebeck Coefficient

Figure 3.3 shows the in-plane S coefficient measurement results, where the S is determined by the linear slope in the plot of thermovoltage as a function of temperature difference (e.g., $S=-dV/dT$). Our optimized slurries showed S of 209 µV/K and -165 µV/K in p-type and n-type materials, respectively after printing and pre-heating to remove solvents. The S value for the p-type printed BST is close to that of bulk BST (220 µV/K), whereas the value for the n-type printed BTS is considerably lower than the bulk value (-208 µV/K), presumably due to the composition change during the ink formulation or hot pressing process,

as evidenced from the EDS analysis (see Figs. 3.13 and 3.14). We also observed that the printed TE layers have similar S compared to that of TE powders, which were prepared by drop-casting the TE powders dispersed in organic solvents on a glass substrate followed by drying. This shows that the addition of the Methocel binder has minimal influence on S. This is because the Methocel is insulating and its amount is small (up to 0.6 wt.% of the inks), and S of the TE/Methocel mixture is dominantly determined by that of the TE materials.

3.4.2 Electrical Conductivity

Due to the minimal influence of the binder on S, the main hurdle to achieve a high ZT in the printed films is the electrical conductivity σ and thermal conductivity κ. One of the challenges associated with the printing on fabric is the roughness and porosity of the substrate that lead to non-uniform printed layers, which would limit the electrical conductivity.   Depending on the design of the weave and the material, fabrics have a certain degree of porosity and a large roughness over 100 μm (Figs. 3.8(a) and (c)), as determined using a Keyence optical surface profiler. This leads to the non-uniformity on the printed layers as some loose fibers can be embedded inside the printed layer as it cures. The infiltration of the TE material into the porous fabric also caused a large error in the determination of the layer thickness and consequently σ, especially for small layer thickness. As shown in Fig. 3.7(h), the σ of the printed BST layers on bare fabric was less than 200 S/cm, substantially lower than the bulk BST ($\sigma \sim 1000$ S/cm). Also, the σ increases with the thickness of the printed and hot-pressed TE layers: σ was improved from 8.5 to 190 S/cm

by increasing the thickness from 9 to 111 μm (Figs. 3.8(e) and (f)), suggesting the detrimental effect of the substrate.
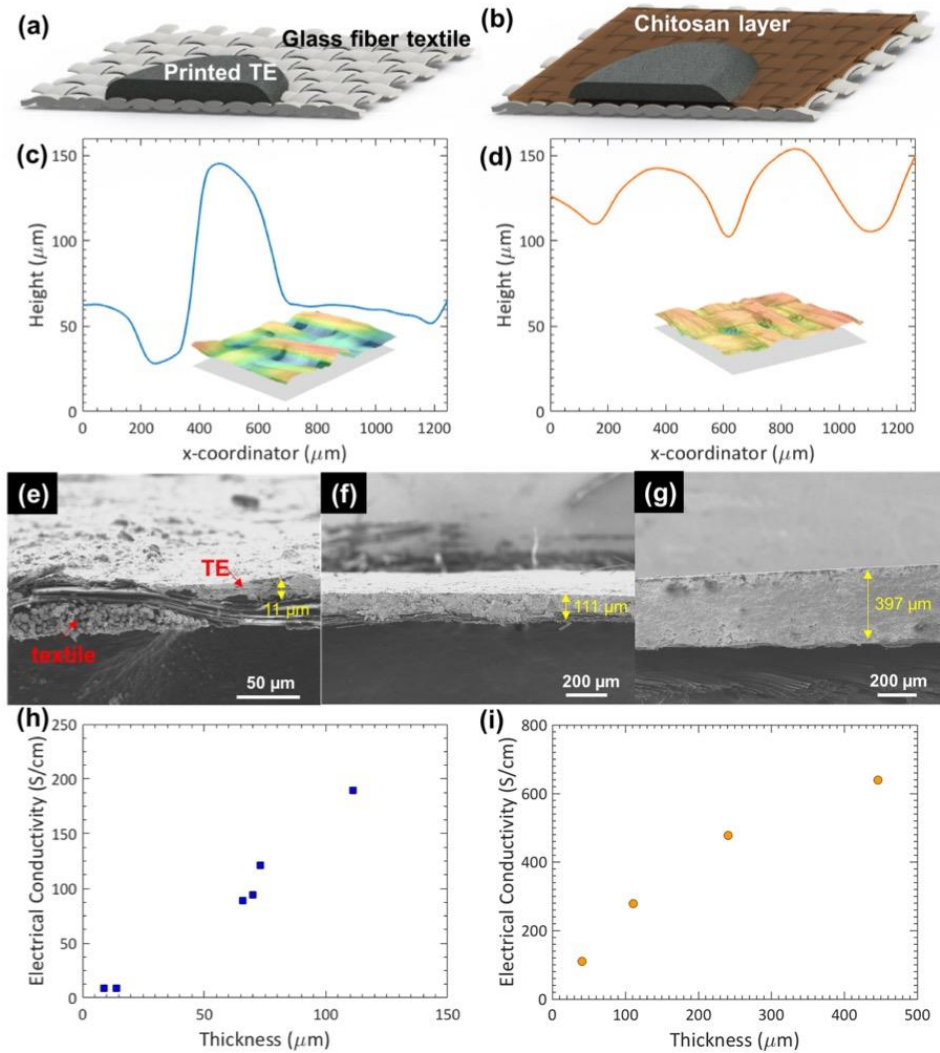
Figure 3.7   Schematics of printed thermoelectric layer on top of bare glass fiber fabric (a) and on Chitosan layer (b) used as a preliminary layer to smoothen the rough bare fabric. Optical surface profiles of bare glass fiber fabric (c) and printed Chitosan layer on top of glass fiber fabric (d) with their measured 3-dimensional surface images using a Keyence optical microscope (insets). SEM cross-sectional images of printed and hot-pressed samples on fabrics with thickness of 11 μm (e), 111 μm (f) and 395 μm (g). Plots of electrical conductivity as a function of thickness of the printed BST layers without (h) and with chitosan (i).

Our approach to mitigate the effect of the roughness and porosity of the fabric substrate is to print a non-conductive layer, referred to as the interface layer, to level the surface and block the pores in the substrate. We also increased the thickness of the TE layer to reduce the thickness ratio between the fabric and the TE layer and to minimize the adverse contribution of the fabrics. We adopted Chitosan as the interface layer, as schematically shown in Fig. 3.7(b). Chitosan is a well-known binder used in printing, e.g., for controlling the viscosity [93,94] and for treatment of fabric. [95-97] The presence of the Chitosan interface layer greatly reduced the surface roughness of the fabric, to within 50 μm, as shown in Fig. 3.7(d). Consequently, the electrical conductivity was largely improved: at the same thickness of ~110 μm, employing the Chitosan layer increased the conductivity from 190 S/cm (Fig. 3.7(h)) to 278 S/cm (Fig. 3.7(i)). Thicker films printed on the Chitosan layers showed higher σ. We also carried out a similar study on n-type BTS by introducing the Chitosan layer and varying the printed TE layer thickness. As a result, the σ was improved up to 639 S/cm and 763 S/cm for p-type BST and n-type BTS on samples with Chitosan and thicker TE layers. Although the large thickness could sacrifice the flexibility of the TE layer itself, a device made of small printed TE pillars on the flexible fabric would still remain flexible.

3.4.3   Thermal Conductivity

Since S and σ were measured along the in-plane direction of the printed layers, it is imperative to also measure the thermal conductivity σ along the same orientation, which is often challenging. Here we employed the Angstrom method [90] to measure the in-plane thermal conductivity ($\kappa_{\parallel}$) of the printed TE layers. In this method, one end of the

sample was heated using a sinusoidal heat source, and the temperature waves were measured at two different locations of the sample, as shown in Fig. 3.8(a). We calibrated our setup with measurements on borosilicate and polyethylene (see Fig. 3.5 and Tables 3.4 & 3.5), which have well-known thermal conductivity values. The measured $\kappa_\parallel$ was found to be 1.29 and 0.77 W/m-K for the thickest (600-800 μm) p-type BST and n-type BTS layers (Table 3.6 and 3.7).
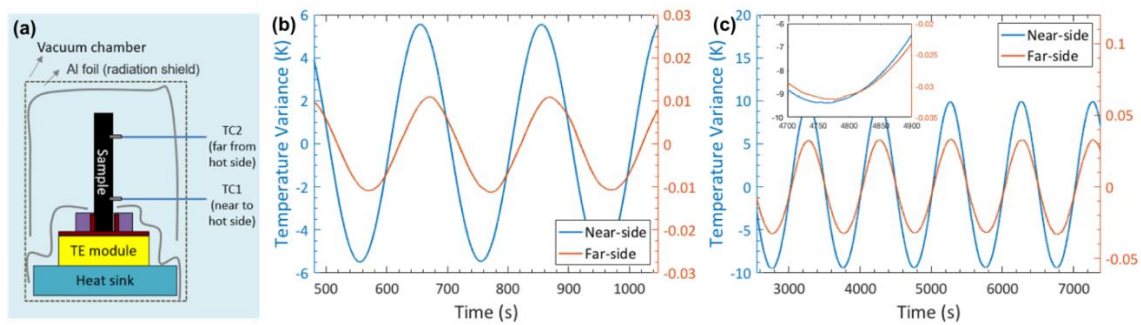
Figure 3.8   Angstrom method: (a) Schematic of the setup. Measured temperature wave of (b) p-type BST and (c) n-type BTS in the Angstrom setup.

To assess the anisotropy of the thermal conductivity, we also measured the cross-plane thermal conductivity ($\kappa_\perp$) using the 3ω technique [98,99]. By using the slope method (see details in the Supplementary Information), we determined the $\kappa_\perp$ to be 1.06 and 0.83 W/m-K at 300 K, for p- and n-type TE layers, respectively. The in-plane and cross-plane thermal conductivity results suggest that the printed TE films were essentially isotropic after the uniaxial hot pressing process.

With the measured in-plane electrical conductivity and thermal conductivity, we can estimate the lattice thermal conductivity: $\kappa_L = \kappa - L\sigma T$, where L is the Lorenz number, and is taken to be $1.67 \times 10^{-8}\ W\Omega K^{-2}$ and $1.74 \times 10^{-8}\ W\Omega K^{-2}$ for p-type BST and n-type BTS, respectively, where the L was corrected with S [100]. The calculated κ_L is 0.97 and 0.37 W/m-K for the p-type and n-type layers, respectively. The κ_L for p-type BST is almost identical to that of the starting bulk material value (calculated to be 1.04 W/m-K by using the same L and the data shown in Fig. 3.15). However, the κ_L for n-type BST is significantly lower than the starting bulk value (1.23 W/m-K, see Fig. 3.15). This difference in κ_L in the p- and n-type printed layers is likely originated from the microstructures, as we shall discuss next.

3.5   Investigation of Microstructure

In order to investigate the relations between the measured thermoelectric properties and microstructures, high resolution-transmission electron microscopy (HR-TEM) was employed. The cross-sectional HR-TEM Energy-dispersive X-ray spectroscopy (EDS) element mapping images show the carbon element distributed in the p- and n-type TE layers in Fig. 3.9. In order to compare the amounts of carbon in the sintered samples, EDS quantifications were carried out. As shown in Table 3.8, the atomic percent of carbon in the samples with Methocel is similar to that in the samples without Methocel, revealing that the binders in the p-type and n-type were effectively removed without oxidizing the TE components and degrading the electrical conductivity. Therefore, the carbon elements

observed with the binder in Fig. 3.9 were attributed to the hydrocarbon contamination in the surface of samples.
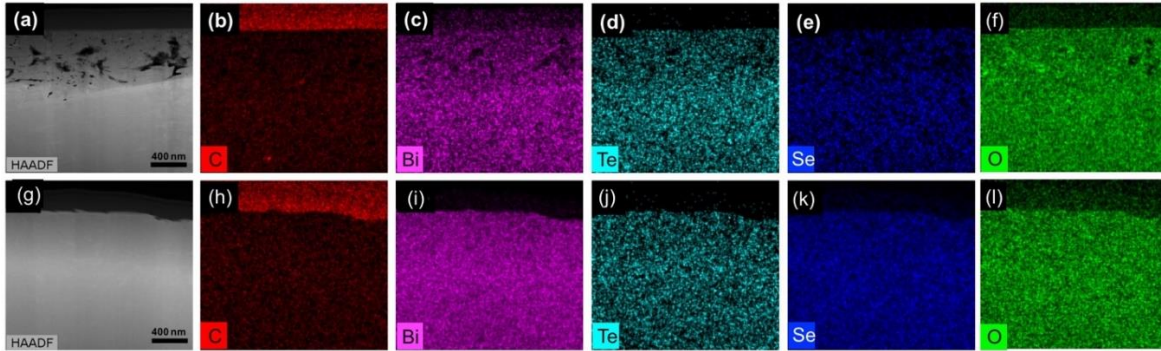
Figure 3.9   TEM EDS mapping images of hot pressed p-type (a-f) and n-type (g-l) with Methocel.

For the p-type printed sample, there is no clear nanoscale feature in the high angle annular dark field (HADDF) image in Fig. 3.10(a), similar to the case of hot-pressed p-type BST without Methocel. This may explain the similar κ_L between the p-type printed layers and bulk samples. However, for the n-type sample, the defects with the length scale of a few hundred nanometers were clearly observed in the printed sample with Methocel after hot pressing as shown in the HADDF image in Fig. 3.10(b). Considering that these defects were not found in the samples without Methocel (Fig. 3.11(b)), it seems that these thin and long defects were generated by the rearrangement of n-type TE particles while the binders were burning out in the sintering process, which could have facilitated the formation of the embedded defects. The nanoscale defects can effectively scatter the phonons in addition to the boundary scattering [101,102] due to the formation of spark-eroded particles, leading to lower

lattice thermal conductivity in the printed n-type layers without significantly affecting charge transport. Thus, the thermal conductivity of the printed n-type samples is lowered compared to that of the bulk.
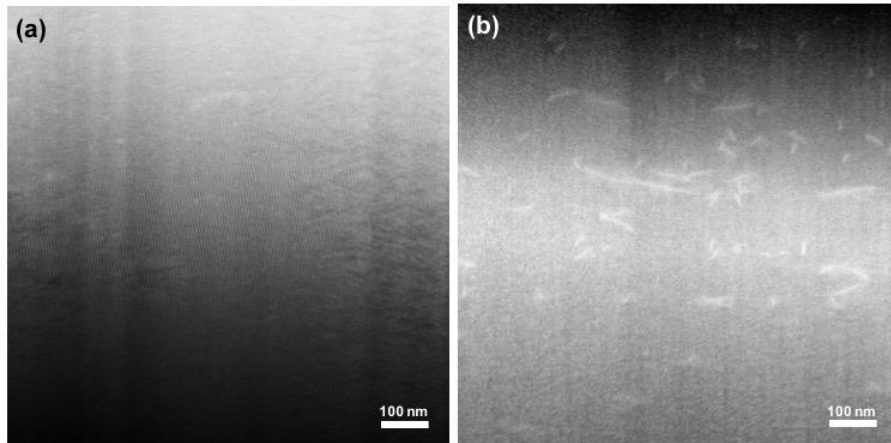
Figure 3.10   TEM HADDF images of hot pressed p-type (a) and n-type (b) with Methocel.

3.5.1   Additional Microstructural Information
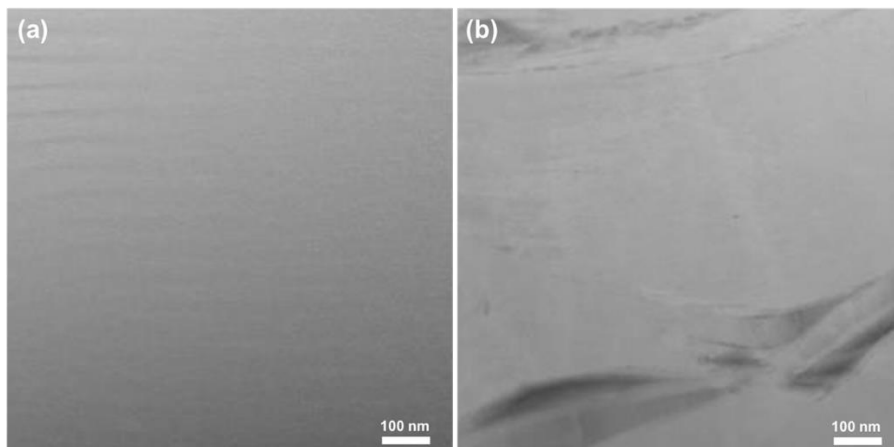
Figure 3.11   HAADF images of hot pressed p-type (a) and n-type (b) without Methocel.

Table 3.7   TEM EDS quantification of hot pressed samples*

EDS quantification (atomic %)		Bi	Sb	Se	Te	C	O
p-type BST	without Methocel	14.44	28.57	-	51.43	2.11	3.48
	with Methocel	13.06	29.94	-	52.14	1.98	2.97
n-type BTS	without Methocel	43.56	-	3.85	46.50	3.73	1.29
	with Methocel	46.64	-	2.58	47.21	2.54	1.05

*Note: The TEM EDS was primarily used to compare the concentrations of C and O in samples with and without the Methocel binders. Since the TEM EDS analysis was only focused on very tiny localized areas and the samples may have non-uniform compositions, the compositions of Bi-Sb-Te in p-type and Bi-Te-Se in n-type from the TEM EDS analysis are different from those in the SEM analysis.

3.5.2   Energy Dispersive X-ray Spectroscopy Analysis

Fig. 3.13 shows the compositions of the starting bulk p- type $Bi_{0.5}Sb_{1.5}Te_3$ and n-type $Bi_2Te_{2.7}Se_{0.3}$. To evaluate the composition variation, we carried out the EDS analysis on printed and hot-pressed samples, as shown in Fig. 3.14. We found that the concentration of Se was changed to $Bi_2Te_{2.85}Se_{0.15}$ in the n-type TE, while the composition remained the same for the p-type TE. Although the observed Se concentration change in the n-type sample is small, it cannot be negligible due to the fact that the optimized n-type solid solution ($Bi_2Te_{2.7}Se_{0.3}$) requires the low concentration of Se. It is known that the lower fraction of Bi_2Se_3 can reduce the energy gap, leading to a lower Seebeck coefficient.[3] Indeed, in our

experiments, the change in the Se concentration led to the degraded Seebeck coefficient in

n-type sample, from the bulk value of -208 µV/K to -165 µV/K in the hot-pressed sample.

(a) P-type: $Bi_{0.5}Sb_{1.5}Te_3$

Element	Weight%	Atomic%
Bi	14.78	8.91
Sb	25.62	26.51
Te	58.76	58.00
O	0.84	6.58
Totals	100.00	

(b) N-type: $Bi_2Te_{2.7}Se_{0.3}$

Element	Weight%	Atomic%
Bi	53.26	38.98
Te	44.44	53.26
Se	1.87	3.61
O	0.43	4.15
Totals	100.00	
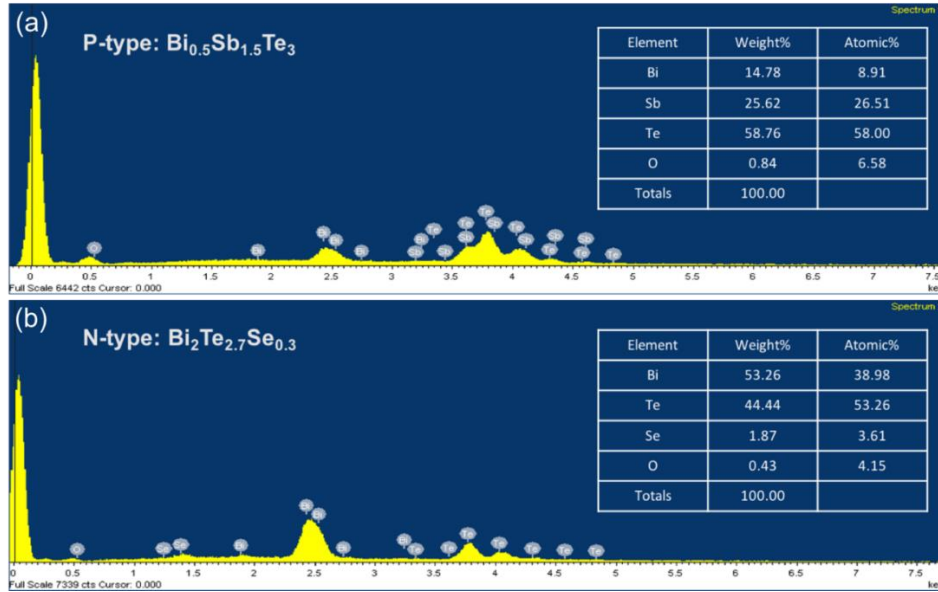
Figure 3.12   Energy Dispersive X-ray Spectrum (EDS) of bulk p- (a) and n-type (b) samples.

(a)

Element	Weight%	Atomic%
Bi	15.61	8.90
Sb	25.10	24.57
Te	57.36	53.58
Si	0.47	2.01
O	1.47	10.94
Totals	100.00	

(b)

Element	Weight%	Atomic%
Bi	51.25	32.01
Te	44.68	45.72
Se	1.58	2.60
Si	0.20	0.92
O	2.30	18.74
Totals	100.00	
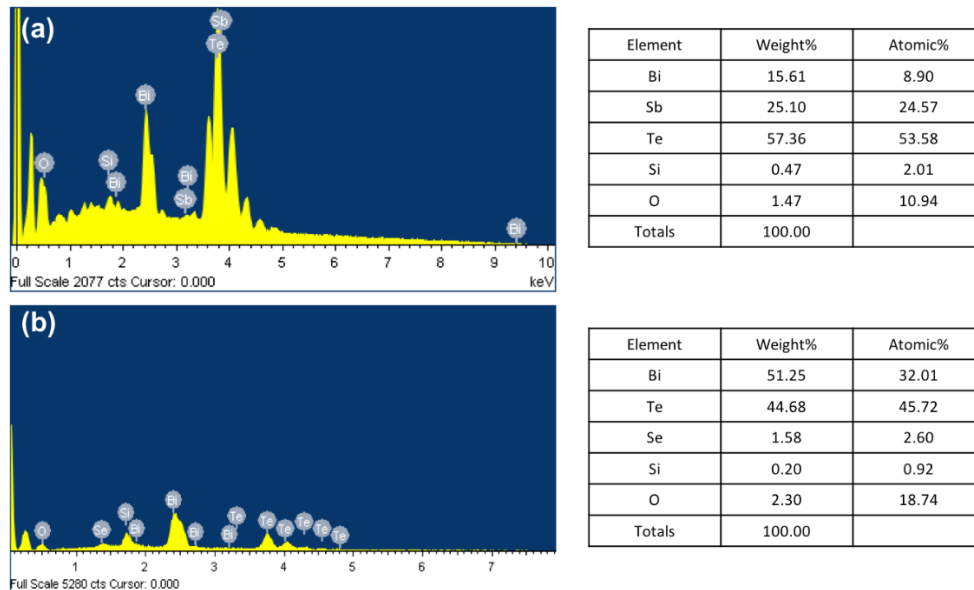
Figure 3.13   EDS of hot-pressed p- (a) and n-type (b) TEs on glass fiber fabrics. The composition of the p-type sample remained the same, while the composition of the n-type was changed to $Bi_2Te_{2.85}Se_{0.15}$.

3.6 Figure of Merit (ZT)

With the measured in-plane $S, \sigma,$ and κ, we determined the ZT values for the printed TE layers to be 0.68 and 0.81 for the p-type and n-type printed layers, respectively, as summarized in Table 1. These values are among the highest for the printed TE samples. The high ZT values in our samples can be attributed to the following features of our processes: (1) we minimized the amount of the organic binder present in the printing slurries by using a high viscosity binder (Methocel). (2) The binder was also effectively burnt off during the curing and hot pressing process. (3) For the n-type printed sample, the nanoscale defects left behind after the binder burnt-off contributed to phonon scattering and thermal conductivity reduction, thereby leading to a high ZT value.

Table 3.8　Summary of thermoelectric properties of printed p-type BST and n-type BTS.

	P-type BiSbTe	N-type BiTeSe
S (μV/K)	209	-165
σ (S/cm)	639	763
κ (W/m-K)	1.29($\kappa_{\parallel}$) 1.06($\kappa_{\perp}$)	0.77($\kappa_{\parallel}$) 0.83 ($\kappa_{\perp}$)
κ_L (W/m-K)	0.97	0.37
ZT @ 300 K (using $\kappa_{\parallel}$)	0.65	0.81

3.6.1 Thermoelectric Properties of Bulk Samples
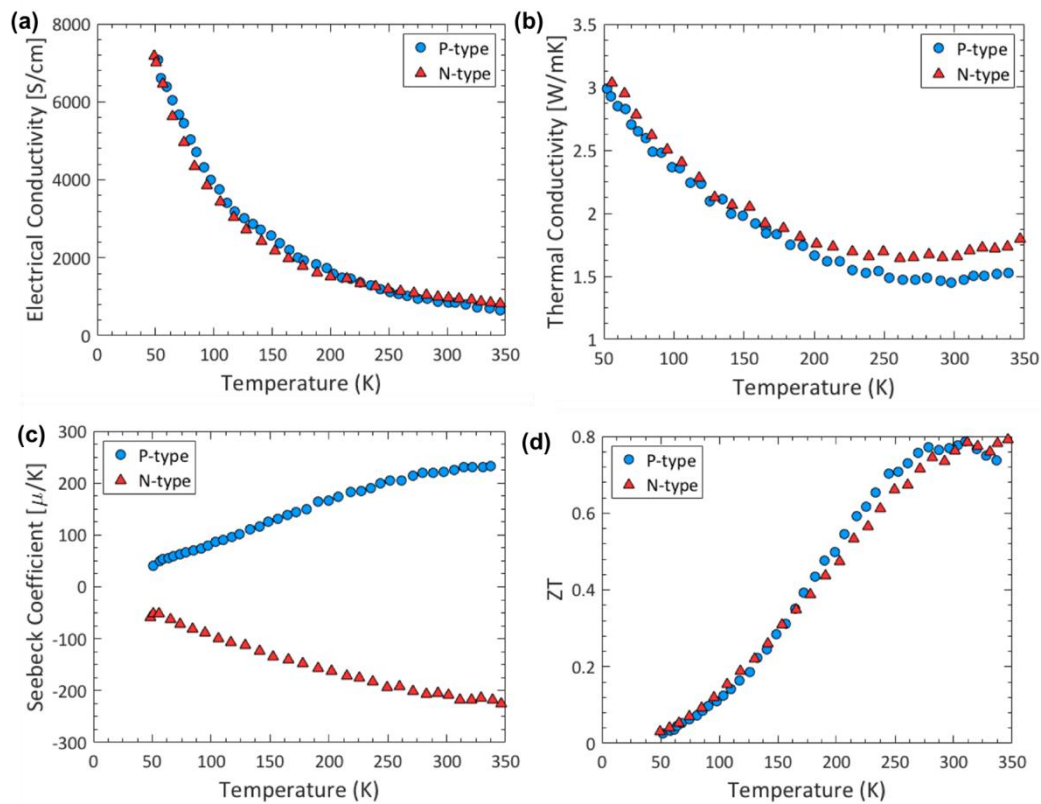
Figure 3.14   Plots of electrical conductivity (a), thermal conductivity (b), Seebeck coefficient (c) and ZT of bulk p-type BST and n-type BTS as a function of temperature.

3.7   Conclusions

We demonstrated printed TE layers with high ZTs for both p-type BST and n-type BTS (i.e., 0.65 and 0.81, respectively), which are close to the bulk values, on flexible glass fabrics. In addition to the high performance and the potential for flexible devices, introducing scale-up processes from preparing TE inks (e.g. spark erosion) to screen printing opens up the opportunities to adopt the TE generator for low-grade heat recovery in wearable devices and personalized thermo-regulation. In this study, we successfully addressed several critical

issues commonly encountered in the printing of TE devices. First, we achieved high-quality printing using a small amount (0.45-0.60 wt. %) of Methocel, an insulating polymeric binder. Second, as the binder has a low decomposition temperature, we effectively burnt off the binders through sintering and hot pressing. The removal of the binders was evidenced from the microstructure analysis and the excellent electrical conductivity. Third, to ensure uniform printing, we also treated porous and rough woven fabrics by printing an interface layer using Chitosan, which enabled the printing of thick TE layers and improved the electrical conductivity. Moreover, we found additional benefit of binder decomposition: it created nanoscale defects that led to low lattice thermal conductivity for the n-type materials. The high-ZT TE layers achieved by printing on flexible fabrics reported in this work could lead to future development of low-cost flexible and wearable TE devices.

Acknowledgements

Chapter 4

Hollow Photonic Structures of Transparent Conducting Oxide with Selective and Tunable Absorptance

4.1   Introduction

Controlling thermal emission in the mid infrared (MIR) range is of great interests for thermal engineering with broad applications ranging from radiative cooling of spacecrafts[103] and terrestrial objects[104,105] to building envelopes[106], and from solar-thermal absorber[107,108] to thermal camouflage[109] and heat shielding (e.g., white roof[110]). In many of these applications, it is often desirable to have selective absorptance in different parts of the spectrum. For example, for many solar utilization devices (such as solar-thermal, thermoelectric, and photovoltaic)[108,111-114], absorption in the solar spectrum is desirable for harvesting solar energy to heat or directly into electricity. On the other hand, for cooling application, it is preferred to have low solar absorption and high infrared emission[104,105,115,116]. Achieving high spectral selectivity is a key strategy to enhance the figure of merit of the thermal absorbers or emitters[86,117]. Therefore, these two opposite applications have adopted different materials, e.g. metals for solar-thermal absorbers and glass for radiative emitters

[104,105,113,118]. Plasmonic materials based on surface phonon polaritons (SPhP), such as SiO_2 and SiC, have been traditional materials of choice to engineer the thermal emission, because its resonant frequency is located at thermal wavelength (~10 μm). SPhP also has much lower optical loss in the MIR compared to surface plasmon polaritons (SPP), which is attractive for some applications such as IR detection[119], where high quality factor is needed. However, for certain applications in thermal absorption/emission, such as solar absorbers and radiative cooling emitters, high optical loss and high extinction coefficient can be taken as an advantage. From this perspective, plasmonic metal structures are particularly suitable. In addition to spectral selectivity, the ability to dynamically tune thermal emission is also desirable in many thermal engineering applications, such as thermochromic windows[120,121] and thermal camouflage. Many of these features are realized by metal-insulator phase transition of VO_2[106,122,123] and related oxide materials[124], as well as conductive polymers[125].

Recently, aluminum-doped ZnO (AZO) and other transparent conductive oxides (TCO) have emerged as an interesting plasmonic material with both spectral selectivity and dynamic tunability. Due to its plasmon frequency residing in the near-IR (NIR) regime, TCO is dielectric (transmitting) in the solar/visible spectrum and metallic (both reflective and absorbing) in the IR spectrum. The cutoff wavelength is determined by the plasmonic frequency described by the Drude model[126-128]. This feature offers a large flexibility when designing thermal infrared structures. Most notably, when the highly reflective feature of the metallic state is used, TCO can be used as a high-transmittance and low-emissivity coating [129]. This coating can be directly applied onto glass to make low-emissivity windows[130] or deposited on a black solar absorber to make spectrally selective solar collectors[131]. AZO has been used for various applications and hence has been prepared with a wide range doping

concentrations from $\sim10^{19}$ cm^{-3} to 10^{21} cm^{-3} by various techniques[126,132-135]. In particular, atomic layer deposition (ALD) has been used to achieve high carrier concentration up to $\sim1\times10^{21}$ cm^{-3} [126]. Also, Ga co-doping can be used to additionally increase the doping level beyond the solubility limit of Al in ZnO[132]. Therefore, the doping concentrations studied here (up to $\sim5\times10^{20}$ cm^{-3}) are well within the experimentally accessible regime.

While TCO was originally used for NIR due to its low loss in this spectrum compared to pure metals[136,137], it is also becoming interesting for MIR applications precisely due to its high loss in this spectral regime, i.e., the absorbing feature of metallic TCO. The infrared properties again can be controlled by tuning the plasma frequency, which can be designed either during the material preparation or dynamically tuned electrostatically. The IR absorption or emission properties can be further engineered by the structures. Various types of photonic structures[138,139] have been developed in the forms of periodic nano/micro-structures and multilayers made of metals and/or dielectrics. For instance, it was recently discovered that three-dimensional (3D) photonic structures of hairs of Saharan silver ants are effective for passive radiative cooling[140,141] with high emittance in the MIR but high reflectance in the visible and NIR regimes. In addition, metamaterials and metasurfaces of TCO have also been utilized to control the IR properties. For instance, it was shown recently that thin metasurfaces of AZO can possess both high IR emissivity (~0.8) and low absorptance in the solar spectrum (~0.16)[103], which is useful for radiative cooling of spacecraft. Owing to the extensive experimental studies of 3D structure with various applications in photonic crystals, drug delivery, soft robotics and so on., the complex structures can be fabricated using dissolvable template[142-144] or 3D printing techniques[145,146].

In this study, we adopted 3D photonic structures of AZO and compare the emissive behavior at room temperature with common bulk blackbody, SiO$_2$. We performed optical modeling to show the effectiveness of tuning the visible and MIR spectral properties independently using both the carrier concentration and structural changes. In addition, with the benefits of the hollow 3D structures, we demonstrated tunable MIR emittance and low solar absorptance.

4.2   Calculations

We started from the permittivity (ε) of AZO. It is well known that the dominant free carriers make the ε of AZO follow the Drude model over the broad energy range, except the high energy in UV region (~300 nm in wavelength) due to inter-band absorption (ZnO bandgap energy is 3.37 eV, or 369 nm), and the relation can be described as[103]:

$$\varepsilon(\omega) = \varepsilon_b - \frac{\omega_p^2}{\omega^2 + i\omega\Gamma} + \frac{f_1\omega_1^2}{\omega_1^2 - \omega^2 + i2\omega\Gamma_1} \tag{4.1}$$

$$\omega_p^2 = \frac{ne^2}{m^*\varepsilon_0} \tag{4.2}$$

where ε_b is permittivity at infinite frequency, ε_0 is permittivity of vacuum, ω_p is plasmon resonance frequency, Γ is damping coefficient followed by the Drude model, f_1 is amplitude, n is carrier concentration, and m^* is effective mass of an electron. ω_1 is spectral position and Γ_1 is damping constant at optical bandgap which follows Tau-Lorenz relation. We can set the resonance frequency out of the dominant solar spectrum to make AZO optically transparent within the solar or visible spectrum.

We then used finite element method (FEM) to simulate the absorptance of 3D triangular structures of AZO and SiO$_2$, as shown in Fig. 4.1(a). Here the triangular structure is used as an example to show the effectiveness of tuning the photothermal properties of 3D AZO structures, and similar ideas can be applied to other structures. We varied the geometry of the triangular structures as well as the carrier concentration in AZO. Perfect conductor was used as a back reflector so as to evaluate the emission and absorption purely from the material of interest (i.e., AZO).
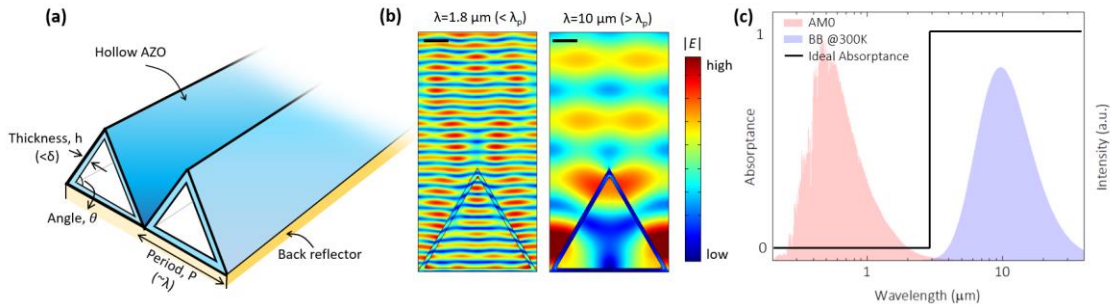
Figure 4.1 (a) A schematic of arrays of hollow triangular cross-section on top of a metal back reflector. The structure has a period of P and wall thickness of h, and angle of θ. (b) Normalized electric field intensity at wavelength of 1.8 μm (left) and 10 μm (right). The scale bar indicates 1 μm. (c) Spectral absorptance or emittance of an ideal emitter which has cutoff wavelength of 3 μm. The filled area shows intensity of solar irradiance (AM0) and Planck's distribution at a 300 K blackbody.

To achieve spectral selectivity, e.g.. low absorptance in the solar/visible spectrum and high emittance in the blackbody spectrum at 300 K, we used two different length scales: skin-depth (δ) and wavelength. For high absorptance in MIR region, structure sizes comparable to wavelengths are required to scatter the infrared, leading to longer effective optical path for stronger light absorption. On the other hand, it is necessary to have the sizes smaller than the

δ of shorter wavelength lights to enhance the transmittance in the visible regime. These two requirements are often contradicting to each other. Even though AZO is dielectric, i.e., non-absorbing, for photons with wavelength shorter than the plasmon wavelength, the structures used for enhancing the IR absorption would still introduce the scattering effect in the visible regime. To mitigate this issue, we used 3D hollow triangular structures, as shown in Fig. 4.1(a). The hollow structures have the primary length scale described by its period (P) comparable to the wavelength of infrared (i.e., a few microns), so as to enhance the scattering and absorption in the MIR regime. In the meantime, the hollow structures have very thin wall, with its thickness (h) much smaller than the skin depth δ of shorter wavelength light for high visible transmittance. This design can decouple the opposite requirements on the length scales for visible transmittance and IR absorptance.

To illustrate this idea quantitatively, we computed the distribution of electric field intensity in a representative hollow triangular structure, as shown in Fig. 4.1(b). A plane wave was used to model the normal incident light, and the figure shows an example of a triangular structure with P of 10 µm and h of 300 nm. As expected, the thickness h is much smaller than the skin depth δ (~10 µm) of AZO in the Vis regime, so there is little absorption of the incident light but only reflection and refraction at the air/AZO interface due to refractive index mismatch. On the other hand, there is enhanced light scattering and trapping in the MIR, thereby we observe the high field intensity confined between neighbor triangular structures. Also, the distinct intensity difference between the outer and inner spaces of the triangle implies significant light absorption inside the hollow structure. This is due to the multiple reflections by the 3D structure and the back reflector. Here we conducted modeling with various cases to achieve spectral selectivity as shown in Fig. 4.1(c), and the results is

discussed in section 3. We aimed to achieve a cutoff wavelength near 3 μm that separates the solar (AM0) and blackbody spectrum at 300 K [Fig. 4.1(c)].

4.3 Results and Discussion

As shown in Eq. (4.1), permittivity ε of TCO is controlled by the carrier concentration. Figs. 4.2(a) and 2(b) displays the real (ε') and imaginary (ε'') part of ε ($\varepsilon = \varepsilon' + i\varepsilon''$), respectively. The plasmon frequency is determined when $\varepsilon'=0$. As expected, as the carrier concentration increases from 5×10^{19} cm^{-3} to 5×10^{20} cm^{-3}, the plasmon wavelength is shifted from ~8 μm to ~2 μm. In addition, higher carrier concentration also results in a larger ε'' at the same wavelength, leading to higher absorption and shorter skin depth δ, as shown in Fig. 4.2(c). We also compared the δ to those of SiO$_2$ in MIR (Fig. 4.2(c)). As mentioned earlier, SiO$_2$ is widely used as an MIR emitting material due to the SPhP resonance within the Reststrahlen band (8 to 9.5 μm). As shown in Fig. 4.2(c), within the narrow Reststrahlen band, δ of SiO$_2$ is comparable to that of AZO. However, outside of this range, SiO$_2$ possesses much larger δ over the broad range. This result indicates that AZO can be a more effective MIR emitting material, especially for a wide range of emitter temperature.
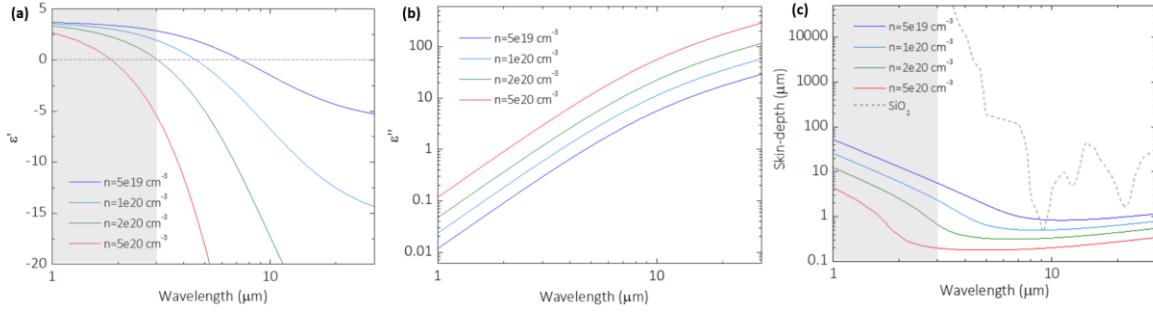
Figure 4.2   Plots of real (a) and imaginary (b) parts of permittivity, and skin-depth (c) as a function of wavelength with various carrier concentrations (n) ranging from 5×10^{19} cm^{-3} to 5×10^{20} cm^{-3}. (c) includes the skin-depth of SiO$_2$ (dashed line) for comparison.

Besides the carrier concentrations, we can also tune the photothermal properties with the structures. In order to show the separate effects of carrier concentrations and 3D photonic structures, we selected two specific carrier concentrations: 5×10^{19} cm^{-3} and 2×10^{20} cm$^{-3,}$ and calculated their spectral absorptance of the solids triangular structures with various periods (P) ranging from 2 to 50 μm, as shown in Fig. 4.3. As expected, for both carrier concentrations, larger P leads to higher absorptance due to the stronger interaction of IR with the larger triangular structures. Also, we can observe a saddle in MIR because of the dips of the skin-depth in these regions [Fig. 4.2(c)]. Therefore, having a suitable primary structural size (P) provides a spectral transition from visible to near-IR regime with the consideration of the skin-depth. On the other hand, the absorptance at the shorter wavelength (e.g., < 3 μm) is significantly reduced for $P \leq$ 10 um (Fig. 4.3), due to the larger δ [Fig. 4.2(c)].
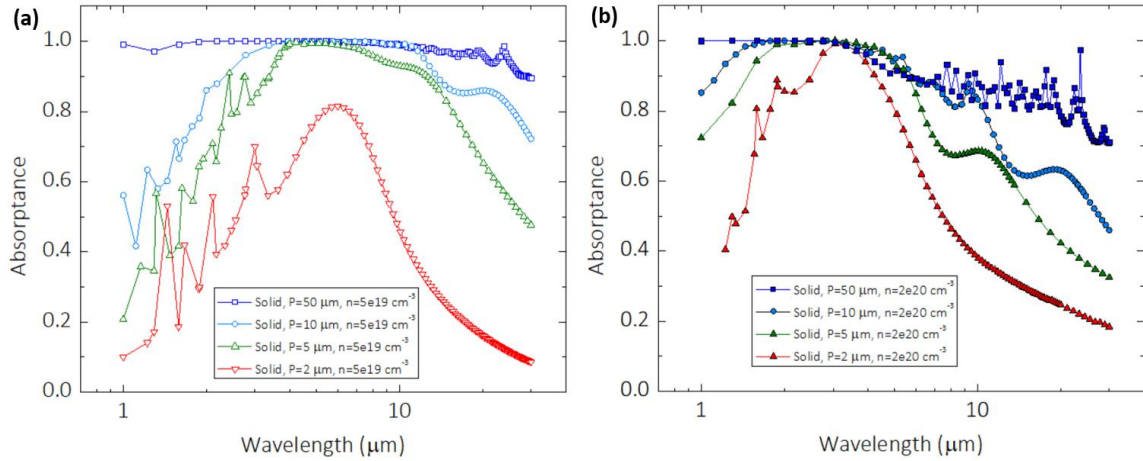
Figure 4.3   Plots of spectral absorptance of solid triangle arrays with various periods (P) ranging from 2 µm to 50 µm with carrier concentration (n) of (a) 5×10^{19} cm^{-3} and (b) 2×10^{20} cm^{-3} at normal incident angle.

The disparity in the absorptance between the NIR and MIR provides an opportunity to engineer the structures of AZO with selective photothermal properties.   For instance, the AZO structures can be placed on a back reflector to reduce the absorption within the solar spectrum while providing high emittance in MIR. However, for solid triangular structures, there is a trade-off for the absorptance between the short and mid wavelength regimes: in order to reduce the absorptance in the shorter wavelength regimes (e.g., < 3 µm) and achieve a sharper spectral selectivity, a smaller structure period P is needed, which would in turn reduce the emittance in MIR.

This trade-off can be mitigated by selectively enhancing the light scattering in longer wavelengths using hollow triangular structures, as shown schematically in Fig. 4.1(a) and illustrated in Fig. 4.1(b). Figure 4.4 shows the comparison of absorptance between solid and hollow triangular structures with P of 5 and 10 µm and carrier concentration of 5×10^{19} cm^{-3}

and 2×10^{20} cm^{-3}, respectively. As can be seen in Fig. 4.4(a) and (b), when the carrier concentration is low (n = 5×10^{19} cm^{-3}), the absorptance of the hollow structures is significantly reduced compared to that of the solid triangles over the entire spectral range, due to the smaller solid volume for light absorption. However, when the carrier concentration is high (n = 2×10^{20} cm^{-3}), while the absorptance in visible and NIR regimes are reduced quite significantly in the hollow structures, the influence on the MIR absorptance is less significant, as shown in Fig. 4.4(c) and (d). The effect of the carrier concentration on the MIR absorptance can also be understood from the skin depth shown in Fig. 4.2c: at $\lambda\sim10$ μm, the skin depths are ~1 μm annd ~400 nm for n = 5×10^{19} cm^{-3} and 2×10^{20} cm^{-3}, respectively. Therefore, the wall thicknesses (300 and 500 nm) in the hollow structures are not sufficient to fully absorb MIR when n = 5×10^{19} cm^{-3}, but are sufficiently thick for high MIR absorptance for n = 2×10^{20} cm^{-3}. Similarly, the large reduction in the visible and NIR absorptance in the case of 2×10^{20} cm^{-3} is also attributed to the larger skin depths in these spectral ranges relative to that in the MIR regime [Fig. 4.2(c)]. Interestingly, for the case of 2×10^{20} cm^{-3}, the MIR absorptance of the hollow structures, despite having the smaller solid volume, still remains high (close to 1), and can even outweigh that of the solid ones within certain spectral ranges, as shown in Figs. 4.4(c-d). This is because the hollow structure acts as an optical cavity surrounded by the metallic surfaces. The higher carrier concentration (e.g. 2×10^{20} cm^{-3}) leads to a more metallic surface as depicted in Fig. 4.2(a). The closed loop of the hollow structure can lead to multiple internal reflections before the light escape from the triangles.
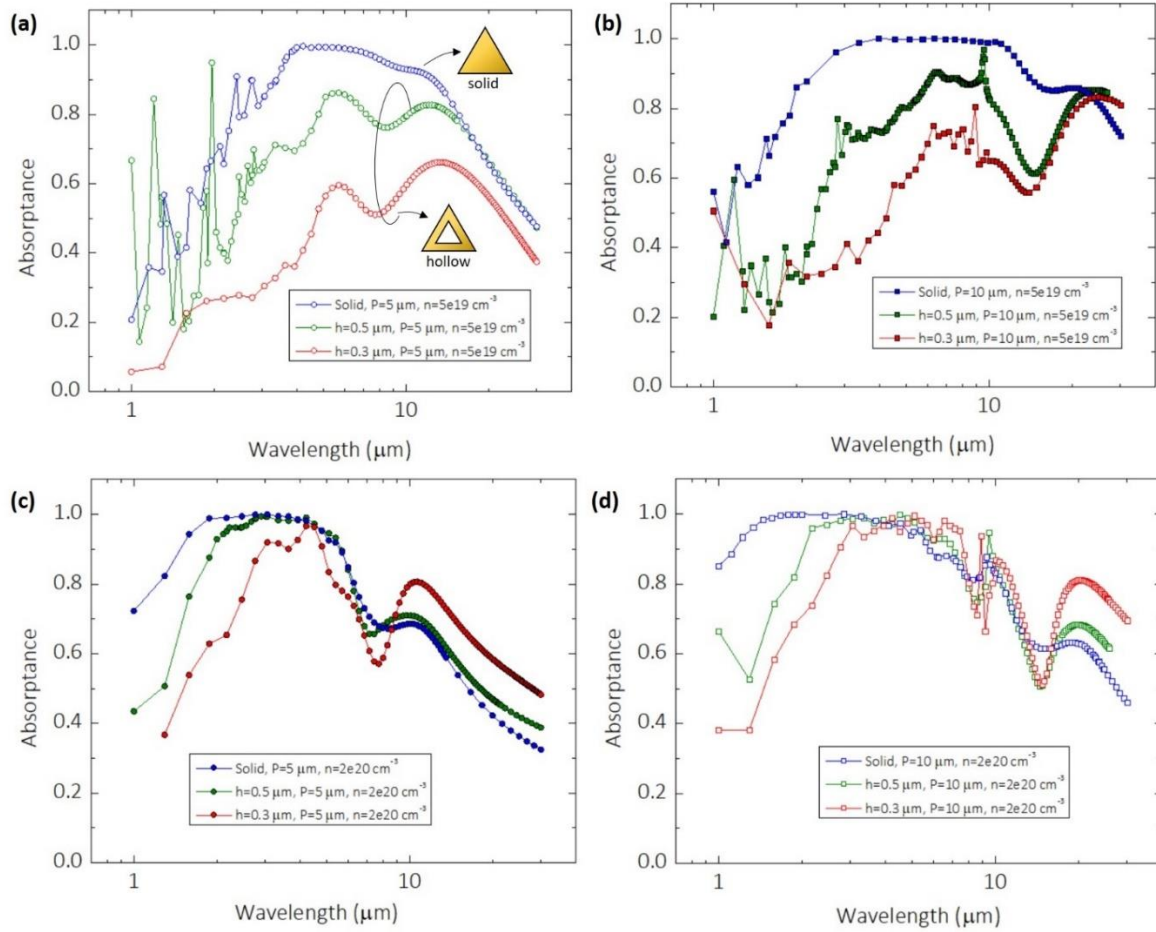
Figure 4.4   Plots of spectral absorptance of solid and hollow triangle arrays with various wall thickness (h), periods (P), and carrier concentration (n) at normal incident angle. (a) $n = 5 \times 10^{19}$ cm^{-3}, $P = 5$ μm; (b) $n = 5 \times 10^{19}$ cm^{-3}, $P = 10$ μm; (c) $n = 2 \times 10^{20}$ cm^{-3}, $P = 5$ μm; (d) $n = 2 \times 10^{20}$ cm^{-3}, $P = 10$ μm.

The hollow structures also offer the ability to dynamic tube the IR emittance by changing the angle (θ) of the triangles. To show this, we modeled the optical properties of the 3D structures with different angles, as shown in Fig. 4.5(a). Owing to the frame-like hollow structures, the structural shape can be easily tuned, for example, by mechanical stretching. The similar technique has been widely used to make flexible electronics using

78

intrinsically rigid materials [147]. Here we fix the surface area and thickness, so the volume of the solid material is identical but the angles of the triangles are adjusted [Fig. 4.5(a)]. As shown in Fig. 4.5(b), the shape of structures strongly affects the MIR absorptance. A smaller angle results in lower IR absorptance. The effects are stronger at the longer wavelength. This change in the spectral absorptance will lead to a large change in the overall emissivity. For example, for a 300 K blackbody, the emissivity (ε_{300K}) can be calculated as,

$$\varepsilon_{300K} = \frac{\int A(\lambda) I_{BB}(\lambda) T(\lambda) d\lambda}{\int I_{BB}(\lambda) T(\lambda) d\lambda} \tag{3}$$

where $A(\lambda)$ is the spectral absorptivity, and I_{BB} is blackbody distribution at 300 K. The calculated effective emissivity is shown in Fig. 4.5(b). We can observe the large emissivity change as a function of the angle θ: emissivity can vary from 0.14 to 0.8 when the angle changes from 10 to 80 degree. This large emissivity tunability highlights another unique feature of the 3D hollow AZO structures.
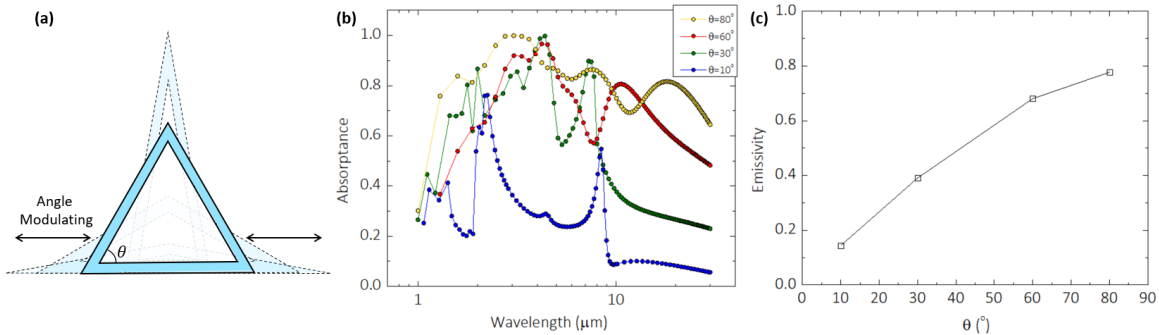
Figure 4.5   (a) Schematics of hollow structures with different angles (θ). (b) Spectral absorptance of the hollow structures with different angles at normal incident angle. (c) Emissivity of hollow structures with various θ, weighted by Planck's distribution of a 300K blackbody.

The enhanced spectral selectivity of the hollow structures is evidenced by examining their absorptance in the solar spectrum, which was modeled on the optimal design for the highest MIR absorptance, namely, with n of 2×10^{20} cm^{-3} and the wall h of 0.3 μm and P of 5 μm. Here, the absorptance in the solar spectrum (α_S) is calculated via:

$$\alpha_S = \frac{\int A(\lambda)I_S(\lambda)d\lambda}{\int I_S(\lambda)d\lambda} \tag{4}$$

where $A(\lambda)$ is the spectral absorptivity and I_S is solar irradiance intensity (AM0). As seen in Fig. 4.6(a), the solid AZO triangular structure has higher absorptance in the UV-vis-NIR region. The high absorption below 300 nm is due to the intra-band energy transition in AZO. However, the hollow AZO triangular structures have much lower solar absorptance. The solar absorptance is insensitive to the angle θ of the hollow structures: it is around 0.33 for $\theta = 10$-60°, which is about half of that of the solid triangles. This reduction in the solar absorptance can be attributed to the reduced solid light absorbing volume in the hollow structures. On the other hand, for the hollow triangles with $\theta = 60°$, the IR emittance is even increased from 0.59 to 0.68.
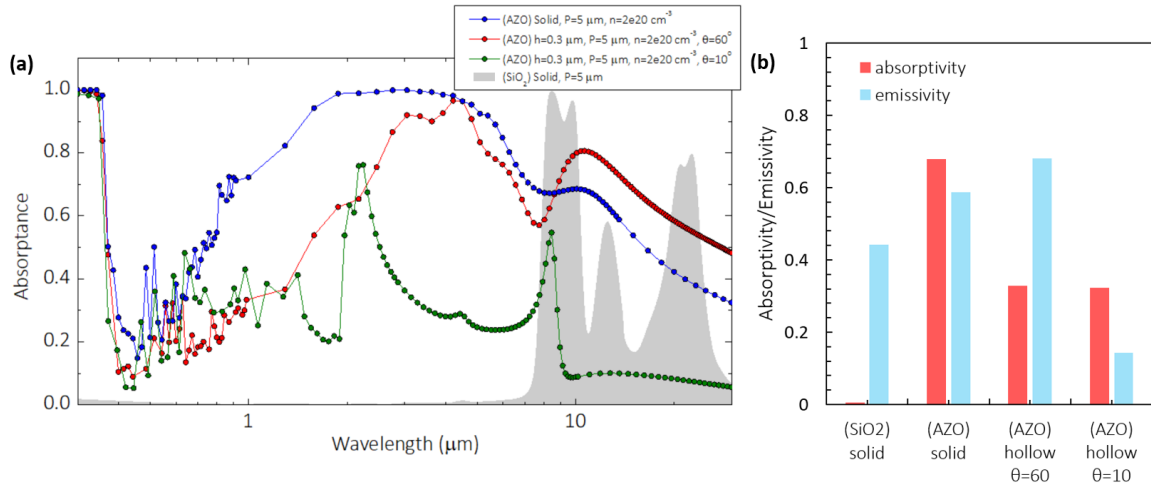
Figure 4.6   (a) Absorptance as a function of wavelength including UV-Vis to IR regime at normal incident angle. (b) Absorptivity and emissivity weighted by solar irradiance and Planck's distribution of a 300K blackbody, respectively.

Compared to the more common IR emitting material in SiO_2, AZO has much shorter skin-depth due to the broadband plasmonic effect [Fig. 4.2(c) and Fig. 4.6(a)]. As a result, both the hollow and solid AZO structures have higher overall ε_{300K} values compared to that of SiO_2, which is ~0.44. With the structures we computed here, the α_S of the hollow structures is still much higher than that of SiO_2 [0.33 vs. 0.01, in Fig. 4.6(b)], due to the nearly-zero loss of dielectric SiO_2 in the solar spectrum [Fig. 4.6(a)). Therefore, more optimization needs to be done if one would like to further reduce the solar absorptance of AZO structures.

Furthermore, we studied the emissive behavior with different incident angles, α. The spectral response of angular dependence showed similar behaviors between solid and hollow structures. Also, the hollow structures showed higher emissivity than the solid ones in all the angles owing to their more efficient light trapping effect. As the incident angle was lowered

81

from the normal direction ($\alpha=90^o$), the directional total emissivity (weighted by 300 K blackbody spectrum) was only slightly reduced, by 31% and 24% for the solid and hollow structures, respectively. This small decrease in the directional emissivity would not lead to a big change in the total hemispherical emissivity, because the latter is more dominantly influenced by the high incident angles due to the $\sin(\alpha)$ factor.
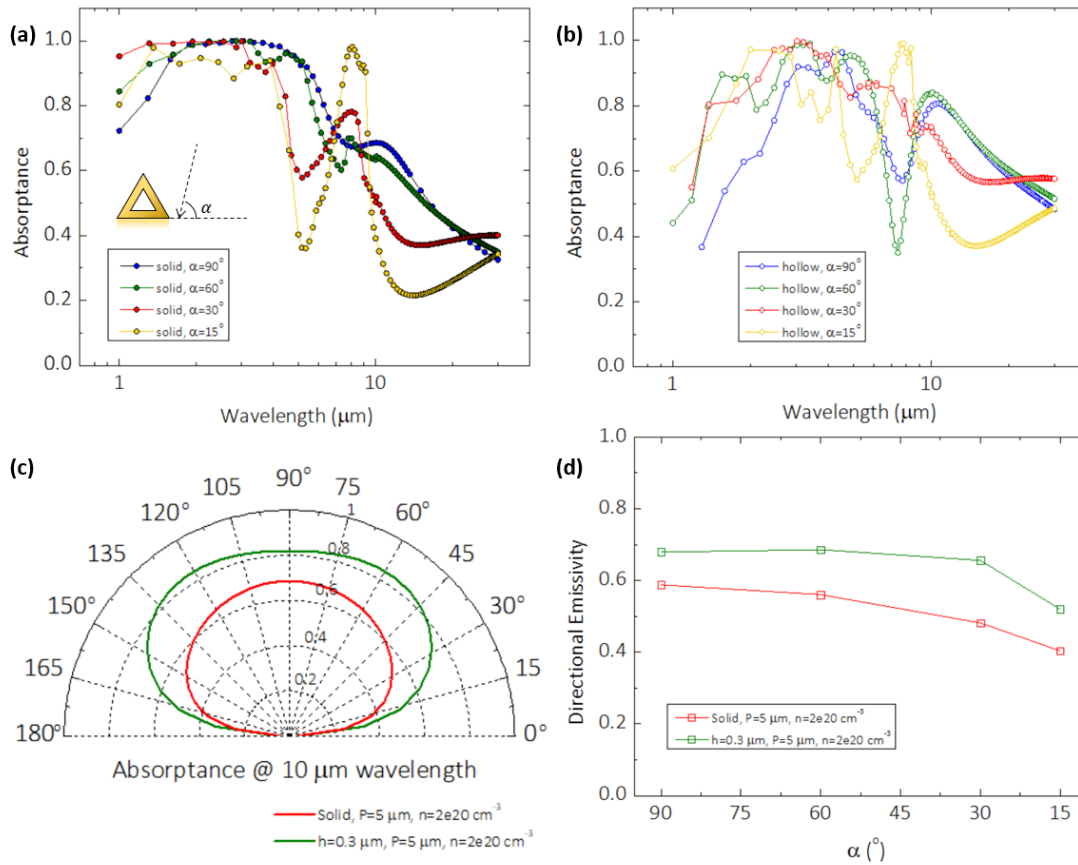
Figure 4.7 Spectral absorptance of the solid (a) and hollow (b) structures with different incident angles, α, ranging from 15° to 90°. (c) Absorptance at 10 µm wavelength as a function of incident angles for solid (red) and hollow (green) structures. (d) Directional emissivity weighted by Planck's distribution of a 300 K blackbody as a function of incident angles.

4.4 Conclusions

In summary, we studied the optical properties of solid and hollow 3D structures of AZO with various carrier concentrations and geometrical factors. As the plasmon frequency and the skin depth of AZO are tunable by varying the carrier concentration, we can design certain structures with selective absorptance. We showed that 3D hollow structures of AZO can be engineered into selective emitter with higher IR emissivity and lower solar absorptance compared to the solid counterparts. This is because the large periods of the triangular array (~ several microns) can have strong interaction with MIR and the small wall thickness of the hollow triangles lead to low absorption volume for visible and NIR. When the carrier concentration is high, the MIR absorptance in the hollow structures can be even increased over that of the solid ones, which can be attributed to the short skin depth in MIR caused by the high carrier concentration and the multiple reflections inside the hollow cavities. Furthermore, the IR emissivity of the hollow structures can be tuned within a large range, from 0.14 to 0.80, by changing the angles. The selective and tunable absorptance of 3D AZO hollow structures may find useful applications in thermal management and energy conversion.

Acknowledgements

Chapter 5

Far-Field Coherent Thermal Emission From Polaritonic Resonance in Individual Anisotropic Nanoribbons

5.1   Introduction

Thermal radiation, as described by Planck's law, is generally considered incandescent in classic textbooks. However, as Planck himself originally noted[148], the emitting energy distribution, including the broadband nature in both spectral and spatial domains, no longer holds if the characteristic size is smaller than the thermal wavelength (λ_T~10 μm at room temperature). Recent rapid development in near-field radiative heat transfer[149-153] has revealed extraordinary behaviours when the distance between the emitter and receiver is smaller than λ_T, including giant enhancement in the heat flux and a coherent feature resulting from the tunnelling of evanescent waves by surface phonon polaritons (SPhPs) or surface plasmon polaritons (SPPs). Although coherence has been extensively investigated in the near field via evanescent waves, observation of coherence in far-field is still significantly limited. Far-field emission from an emitter with a size smaller than λ_T can result in polarised thermal emission that could be relevant for broader applications for which the near-field gap

is inaccessible.[154-160] Recent work has shown the feasibility of spectral and spatial control of far-field thermal emission from engineered microstructures. For instance, Greffet *et al.* demonstrated coherent emission, featured with a narrow spectral and angular range, achieved by the grating of a polaritonic material (i.e., SiC) with a grating period comparable to λ_T to couple to SPhPs.[161] More recently, through fluctuational electrodynamics modelling, Fernández-Hurtado *et al.*[162] showed highly directional emissivity from anisotropic polaritonic structures, which was found to originate from the guided modes whose dispersion relation becomes highly dispersive around the Reststrahlen band. This feature resulted in super-Planckian thermal radiation between two anisotropic objects when they are oriented along the dominant emission direction, which was also experimentally demonstrated by Thompson *et al.*[163]

These earlier findings provide important insights into the design of an emitter with coherent far-field thermal emission. To achieve dominantly coherent thermal emission in the far field, it is desirable to quench the incoherent emission. Bulk polar dielectric materials, such as SiO_2, generally behave like a blackbody in the broad infrared (IR) range, except within the Reststrahlen band[164] (negative permittivity) that shows high reflectance (Fig. 5.1(b)). For SiO_2, the skin depth (δ) at 10-μm wavelength is on the order of 1 μm[165]. Therefore, one could utilise an emitter smaller than δ to suppress the broadband emission. This volumetric absorption regime was theoretically studied by Golyk *et al.*[165] for cylindrical SiO_2 and SiC nanorods, where the incoherent emission was greatly suppressed from the near-blackbody limit for rod diameters much smaller than δ. However, the small rod diameter, now also much smaller than λ_T, would limit the resonant effect and diminish the potential

coherent thermal emission. Due to this constraint, previously studied nanorods showing the unusual polarised thermal radiation behaviours would all have low overall emissivity[165-168], as modelled by Golyk et al.[165].

Here, we seek to design a nanoscale emitter that quenches the incoherent broadband emission without compromising the coherent resonance. Our strategy is to exploit another degree of anisotropy using rectangular polar dielectric nanoribbons, which have two characteristic length scales, the thickness and width, to separately match δ and λ_T, respectively. As shown in Fig. 5.1(a), we utilised a much smaller thickness (100 nm) relative to δ to suppress the broadband incoherent thermal emission originated from the volumetric effect in cylindrical nanorods[165,166]. Moreover, we designed the width of the nanoribbons to be comparable to λ_T, which is expected to result in enhanced coherent thermal emission because of resonance of the SPhPs. Guided modes by SPhPs shrink the wavelength (λ_{SPhP}) at the surface, as shown in Fig. 5.1(c); furthermore, the finite cross-section determined by the width and thickness intensifies the absorption efficiency. A size comparable to integer multiples of the half wavelength maximises the resonant enhancement. With this design, we can simultaneously enhance the coherent emission and quench the background broadband emission, thereby achieving dominantly coherent thermal emission within the narrow Reststrahlen band.
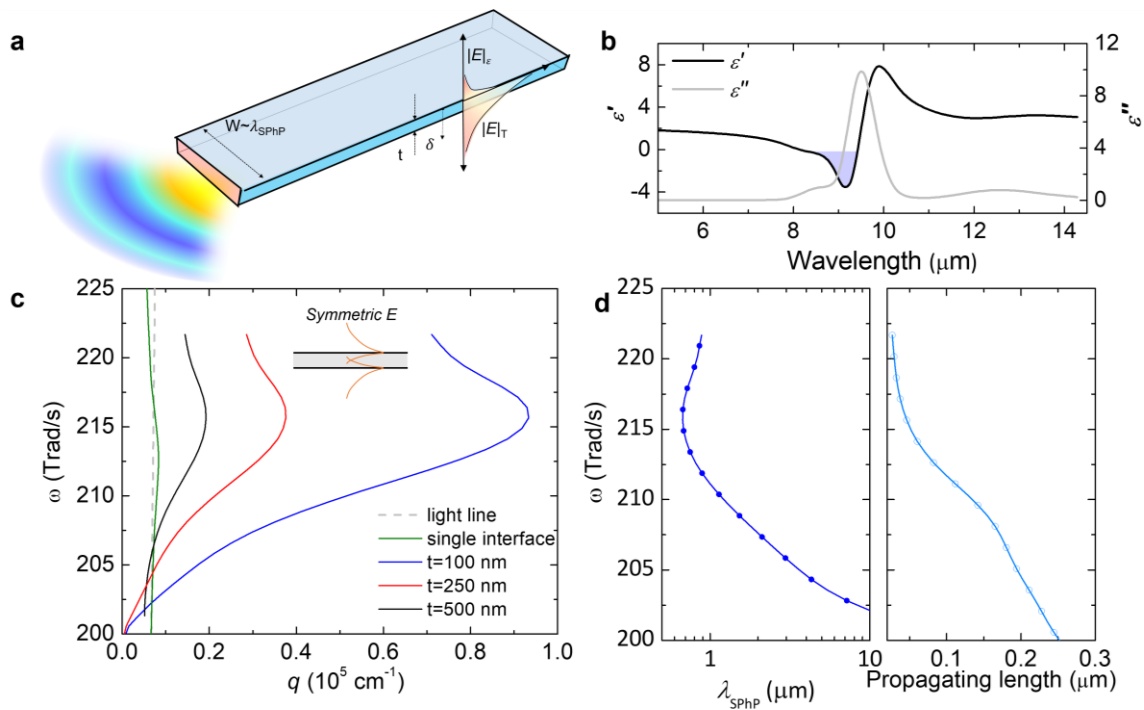
Figure 5.1 Anisotropic nanoribbon for localised resonance by polaritons. a, Schematic illustration of a long nanoribbon with rectangular cross section with thickness (t) and width (W). Here, t is thinner than the skin depth (δ), leading to significant transmitted intensity of the electromagnetic wave perpendicular to the ribbon ($|E|_T$) compared with the absorbed intensity ($|E|_\varepsilon$). Otherwise, the optical response in the parallel direction to the plane would yield higher emission because the cross-sectional length scale with the integer multiples of half wavelength supports the localised resonance modes, enhancing the absorption cross-section. b, Plots of the real and imaginary permittivity of SiO_2. The region of the Reststrahlen band is coloured. c, Dispersion relation of SPhP supported by thin films of different thickness, calculated from the approximate solution (Eq. 4.1). The energy range is within the Reststrahlen band. d, SPhP wavelength and propagating length for a 100 nm thick thin film, corresponding to the dispersion curve.

A perceived experimental challenge to directly probing the thermal emission from these emitters is the exceedingly low emitting power (down to nW, assuming 10-μm width, 100-μm length, 100-nm thickness, $\varepsilon = 0.2$, $T = 100–400$ K). To our knowledge, direct thermal emissivity (ε) measurements from dielectric nanoheaters have not yet been achieved because

of the low emissive power. Prior ε measurements have only been achieved on metallic nanoheaters, such as W, Pt, and carbon nanotubes,[156,157,168,169] where the specimen also served as a joule heater and thermometer. Measurements on these metallic nanostructures revealed the important role of SPP resonance on emissivity. However, due to the high frequency of SPPs, their effect is only important at elevated temperature. Unfortunately, the dielectric itself cannot provide heating or thermometry, and any metallic addenda could impact the emission properties of the nanoscale specimen. Although recent scanning probe techniques[158,164,170] have enabled the detection of local near-field radiation intensity from nanoscale objects[171], these measurements are not suitable for far-field. Far-field optical measurements of thermal emission (e.g., Fourier-transform infrared spectroscopy) require a substrate and must be performed at high temperature to obtain detectable infrared signals,[156,157,161] both of which can alter the emission behaviours. The substrate itself could introduce parasitic signals by refraction and reflection at the interface,[172] and the thermalisation at high temperature could reduce the quality (Q) factor because of the reduced lifetime of optical phonons[173,174].

In this work, to directly measure the far-field thermal emissivity, ε, from single anisotropic nanoribbons of polar dielectrics with a perceived high degree of coherent thermal emission, we devise a novel thermometry platform by combining a fin model with sensitive thermometry. This platform allows us to observe over 8.5-fold enhancement in ε of SiO_2 nanoribbons compared with that of thin-film SiO_2 of the same thickness. Importantly, through experimental observation and computational analysis, we are able to attribute this enhancement to the coherent resonant effect of SPhPs enabled by the anisotropic nanoribbon design. This resonance effect is further confirmed by the observed increasing emissivity at

lower temperature, as the suppression of phonon broadening and increased phonon life time

at low temperature lead to enhancement of the coherence and Q factor.

5.2   Design of Anisotropic Nanoribbons

We designed the anisotropic nanoribbons based on the relevant length scales of δ[165]

and λ_{SPhP}, as shown in Fig. 5.1(a). The thickness of the ribbons was fixed at 100 nm to

suppress the broadband emission. We estimated the volumetric emissivity to be 0.062 for this

thickness at room temperature, which is much smaller than the bulk emissivity (~0.9). The

design of the width of the ribbon was dependent on λ_{SPhP}. It should be noted that the

wavelength of SPhPs at the SiO_2/vacuum interface is different from that in free space (~10

μm); it is dependent on the geometry of the SiO_2 ribbons because the dispersion of SPhPs is

now controlled by the coupling between the optical phonon in SiO_2 and photons. We

determined the dispersion of a thin film using the following analytical formula (see

Supplementary Note 8):

$$\frac{\varepsilon_{SiO_2}}{\varepsilon_0} = -\frac{k_{t,SiO_2}}{k_{t,0}}\coth(\frac{t}{2i}k_{t,SiO_2}),\tag{5.1}$$

where ε_0 and ε_{SiO_2} $(=\varepsilon'+i\varepsilon'')$ are the permittivity in vacuum and SiO_2,[175] respectively;

$k_{t,i}$ is the transverse vector $(k_{t,i}^2 + k_p^2 = \varepsilon_i k_0^2)$ in the medium i; k_p is the propagating vector

along the surface ($k_p = q+i\kappa$, where q and κ are the real and imaginary part of the

momentum vector, respectively); and k_0 is the free space vector. Eq. (5.1) is the solution for

the even modes of two branches of the surface waves by electric fields at the top and bottom

surfaces, and this case represents the dominant contributions for the efficient absorption by confining the energy from the free space into the small physical cross-section area.[176] The confinement becomes more significant with a smaller thickness, due to the stronger interaction of the two symmetric evanescent surface waves (Fig. 5.1(c)). The analytical equations are summarized in the Supplementary Information for the major available fundamental modes by different polarizations (namely, symmetric TM, asymmetric TM, and TE modes). The calculated dispersions, shown in Fig. 5.1(c), indicate that the wavelength of SPhPs ranges from 0.8 to 1.8 μm, which is approximately 5–10 times smaller than the free-space wavelength, for a SiO_2 layer thickness of 100 nm. We designed the width (e.g., ~5 and 10 μm) to cover the integer multiples of the half wavelength of SPhP, to study the size effect on the resonant enhancement. The realised widths on the fabricated nanoribbons were 11.5 and 6.28 μm (Fig. 5.2).
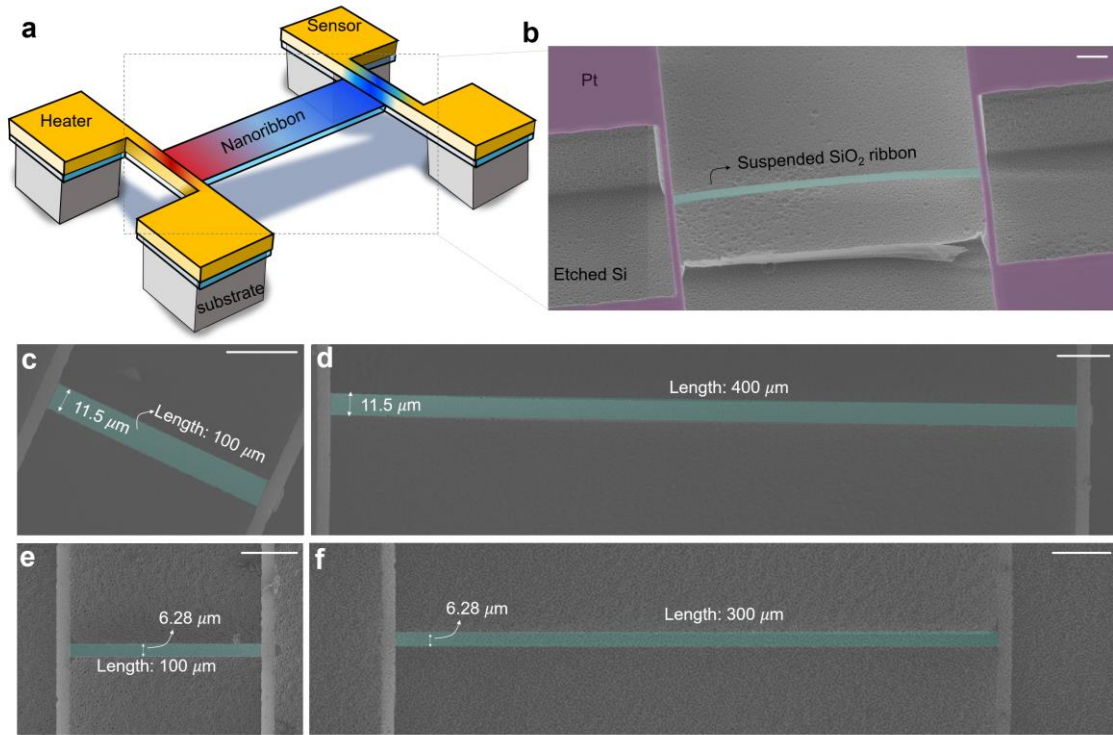
Figure 5.2 Suspended thermal transport measurement micro-device with monolithic SiO_2 nanoribbon. (a) Schematic illustration and (b) SEM image of the device showing the suspended heater and sensor electrodes (Pt) and a monolithic SiO_2 nanoribbon across the electrodes. (c–f) SEM images of SiO_2 nanoribbons of various sizes. All the scale bars represent 30 μm.

5.3 Direct Thermal Emissivity Measurement Platform

We developed a microscale thermometry platform to measure the radiative heat loss of single SiO_2 nanoribbons, as shown in Figs. 5.2(a)–(f). We used a suspended device such that the emission comes entirely from the nanoribbon without any influence of a substrate. We also implemented a modulated AC heating technique (Fig. 5.3(b)) to achieve sensitive thermometry with ~0.1 mK resolution[177-179]. The basic idea to extract the radiative heat loss

was to utilise the thermal fin model by systematically varying the length of the ribbons. Considering heat conduction along the length (L) of a nanoribbon with consideration of the radiative heat loss characterised by the heat transfer coefficient h, where $h = 4\varepsilon\sigma T^3$ (ε is the emissivity, σ is the Stefan–Boltzmann constant, and T is the temperature), the temperature rise along the ribbon can be described by the fin model:

$$\theta = \theta_h \cosh(mx) + \frac{\theta_s - \theta_h \cosh(mL)}{\sinh(mL)} \sinh(mx). \tag{5.2}$$

Here, θ ($\equiv T - T_0$) is the temperature rise from the ambient temperature (T_0) as a function of the x-coordinate along the length (L); θ_h and θ_s are the temperature rise at the hot and cold reservoirs, respectively; and m is the fin parameter:

$$m = \sqrt{\frac{hP}{\kappa A_c}}. \tag{5.3}$$

Here, κ is the intrinsic thermal conductivity of the ribbon, and P and A_c are the perimeter and cross-sectional area, respectively. The fin model notably allows us to quantitatively describe the combined energy transfer of light and heat in the form of radiation out of the surface and conduction through the volume. We summarise the temperature rise ratio of heating to the sensing side, γ, as

$$\frac{\theta_s}{\theta_h} = \frac{1}{\cosh(mL) + \dfrac{G_b}{\kappa A_c m} \sinh(mL)} \equiv \gamma. \tag{5.4}$$

In the absence of radiative heat loss, m becomes zero; therefore, Eq. (5.4) can be simplified as

$$\left. \frac{\theta_s}{\theta_h} \right|_{m=0} = \frac{G_s}{G_b + G_s} \equiv \gamma_{\text{lossless}}, \tag{5.5}$$

where G_s ($=\kappa A_c/L$) is the thermal conductance of the sample and G_b is the thermal conductance of metal beams (see Supplementary Note 4). Finally, we can define the ratio of γ to $\gamma_{lossless}$ as Δ ($=\gamma/\gamma_{lossless}$), where $\gamma_{lossless}$ is determined using short samples with bulk thermal conductivity. By comparing the Δ of samples with varying lengths, as shown in Fig. 5.2 and Fig. 5.3(a), we can determine m and eventually h and ε.

The measured apparent thermal conductance includes the overall influences of both heat propagation through the solid volume and radiation out of the surface (G_{rad}). To apply this measurement technique to low-dimensional materials, high-resolution thermometry is needed to resolve the radiative loss from the net thermal conductance. It is especially important to be able to detect the emissive power even with a small amount of heating, as we want to avoid a large deviation from the theoretical estimation, where the optical parameters are assumed to be identical to the values at room temperature. Using this novel approach, which bridges thermal and optical phenomena to measure the radiative heat loss, we were able to measure ε of a single isolated nanostructure, e.g., a nanoribbon, for the first time, without the effect of a substrate.
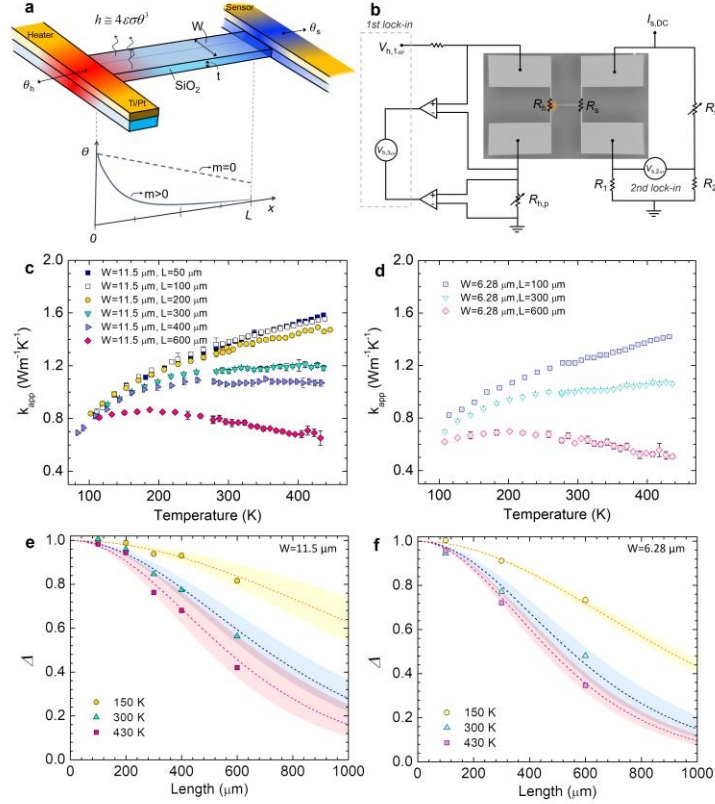
Figure 5.3   Thermal transport measurement methodology and results. a, Schematic illustration of heat-transfer process in the suspended micro-device with SiO_2 nanoribbon overlaid with the colour code representing the temperature rise (θ) on the heater, sensor, and nanoribbon. The schematic plot at the bottom presents profiles of θ along the ribbon: when there is no heat loss (the fin parameter $m = 0$), the θ profile is a straight line (dashed line), and when there is radiative heat loss ($m > 0$), θ is exponentially decayed along the length (solid line). b, AC modulated heating scheme. The heating beam is heated by a 1ω current, and the corresponding resistance change (ΔR_h) due to the temperature rise is measured from the 3ω voltage. The sensing beam resistance change, ΔR_s, was measured from the 2ω voltage using a small DC excitation current ($I_{s,DC}$). A Wheatstone bridge configuration was used on the sensing side to increase the measurement sensitivity. c–d, Plots of measured apparent thermal conductivity (k_{app}) vs. temperature   for nanoribbon widths of 11.5 μm (c) and 6.28 μm (d). k_{app} was calculated using Eq. 5.6, which assumes a linear temperature profile along the ribbon (i.e., the dashed line in a with m=0 or no radiation heat loss). The further below k_{app} is from the true thermal conductivity of SiO_2, the larger the radiative heat loss. The error bars were determined by the standard deviations from the conductance measurement. e–f, Plots of temperature ratios, Δ, between the heating and sensing beams as a function of temperature. Δ is defined as $\gamma/\gamma_{lossless}$ and is a measure of the radiative heat loss. The experimental results (symbols) are compared to the fitted fin model (dotted lines), and the coloured area indicates the uncertainties of the fitted emissivity values.

As a a calibration of our fin technique to extract thermal emissivity, we also conducted a similar experiment with a rectangular beam cross section which have larger thickness (~10 μm) than that of the ribbons as well as the skin-depth (~1 μm), such that the thermal radiation would follow the incoherent (broadband) bulk-like emission spectrum and the emissivity is expected to be close to the bulk value of SiO_2 (~0.9 at room temperature). We extracted the emissivity using the fin model following the same procedure described above. Firstly, we designed the thick SiO_2 length for 10 μm thick beams. To determine the suitable beam lengths to emphasize the radiative heat loss, we estimated thermal conductance by heat conduction and radiation with an assumed emissivity of 0.9. Figure 5.9 shows that radiative conductance would be significant relative to heat conduction when the beam length is around 800 μm or longer. Thus, we fabricated the suspended SiO_2 beams with various lengths, namely, 100, 400, 600, and 800 μm, as shown in Fig. 5.10. With these various lengths, we measured thermal conductivity of the beams, as shown in Fig. 5.11. We analyzed temperature ratios between the heating and sensing sides, γ, at each length. At the smallest length (100 μm), we obtained thermal conductivity of 1.41 W m^{-1} K^{-1} at room temperature. At this length, the radiation is negligible (see Fig. 5.9) and the measured thermal conductivity agrees well with the expected bulk value of SiO_2. This validates our heat transfer measurements. By using the thermal conductivity value of the shortest beam or the bulk SiO_2 (~1.4 W m^{-1} K^{-1}), Δ was calculated as shown in Supplementary Fig. 5.11(b). Using the same fin model that fits all the sample lengths with a single fitting parameter in the emissivity, we found the best fit with an emissivity value of 0.77 (±0.07) for the 7.5 μm wide and 10 μm thick beams. This value agrees well with the theoretical expectation. For example, Golyk et al.[165] estimated an emissivity of around 0.7 for a cylindrical rod with 5 μm radius. The small discrepancy is

likely due to the different cross sectional geometries (rectangular in our experiment vs. cylindrical in Golyk *et al.*) as well as the surface roughness of our samples.

5.4   Apparent Thermal Conductivity of Individual SiO$_2$ Nanoribbons

Because amorphous SiO$_2$ ribbons were used, we could calibrate the new measurement technique on short samples (e.g., L=50 or 100 µm) with negligible radiative heat loss. SiO$_2$ is an ideal candidate to evaluate a new platform for heat-transfer measurement because it has very short phonon mean free paths (~1 nm at room temperature)[180,181]. Therefore, bulk-like thermal conductivity (1.3–1.4 W m^{-1} K^{-1} at 300 K) is maintained even at the nanometre scale, as experimentally confirmed by us on SiO$_2$ nanotubes with shell thicknesses down to 7.7 nm[178]. For samples with longer length, γ would be larger, and the measured apparent thermal conductivity would deviate from the intrinsic κ of SiO$_2$, the difference in which is due to the radiative heat loss. Here, the apparent thermal conductivity is defined as $\kappa_{app} = G_{app}L/A_c$, where

$$G_{app} = G_b \frac{\theta_s}{\theta_h - \theta_s}.$$
(5.6)

When there is radiative heat loss (m>0), G_{app} in Eq. (5.6) deviates from the true G_s. Thus, by comparing the measured κ_{app} to the intrinsic value for SiO$_2$, we can directly illustrate the importance of thermal radiation.

Figs. 5.3(c)-(d) shows the temperature-dependent κ_{app}. Indeed, we observed saturated phonon thermal conductivity in a relatively short length up to 100 μm, which is the same as the bulk value. κ_{app} clearly decreased with longer lengths as a result of the enlarged radiative heat loss, which becomes more pronounced at higher temperature. In general, κ_{app} with various lengths converges to the bulk value at lower temperature, indicating the reducing radiative heat loss, as expected.

5.5 Radiative Behavior of SiO$_2$ Nanoribbons

We compared the relative change among samples with various lengths covering the conduction- and radiation-dominant regimes by utilising the *m* parameter, which quantifies the degree of radiative loss. Figs. 5.3(e) and 5.3(f) present the experimental and fitted Δ values based on the fin model with two different widths, 11.5 and 6.28 μm, respectively. A longer ribbon resulted in lower Δ because of the larger radiation heat loss relative to the heat conduction. However, Δ was close to ~1 for the short samples (e.g., L = 50 and 100 μm) because of the negligible radiative loss. Similarly, we plotted Δ at different temperatures, and, as expected, higher temperature generated lower Δ. To extract ε, we directly compared the experimental and fitted Δ values. We used a single ε value to fit all the samples with the same width but different lengths. The dashed line in Fig. 5.3 represents the Δ value based on the averaged ε value showing the best fit over the entire length range, and the shaded area indicates the uncertainty of the fitting. The uncertainty could originate from the slight variation in the actual widths of the fabricated samples with different lengths. Also, it may

include the length-dependent behaviour with the nature of broad range of propagating length as we shall see later. The temperature-dependent ε values were determined by repeating the same fitting process for all the samples measured at different temperatures. To avoid any contribution from the surroundings, we employed triple radiation shields in a vacuum chamber to ensure the surrounding temperature is the same as the sample temperature.

Figure 5.4 presents the extracted ε values at room temperature for ribbons with widths of 6.28 and 11.5 µm. In addition, the ε of a 100-nm-thick film was analytically calculated to provide a baseline for comparison with the ribbons (Supplementary Figs. 5.17-5.19). Here, we observed two effects associated with the low dimensions in SiO_2 nanoribbons. First, the effective ε of the ribbons was significantly lower than that of the bulk SiO_2 because the 100-nm thickness was much smaller than δ of SiO_2 (~1 µm at 300 K). However, more interestingly, a higher ε was observed for the nanoribbons than for a film of the same thickness. Furthermore, a larger enhancement in ε compared with the thin-film limit was observed for the ribbon with smaller width, 6.28 µm, which implies that a narrower width increases the resonance effect. These results can be explained by the localised resonant effect by SPhPs combined with the directional emission via the waveguided modes, which enhances σ_{abs}, as we shall discuss next.
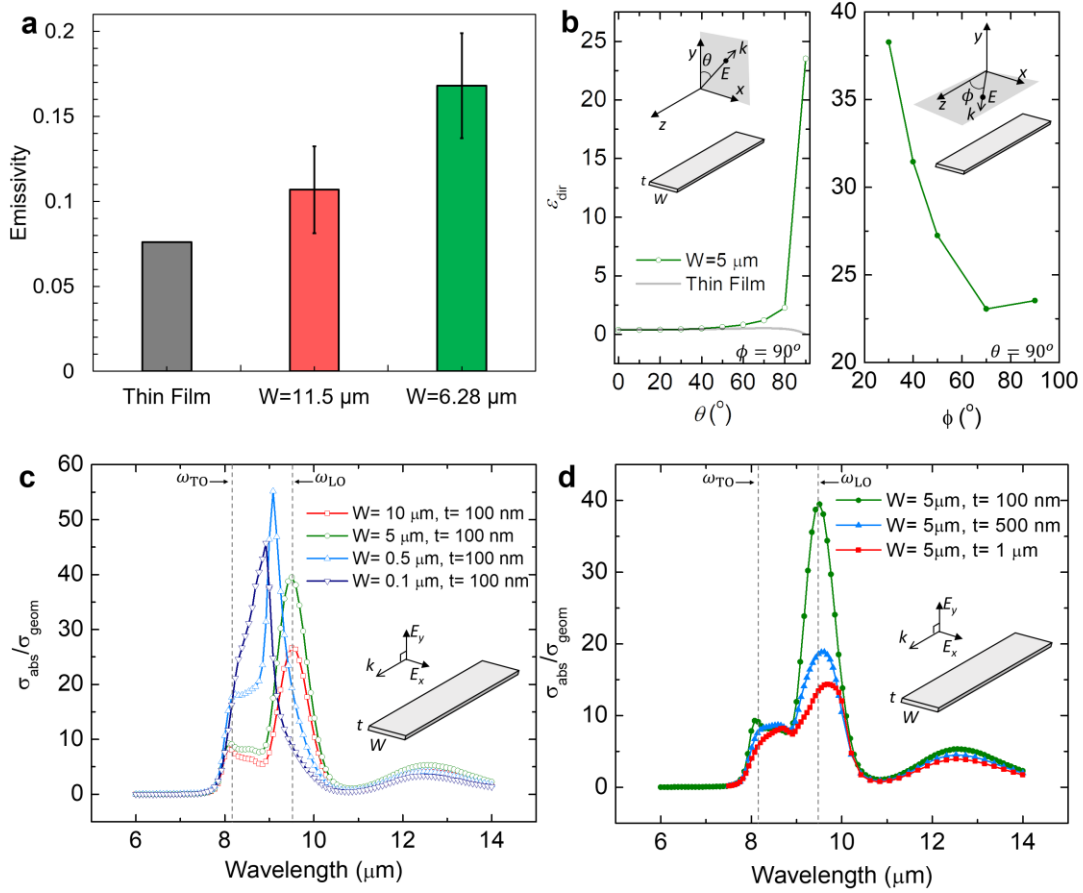
Figure 5.4 Enhanced emissivity with anisotropic nanoribbons. a, Plots of the extracted emissivity at room temperature for ribbon widths of 6.28 and 11.5 μm, where the error bars are corresponding to the uncertainty in the fitting as shown in Figs. 5.3(e)-(f). The grey bar represents the computed emissivity of an infinitely wide thin film of the same thickness as the ribbons, i.e., 100 nm. b, Plots of directional emissivity (ε_{dir}) of a nanoribbon with W= 5 μm at a wavelength of 9.5 μm, where the incoming plane wave has propagation (k) directions where the polarisation directions are normal to k in x-y plane and x-z plane, respectively for each φ= 90º and θ= 90º cases, and its incident angle is controlled by θ and φ as shown in the insets. c-d, Enhanced absorption cross-sectional area as a function of wavelength, where the absorption cross-sectional area (σ_{abs}) is normalised by the geometrical cross-section (σ_{geom}) for various widths (c) and thicknesses (d).

5.6 Comparison with the Broadband Background Thermal Emission

We now analyse the contribution of the background broadband thermal emission, which is suppressed because of the small thickness (100 nm). In bulk SiO_2, the strong broadband absorption prevents the observation of further enhanced emission by polaritonic resonance. Therefore, a highly transparent (less absorbing) ribbon could signify the role of SPhPs in suppressing the broadband background, whose ε was reduced to ~0.062 in the thin-film limit as shown in Fig. 5.4(a). This significantly quenched background broadband ε in the thin film provides the basis for dominantly coherent emission in the nanoribbon designs.

We now seek to understand the enhancement of the coherent emission in the nanoribbons, which was over 8.5 fold for the 6.28-µm-wide ribbon at 150 K compared with the thin-film limit calculated above. This enhancement is remarkable, considering that the spectral window for emission ($\omega_{TO} \sim 1251$ cm^{-1} to $\omega_{LO} \sim 1065$ cm^{-1} or from 8 to 9.5 µm) is now much narrower compared with the broad thermal spectrum. This enhancement can be understood from the strong resonant nature of the antenna-like nanoribbons, which results in an effective absorption cross-section (σ_{abs}) that is significantly higher than the geometrical one (σ_{geom}).[162] Fernández-Hurtado *et al*.[162] suggested theoretical guidelines to overcome the far-field limit by Planck's law and have systematically studied the far field radiation heat transfer from and between various sub-wavelength dielectric objects through the theoretical and numeric modelling. The computational study introduced the enhanced far-field thermal conductance between two anisotropic objects by increasing absorption efficiency, which was

subsequently verified experimentally by Thompson *et al.*[163] Similarly, we modelled σ_{abs} of the nanoribbons using a finite element method (FEM) approach in COMSOL.

Here, two plane waves propagating along the length with normal polarisation were simultaneously exposed to evaluate their averaged contribution, as shown in the inset in Fig. 5.4(c). The modelling results of σ_{abs}, as observed in Fig. 4c, indeed showed strong enhancement within the Reststrahlen band (Fig. 5.4(c)). The results are clearly distinguished from the lossy dielectric regime at around 12 μm wavelength. The peak enhancement factors ranged from 25 to 55 in ribbons of different widths. The enhancement increased when the ribbon width was reduced from 10 μm to 500 nm. From our results on the dispersion relations of SPhPs in a 100-nm-thick SiO_2 (Fig. 5.1(c)), the wavelengths of the SPhPs $(2\pi/q)$ ranged from 0.8 to 1.8 μm at around 9 μm. Therefore, the ribbons with widths down to 500 nm, which is larger than half of the shortest SPhP wavelength, can still support localised resonance SPhP modes.

Our modelling results also indicate that further reduction of the ribbon width below 500 nm would rather lead to smaller enhancement. For example, the peak enhancement factor for 100 nm width is 45, which is smaller than that of the 500 nm width (~55), see Fig. 5.4(c). This difference occurs because when the width is reduced to less than half the wavelength of certain modes of SPhPs, the localized resonance mode can no longer be supported within the width of the ribbons. Therefore, as the width decreases, a greater portion of the localised SPhP modes become unavailable. This result highlights the importance of the anisotropic nanoribbon design with suitable widths in maximising the resonance effect and resultant coherent thermal emission, as an isotropic cross section such as that in a cylindrical rod would

be unable to support certain resonance modes and consequently lead to a much smaller emissivity (e.g., $\varepsilon = 0.025$ in a 100-nm-diameter nanorod[165]). The geometry-dependent peak shift in the metallic regime indicates the coherent effect, as opposed to the monotonic change in the dielectric regime (near 12 μm wavelength).

We also modelled the enhanced σ_{abs} with different thickness. The thicker ribbon would result in the less overlaps of two evanescent waves at the top and bottom surfaces. Therefore, it yields smaller enhancement as shown in Fig. 5.4(d). The enhanced σ_{abs} is closely correlated with the enhancement of the measured ε. Therefore, we can attribute the largely enhanced ε from the nanoribbons to the coherent emission within the Reststrahlen band caused by the strong SPhP resonance.

Similar to the analytical model using a thin film, we also conducted mode analysis study of nanoribbons with the finite width and thickness. We compared the propagating vector of the thin film to that of nanoribbons calculated using COMSOL. The ribbon structure assumes infinite length and the k_p is parallel to the length. The two finite dimensions in thickness and width resulted in multiple modes, as shown in Fig. 5.5. The dominant modes with high q are very close to the dispersion of the thin film. Therefore, similar to the analysis from the thin film, it can be concluded that symmetric configurations of electric fields at the surfaces dominantly support the energy confinement. In addition, we observed the electric field intensity distributions at the cross-section of nanoribbons. Indeed, it showed high intensity along the width. The lowest order of modes, marked with the red circle, are well overlapped with the fundamental mode available from the dispersion relation of a thin film. For higher order modes, we could clearly observe the coherent resonance along the width

(Fig. 5.5(b)). Please note that still the propagating direction is along the length, and the diverse forms of polarization increase the number of modes. Although the higher order modes have lower q values, still multiple modes possess significantly higher q, compared to the light line. Further, the shift in q is smaller with the narrower width (Fig. 5.5(b)). Corresponding to the real part (q) of propagating vector ($k_p = q + i\kappa$), we also studied the imaginary counterpart (κ). The propagating length was then calculated by $1/2\kappa$, shown in Fig. 5.5(c). Broad range of propagating length from 100s nm to ~1 mm, can be supported. It implies that the anisotropic structure could have the length-dependent emissivity. In our experiments (Figs 3.3(e)-(f)), the fitted lines assume a constant ε over all the lengths up to 600 µm. The error range covers the potential length-dependent behaviour. All modelling in this study has been done with an infinite length, but more rigorous theoretical study, such as fluctuational electrodynamics[162] could be a potential interesting study for the non-traditional far-field radiation.
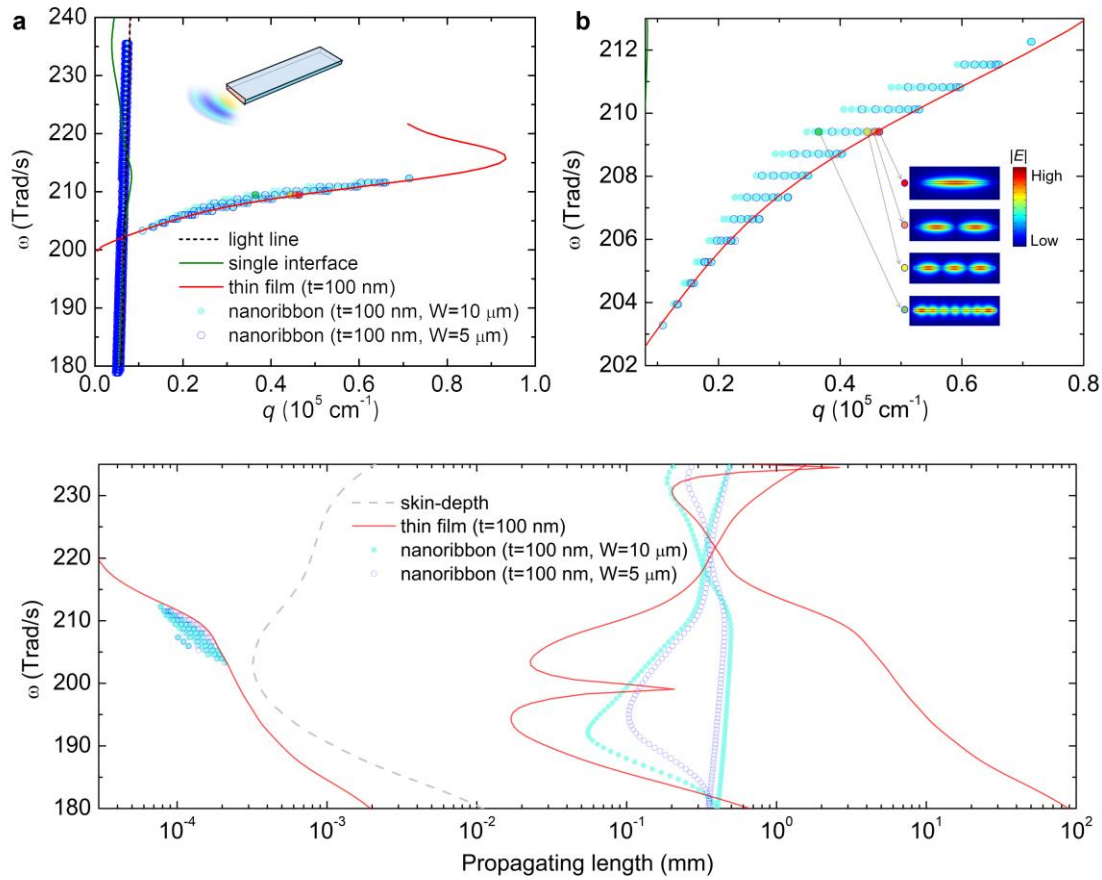
Figure 5.5   Numerical mode analysis of nanoribbons. a, Dispersions of nanoribbons by numerical modelling. The numerical results (symbols) were compared to the analytical results of light line, single interface and a thin film. b, Zoomed-in plots of a. The insets represent the electric field intensity distributions in the cross-section of a 5-µm wide nanoribbon at the four colour-filled symbols. c, Propagating lengths of nanoribbons with 5 and 10 µm widths, corresponding to the dispersion in a-b.

In addition to the cross-sectional size-dependent emission, we modelled and compared the directional emissivity (ε_{dir}) of a nanoribbon and a film at 9.5-µm wavelength (e.g., ω_{LO} with the TE-polarised mode) using the finite-difference time-domain (FDTD) method, as shown in Fig. 5.4(c). Compared with ε_{dir} of the thin film (e.g., $\varepsilon_{dir}<1$ in all

directions), ε_{dir} of the nanoribbon with 5-μm width was distinguishably enhanced with the larger incident angle θ with fixed $\varphi=90°$ (see the θ and φ definition in the insets of Fig. 5.4(c)). The edges of the nanoribbon exposed to the incoming waves enhance the coupling of SPhPs, leading to the efficient emissive behaviour by the resonant modes. Similarly, as this nanoribbon is a 3D anisotropic structure, we also controlled φ (Fig. 5.4(c)) and observed further enhancement when the incident wave was close to parallel to the length. The higher absorption originates from the infinite length of the nanoribbon used in the model. These findings clearly demonstrate the merit of the anisotropic designs to selectively emphasise the coherent modes. Our observation for the enhanced emissivity over the thin film limit originates from the fact that the selective enhancement (in the spatial and spectral domains) outweighs the reduced absorption by the smaller volume, compared to the skin-depth (determined by $\lambda/4\pi k$, where k is the imaginary part of the complex refractive index). This point is different from the previous study by Thompson *et al.*[163] As we observed from the angle-dependent absorption-cross section, the most significant enhancement occurred along the edge with sharper angles. It implies the strong directionality. Here we want to clarify that the observed enhancement does not mean the super-Planckian emission. The spectral enhancement we observed from the modeling is up to 55, but it is within a certain spectral and directional range and thus is still insufficient to result in a super-Planckian hemispherical emissivity, which is an integrated effect over the entire spectral and angular ranges. This was also clearly shown by Fernández-Hurtado *et al.*.[162] Nevertheless, the fact that the emissivity is higher than the thin film limit underscores the prominent effect of the localized modes.

Our sensitive thermometry platform also enables the direct emissivity measurement at lower temperature, where the coherent effect is expected to be stronger but the emissive power is more challenging to measure (radiative power scales as T^4). At lower temperature, the phonon lifetime is expected to be longer and the $k_B T$ broadening is expected to be smaller, which will lead to a higher Q factor of the emission. For the modelled emission from thin films, the spectral emittance showed a peak within the Reststrahlen band, whereas significantly suppressed emission was observed in the broad range. The modelling results assumed a temperature-independent optical parameter. Therefore, the temperature-dependent behaviour was only determined by the peak shift in the Planck's distribution and showed a maximal value near room temperature, corresponding to a thermal wavelength of ~10 μm (inset in Fig. 5.6(a)). For the nanoribbons, however, we observed higher ε at lower temperature, up to 0.35 at 150 K for the 6.28-μm-wide ribbon (Fig. 5.6(a)). This unusual temperature dependence can be explained by the smaller $k_B T$, which increases the Q factor because of the smaller loss (lower ε'') at lower temperature. The damping term in the dielectric function in the form of the Lorentzian function is correlated with the lifetime of the optical phonons, which is smaller at lower temperature [174,182] and leads to less broadening of the emission peak and stronger coherent emission; thus, the emissive behaviour would be temperature dependent. To quantify the coherent emission, we introduce a coherent enhancement factor (CEF) determined by the ratio of ε_{ribbon} to ε_{film}, where ε_{ribbon} and ε_{film} are ε of a nanoribbon and film of identical thickness, respectively. As shown in Fig. 5.6(b), the higher CEF observed at lower temperature is a very clear signature of the coherent

mechanism.[183-185]. The maximum CEF achieved here was 8.5 for the 6.28-µm-wide ribbon at 150 K.
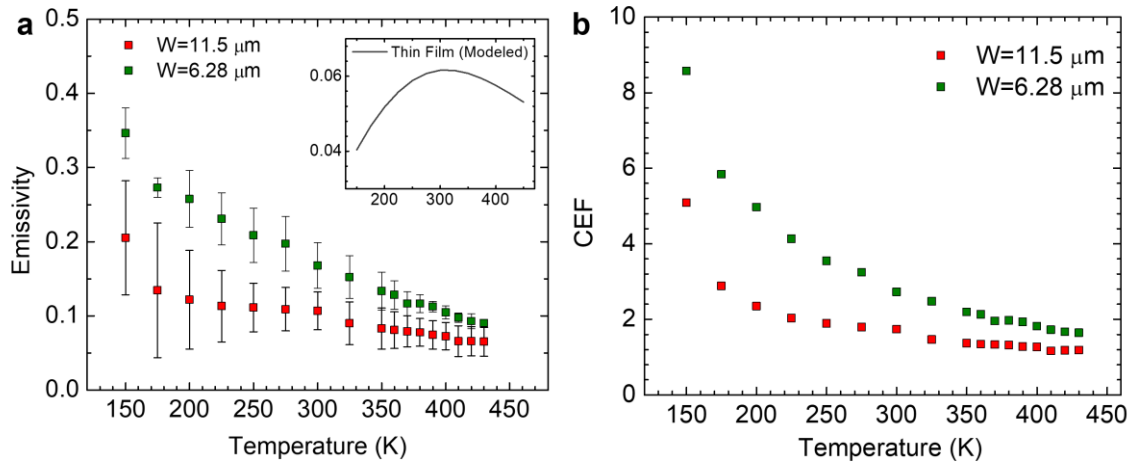
Figure 5.6   Temperature-dependent emissive behaviour. a, Plots of emissivity as a function of temperature, where the error bars correspond to the uncertainty in the fitting as shown in Figs. 5.3(e)-(f). The inset shows the modelled emissivity of an infinite thin film. b, Plots of coherent enhancement factor (CER) as a function of temperature.

We analyzed the temperature-dependent emissive behavior. Based on the Planck's distribution, we can expect the heat transfer coefficient, h, is proportional to T^3, and some previous experimental studies have shown the possibility to have different temperature-dependency[157,166] but no specific study has been conducted to reveal the reason behind it. Figure 5.5(a) shows indeed different temperature dependency of emissivity between the experimental and the modeling results. The modeling results assumed temperature-independent optical parameter. Therefore, the temperature-dependent behavior is only determined by the peak shift in the Planck's distribution function, and it shows the maximal

value at around room temperature corresponding to the thermal wavelength of ~10 µm. We observed nonlinear slope of $\ln(h)$ as a function of $\ln(T)$, over the broad range of temperature (Fig. 5.7). It implies that the temperature dependency obeys Plank's law by modifying the dielectric constants.
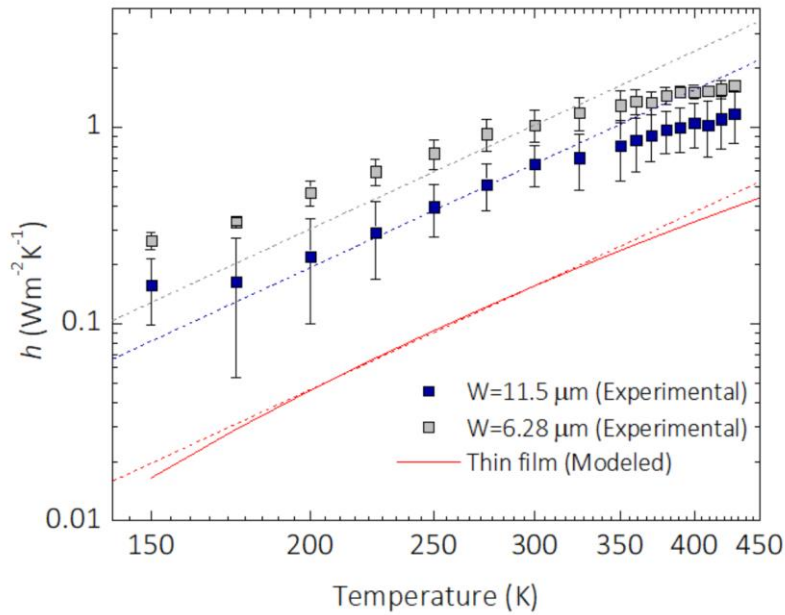
Figure 5.7   Plots of heat transfer coefficient as a function of temperature in log scale. The dashed lines are expected linear h based on the emissivity at 300 K. Error bars corresponds to the uncertainty in the fitting in Fig. 5.6(a).

5.7 Methods

5.7.1 Preparation and Thermal Conductivity Measurement of SiO_2 Nanoribbons

To eliminate the potential impact of thermal contact resistance, the nanostructures were monolithically integrated with the thermal reservoirs. First, we prepared a 100-nm thermal oxide film on a Si wafer. Electrodes were patterned on top of the SiO_2 layer using photolithography, and a metal layer (Ti/Pt 80 nm) was deposited by sputtering. After defining the patterned area with Cr based on the designed nanoribbon structures, the SiO_2 layer was dry etched using CHF_3 and Ar gas (Oxford Plasmalab P80). Then, an additional Cr layer was deposited for protection with a larger area than that of the nanoribbons before the subsequent Si deep reactive ion etching (DRIE) by SF_6 gas (Oxford Plasmalab P100 RIE/ICP). This etching step provided a larger distance (~50 µm) between the Si substrate and SiO_2 nanoribbons. After the DRIE, the Cr layers were removed with a Cr etchant, and the Si was treated with a buffer oxide etchant (BOE), followed by XeF_2 etching to suspend the nanoribbons by removing the Si substrate underneath.

5.7.2 Fin Model
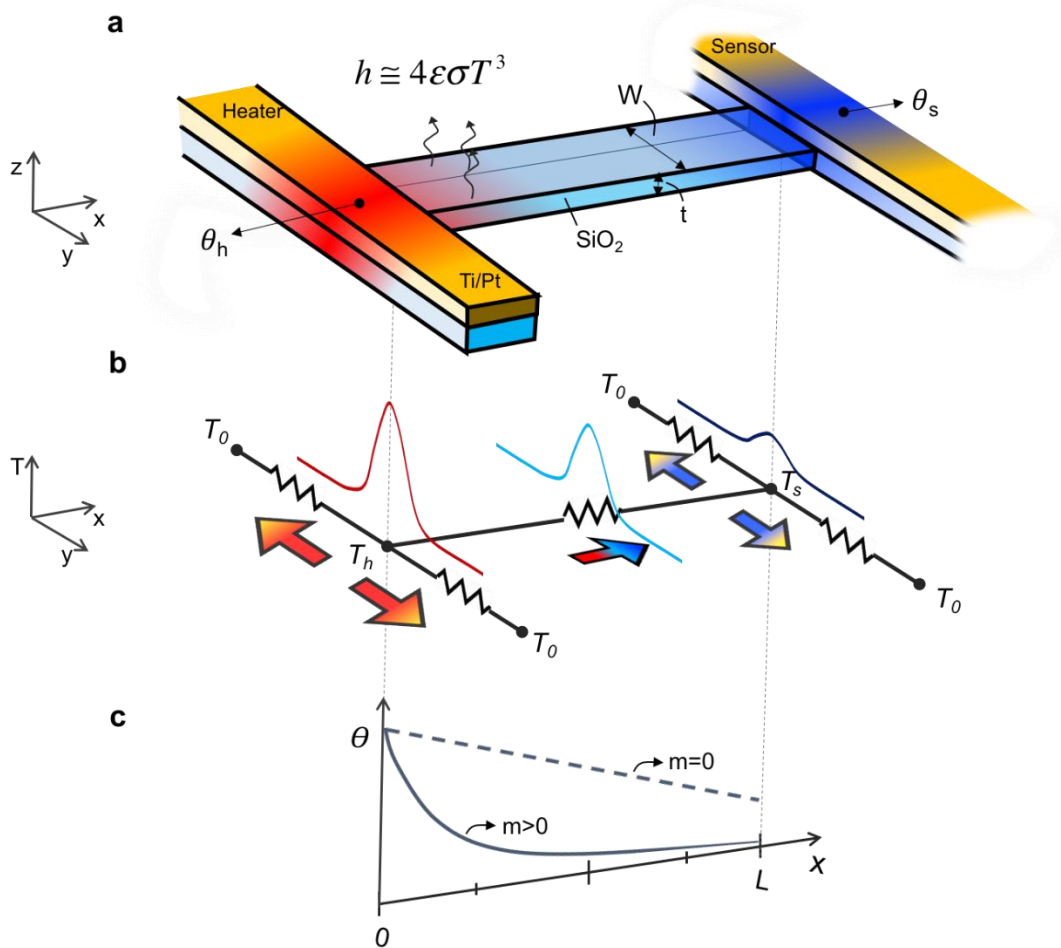
Figure 5.8   (a) Schematic of a SiO$_2$ ribbon with radiative heat loss ($m > 0$), where θ is a temperature rise. (b) Schematics of temperature profiles along the metal beams (e.g. heater and sensor) and the nanoribbon. (c) Temperature rise along the nanoribbon with and without radiative heat loss are compared (e.g. m>0 and m=0, respectively).

A fin has high aspect ratios in dimensions to extend the surface area. Therefore, the temperature change along the length has the major contribution while it can be assumed that the temperature across the smaller dimension is constant. For this reason, the fin structure

can possess the limited heat conduction and more effectively radiate heat, thus it has been widely used to cool devices as a heat sink[186].

The temperature profile can be described in Fig. 5.8. By defining the temperature profile along the x-axis, parallel to the length, above the ambient temperature (θ) as below.

$$q = C_1 \cosh(mx) + C_2 \sinh(mx) \tag{5.7}$$

, where C_1 and C_2 are unknown constants.

$$\theta = T - T_0 \tag{5.8}$$

The general solution introduces the feature of exponential temperature drop while propagating along the x-axis. The decaying rate is weighted by m, so-called fin parameter, and it is determined by:

$$m = \sqrt{\frac{hP}{\kappa A_c}} \tag{5.9}$$

$$h \approx 4\varepsilon\sigma T^3 \tag{5.10}$$

where h is the heat transfer coefficient, ε is the emissivity, σ is the Stefan–Boltzmann constant, and T is the temperature. Quantifying the m parameter enables to obtain the ε.

To specify the unknown parameters from the solution for θ, here we summarize the boundary conditions for temperatures at $x = 0$ and $x = L$:

$$\theta\big|_{x=0} = C_1 = \theta_h \tag{5.11}$$

$$\theta\big|_{x=L} = \theta_h \cosh(mL) + C_2 \sinh(mL) = \theta_s \tag{5.12}$$

$$C_1 = \theta_h \tag{5.13}$$

$$C_2 = \frac{\theta_s - \theta_h \cosh(mL)}{\sinh(mL)} \tag{5.14}$$

where θ_h and θ_s are the temperature rise at the ends of the fin. By integrating two ends to the suspended metal beams, θ_h and θ_s are measured in this thermometry platform. Therefore, θ can be represented as:

$$\theta = \theta_h \cosh(mx) + \frac{\theta_s - \theta_h \cosh(mL)}{\sinh(mL)} \sinh(mx) .$$ (5.15)

Next, we summarize the boundary conditions for heat flux at $x = 0$ and $x = L$.

For heat flux at $x = 0$ (heating side),

$$Q_h = -\kappa A_c \left. \frac{\partial \theta}{\partial x} \right|_{x=0} = -\kappa A_c m C_2 .$$ (5.16)

For heat flux at $x = L$ (sensing side),

$$Q_s = -\kappa A_c \left. \frac{\partial \theta}{\partial x} \right|_{x=L} = -\kappa A_c \left\{ m C_1 \sinh(mL) + m C_2 \cosh(mL) \right\} .$$ (5.17)

To meet the overall energy balance,

$$Q_s = G_b \theta_s$$ (5.18)

$$-\kappa A_c \left\{ m C_1 \sinh(mL) + m C_2 \cosh(mL) \right\} = G_b \theta_s$$ (5.19)

$$-\kappa A_c m \left(\theta_h \sinh(mL) + \frac{\theta_s - \theta_h \cosh(mL)}{\sinh(mL)} \cosh(mL) \right) = G_b \theta_s$$ (5.20)

$$\theta_h \sinh^2(mL) - \theta_h \cosh^2(mL) + \theta_s \left\{ \cosh(mL) + \frac{G_b}{\kappa A_c m} \sinh(mL) \right\} = 0$$ (5.21)

$$-\theta_h + \theta_s \left\{ \cosh(mL) + \frac{G_b}{\kappa A_c m} \sinh(mL) \right\} = 0$$ (5.22)

$$\theta_s = \frac{\theta_h}{\cosh(mL) + \frac{G_b}{\kappa A_c m} \sinh(mL)}$$ (5.23)

$$\left.\frac{\theta_s}{\theta_h}\right|_{m>0} = \frac{1}{\cosh(mL) + \dfrac{G_b}{\kappa A_c m}\sinh(mL)} \equiv \gamma .\qquad(5.24)$$

As shown in Fig. 5.8(c), the temperature profile become linear in the absence of heat loss ($h=0$, and eventually $m=0$).

$$Q_s = \frac{Q_h}{1+\dfrac{G_b}{\kappa A_c}L} = \frac{Q_h}{1+\dfrac{G_b}{G_s}} = \frac{G_s}{G_s+G_b}\theta_h \qquad(5.25)$$

$$G_s(\theta_h - \theta_s) = G_b\theta_s \qquad(5.26)$$

$$\theta_s = \frac{G_s\theta_h}{G_b + G_s} \qquad(5.27)$$

$$\left.\frac{\theta_s}{\theta_h}\right|_{m=0} = \frac{G_s}{G_b + G_s} \cong \frac{G_s}{G_b} \equiv \gamma_{\text{lossless}} . \qquad(5.28)$$

Finally, we can define the ratio factor, Δ as:

$$\Delta \equiv \frac{\gamma}{\gamma_{\text{lossless}}} = \frac{G_a}{G_s} \equiv \frac{\kappa_a}{\kappa_s} . \qquad(5.29)$$

where G_a is the measured apparent thermal conductance. By comparing the expected ratios of γ to the ratios of the measured conductivity, ε can be extracted.

We also conducted additional experiments with thick SiO_2 samples where the thickness is larger than the skin-depth, so the thermal radiation would follow the incoherent (broadband) bulk-like emission spectrum. As a result, we would expect the extracted emissivity value to be close to the bulk value of SiO_2 (~0.9 at room temperature). In our new experiments, we extracted the emissivity using the fin model, by following the same procedure as we did for the thin nanoribbons.

We designed the thick SiO_2 beams with 10 µm thickness, i.e., comparable with the skin depth of infrared from 8-10 µm in bulk SiO_2. To determine the suitable beam length to emphasize the radiative heat loss, we estimated the thermal conductance by conduction and radiation with an assumed emissivity of 0.9.
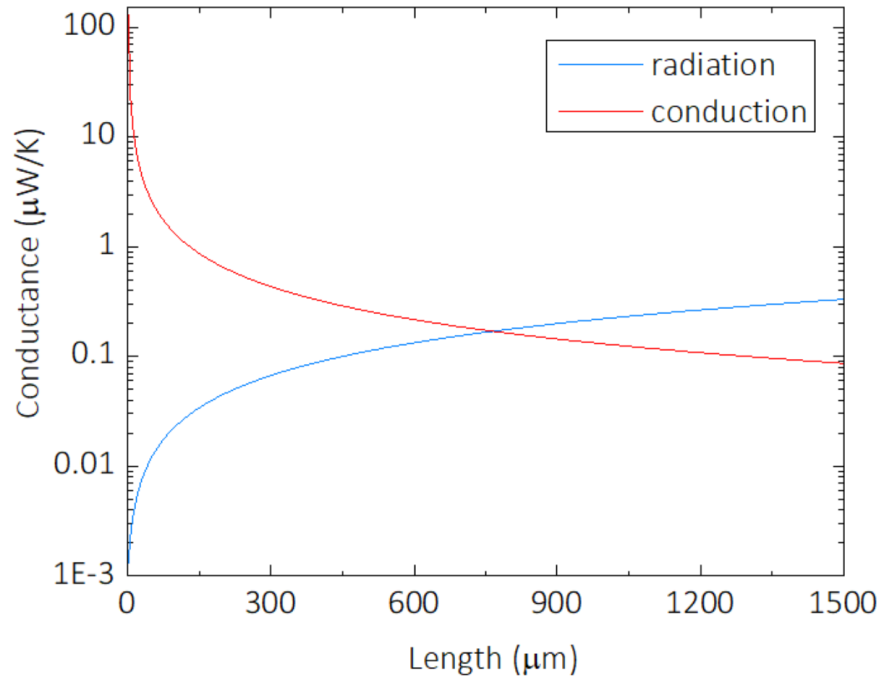
Figure 5.9   Plots of calculated thermal conduction due to phonon conduction and radiation heat loss as a function of the beam length for beam width of 7.5 µm and thickness of 10 µm.

Figure 5.9 shows that radiative conductance would be significant relative to heat conduction when the beam length is around 800 µm or longer. Thus, we fabricated the suspended SiO_2 beams with various lengths, ranging from 100 to 800 µm as shown in Fig. 5.10.

With various lengths, namely, 100, 400, 600 and 800 µm, we measured thermal conductivity as shown in 5.11. We analyzed temperature ratios between heating and sensing

sides, γ, at each length. At smallest length (100 μm), we obtained thermal conductivity of 1.41 W m^{-1} K^{-1} at room temperature. Again, at this length, the radiation is negligible (see Fig. 5.9) and the measured thermal conductivity agrees well with the expected bulk value of SiO$_2$. This again validates our heat transfer measurements. By using the thermal conductivity value of the shortest beam or the bulk SiO$_2$ (~1.4 W m^{-1} K^{-1}), Δ was calculated as shown in Fig. 5.11. Using the same fin model that fits all the sample lengths with a single fitting parameter (i.e., the emissivity), we found the best fit with an emissivity value of 0.77 ($\pm$0.07) for the 7.5 μm wide and 10 μm thick beams. This value agrees well with the theoretical expectation. For example, Golyk et $al.$ estimated around an emissivity of 0.7 for a cylindrical object with 5 μm radius.[165]
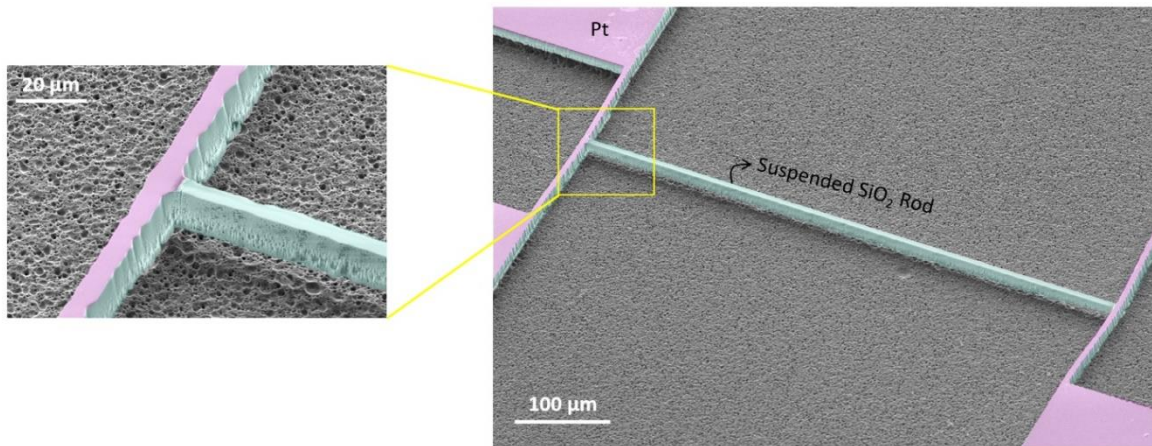
Figure 5.10   A SEM image of a suspended long SiO$_2$ beam with 10 μm thickness and 7.5 μm width.
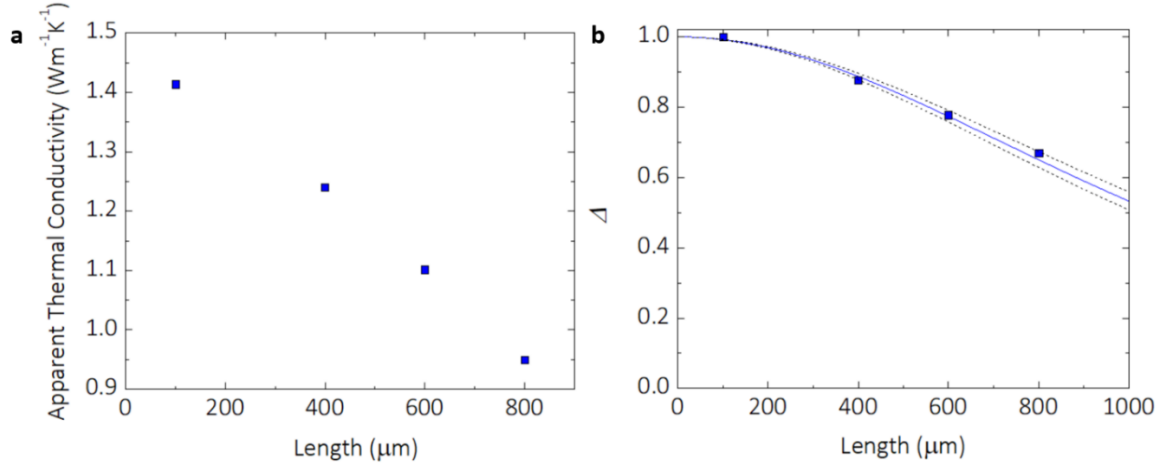
Figure 5.11   Plots of (a) apparent thermal conductivity at room temperature and (b) Δ with various lengths of samples, where the best fit emissivity is 0.77 and the fitting has a standard deviation of 0.07 in absolute emissivity.

5.7.3   Heat Transfer Measurements

Nanoscale emitters with radiative heat loss generate very small signals. Therefore, we employed an AC-modulated joule heating and lock-in thermometry technique, as depicted in Fig. 5.3(b), to improve the sensitivity. In addition, we used a Wheatstone bridge to measure the temperature at the sensing side with a high resolution down to ~0.25 pW K^{-1}.[179] By measuring the RMS of the voltages at the heating and sensing sides corresponding to the modulated heating with 1ω angular frequency (i.e., $V_{h,3\omega}$ and $V_{s,2\omega}$, respectively), the temperature rise could be determined[179]:

$$\theta_h = 3\frac{V_{h,3\omega}}{I_\omega}\left(\frac{dR_h}{dT}\right)^{-1} \tag{5.30}$$

$$\theta_s = \sqrt{2}\frac{V_{s,2\omega}(R_s + R_{s,p} + R_1 + R_2)}{I_{s,DC}R_2}\left(\frac{dR_s}{dT}\right)^{-1}. \tag{5.31}$$

116
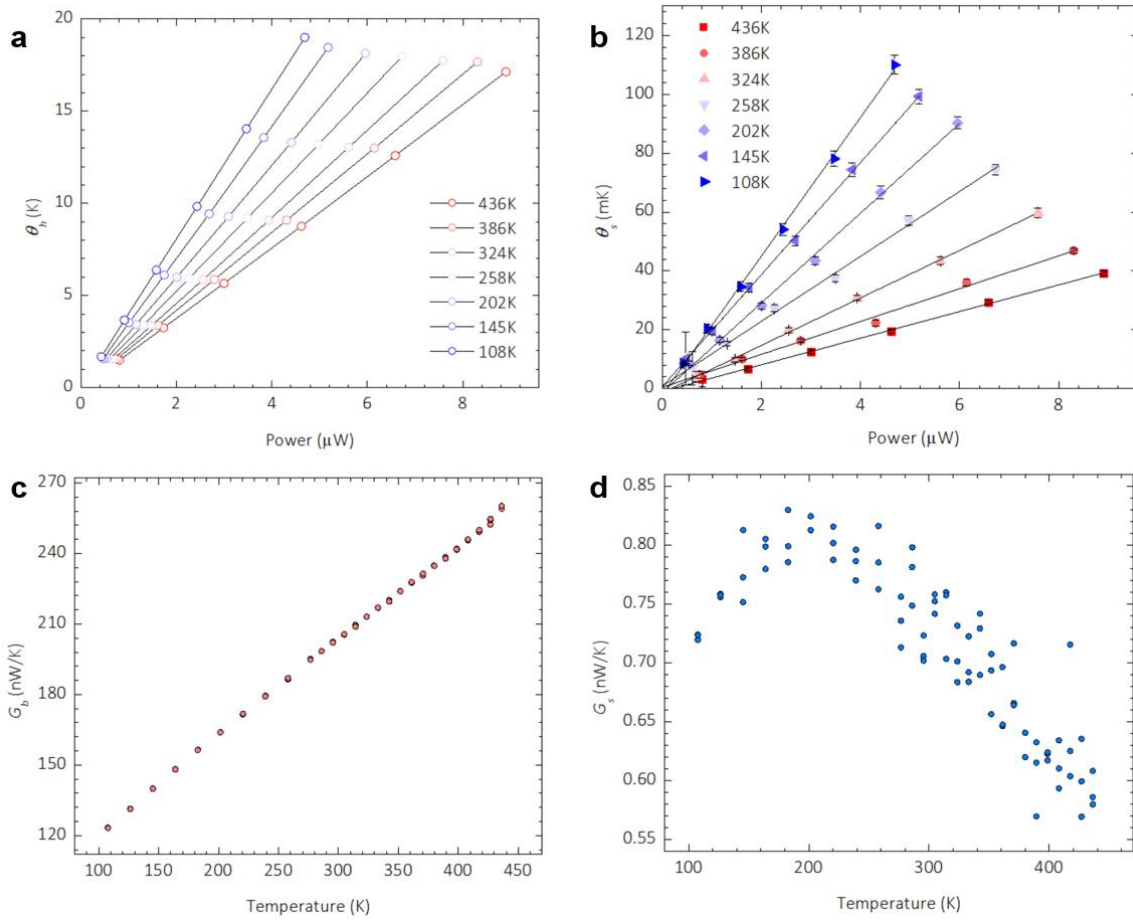
Figure 5.12 Plots of measured temperature rise at the heating (a) and sensing side (b) at different temperatures as a function of heating power, and thermal conductance of the heating (c) and sensing beam (d) as a function of temperature, for the nanoribbon with W=5 μm and L=600 μm.

Here, I_ω and $I_{s,DC}$ are the AC-modulated input current to heating and DC current to the sensing beam, respectively; R_h and R_s are the resistance of the heating and sensing beam, respectively; and $R_{s,p}$, R_1, and R_2 are the resistances of the Wheatstone bridge in Fig. 5.3(b). Equations (5.30–5.31) are applicable in the low-frequency regime, where the heat penetration depth is much longer than the length of the suspended bridge.[187] The measured temperature rise at the heating and sensing sides was inputted into equation (5.4) to obtain the parameter

γ. γ_{lossless} was determined from the short sample, which has negligible radiative loss compared with conduction by phonons. Finally, the experimentally measured Δ (= $\gamma/\gamma_{\text{lossless}}$) could be compared using equation (5.32) to extract the unknown parameter, m in the fin model, which allows both h and ε to be determined:

$$\Delta = \frac{\dfrac{1}{\cosh(mL) + \dfrac{G_{\text{b}}}{\kappa A_{\text{c}} m} \sinh(mL)}}{\dfrac{G_{\text{s}}}{G_{\text{b}} + G_{\text{s}}}}. \qquad (5.32)$$

As the measurements were done in vacuum ($\sim 10^{-6}$ Torr) and thus the convection and conduction of air is not important, h is only contributed by radiation heat loss, namely, only determined by the emissivity value. For each width, we used one single fitting parameter (ε) to fit all the ribbon lengths from 100 to 600 μm (Fig. 5.3(e) and 5.3(f)). We also showed that the measured thermal conductivity values of the shortest ribbons (50 μm long ribbon in Fig. 3c) agree well with the bulk value of amorphous SiO_2 (Fig. 5.14). At room temperature, the measured value is ~ 1.4 W m^{-1} K^{-1}. We note that at 50 μm length, the radiation heat loss is negligible compared to heat conduction along the ribbon, as the calculated Δ is very close to 1 even if the emissivity is 0.90 (see Fig. 5.15). The thermal conductivity of amorphous SiO_2 is well known and is not expected to be influenced by the size range studied here (down to ~100 nm thickness in this case) because of the short phonon MFP in SiO_2 (<10 nm), as well documented in the literatures[188,189]. We have also previously shown bulk-like thermal conductivity of SiO_2 nanostructures (nanowires and nanotubes) with thickness down to ~7 nm. Therefore, we obtained bulk-like thermal conductivity of the ribbons (directly from the shortest, 50 μm long ribbon, and indirectly from the fitting to all the other ribbons) over the

entire temperature range of 150 to 430 K. We also obtained bulk thermal conductivity value from short (100 μm) and thick (10 μm) SiO₂ beams (see Fig. 5.14). These results validate our heat conduction measurements. In particular, the use of the monolithic devices eliminates any potential thermal contact resistance between the ribbons and the thermal reservoirs, which have been a challenging issue in many nanowire thermal transport measurements using similar platforms.
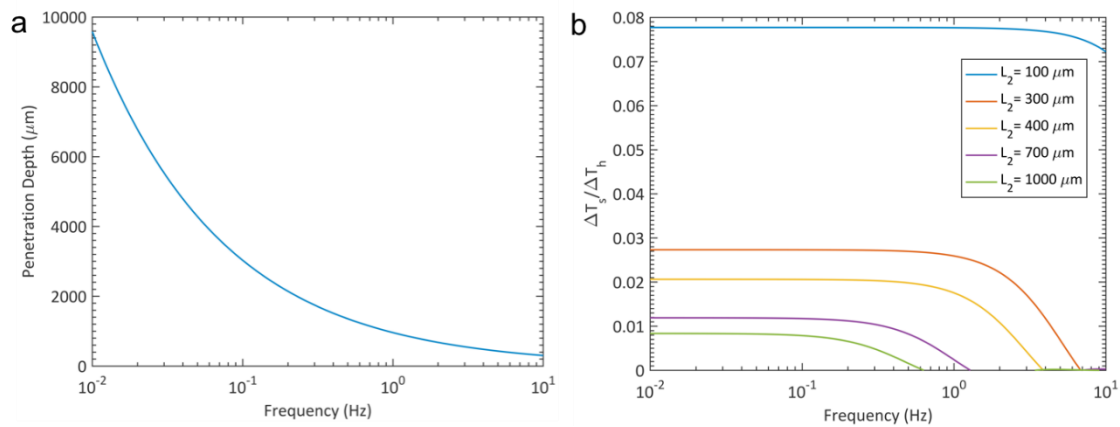
Figure 5.13   Plots of penetration depth (a) and $\Delta T_s / \Delta T_h$ (b) as a function of frequency.
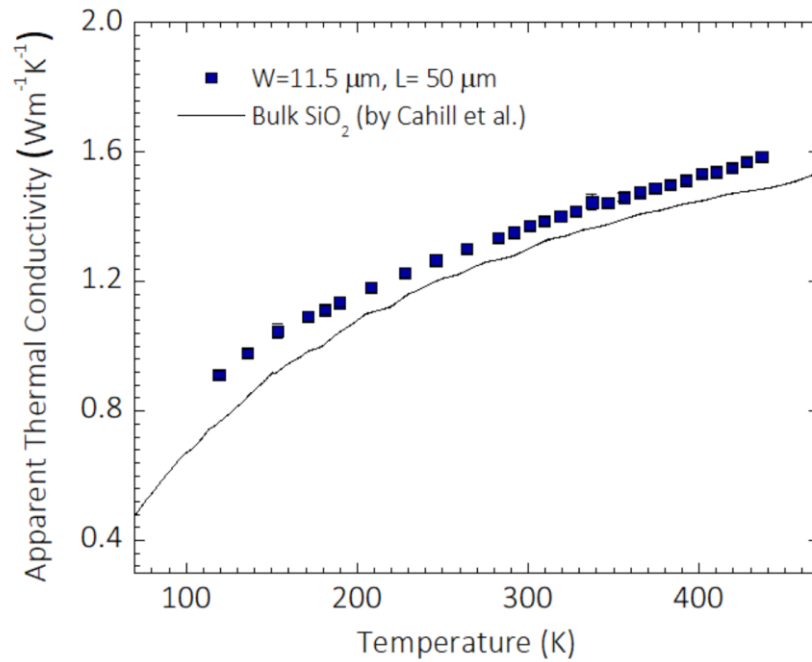
Figure 5.14   Measured thermal conductivity of a nanoribbon (W=11.5 µm, L= 50 µm and t=100 nm) were compared to the bulk SiO_2 thermal conductivity[190].
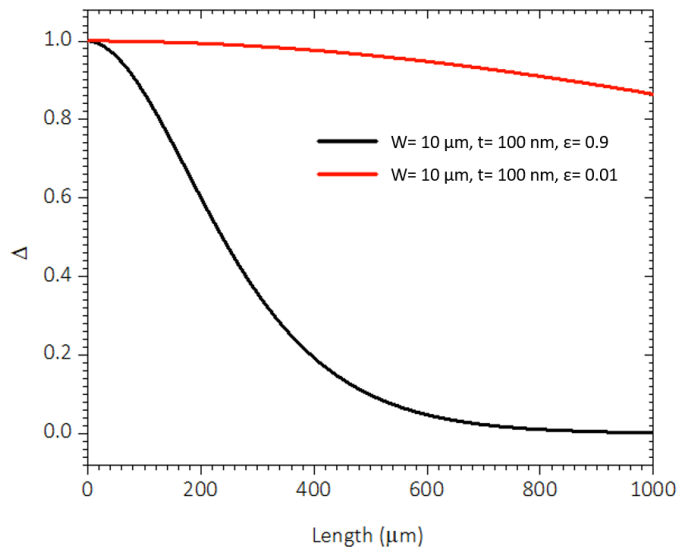
Figure 5.15   Plots of the modeled temperature rising ratio, Δ with various lengths at room temperature.

5.7.4　Directional Emissivity Modeling

The emissivity of an infinite ribbon was estimated from the absorption cross section, which was calculated numerically using FDTD simulation (Fig. 5.16). The ribbon was illuminated by a plane wave (emitted by a total-field scattered-field source[191]), the profile of which in the frequency domain forms a Gaussian pulse, covering the frequency range in which SiO_2 has an appreciable extinction coefficient (55–280 Trad s^{-1}).
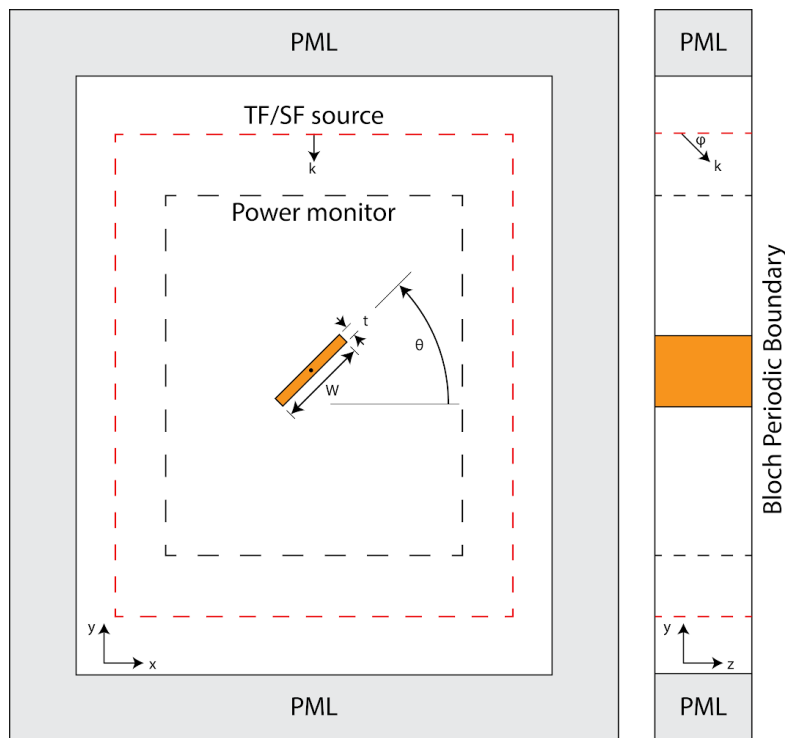
Figure 5.16　Finite-difference time-domain simulation layout.

The incidence angle was manipulated to cover a hemisphere by changing the ribbon orientation angle, θ, from 0° to 180° and the plane-wave travel direction, ϕ, from 0° to 90° (see Fig. 5.16). Because of the infinite length of the ribbon, we could accommodate the out-

of-plane travel direction of the incident waves by applying Bloch periodic boundary conditions on the solution domain sides perpendicular to the direction along the length[191]. For incidence waves with $\phi \neq 90°$, we limited the frequency spectrum of the Gaussian plane wave, such that the deviation in the angle ϕ was below 5° for waves with different frequencies. The power absorbed by the ribbon was calculated by monitoring the net power flux crossing the boundary surrounding the ribbon in the time domain and then performing a Fourier transform to recover the absorbed power in the frequency domain. The spectral absorption cross-section was then calculated as the ratio between the absorbed spectral power and the plane-wave spectral source intensity. According to Kirchoff's law, the directional and spectral emissivity, ε_{dir}, has the same value as the spectral absorption efficiency, which can be calculated from the ratio between the absorption cross-section, σ_{abs}, and ribbon projected area, σ_{geom} (assuming a ribbon of unit length)[192]:

$$\varepsilon_{dir}(\omega,\theta,\phi) = \frac{\sigma_{abs}(\omega,\theta,\phi)}{\sigma_{geom}(\theta,\phi)} \tag{5.33}$$

$$\sigma_{geom}(\theta,\phi) = (W\cos\theta + t\sin\theta)\sin\phi \,. \tag{5.34}$$

Table 5.1   Summary of resonant frequencies for SiO$_2$.[175]

Resonance	$\omega_{LO,\,1}$	$\omega_{TO,\,1}$	$\omega_{LO,\,2}$	$\omega_{TO,\,2}$
frequency [$\times 10^{14}$ rad/s]	0.8	0.9	2.0	2.3
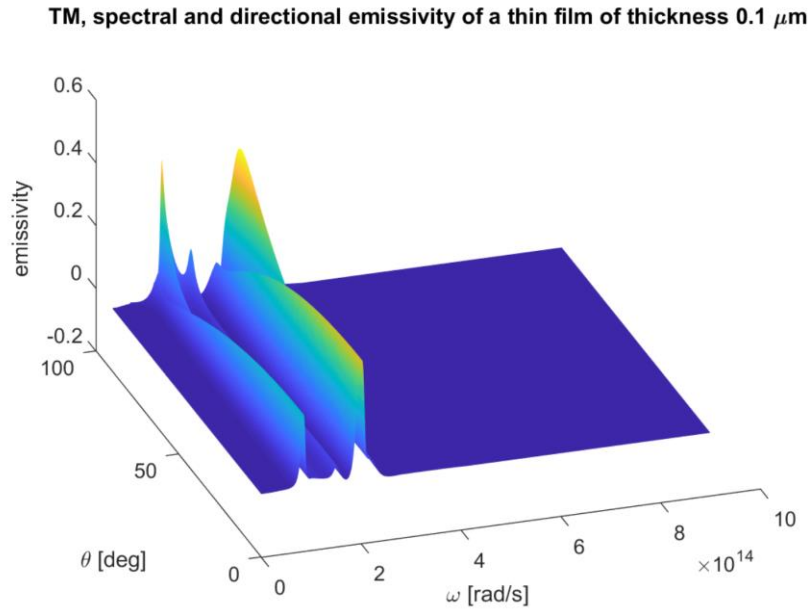
Figure 5.17   Plots of spectral and directional emissivity of TM mode of a 100 nm thin film.
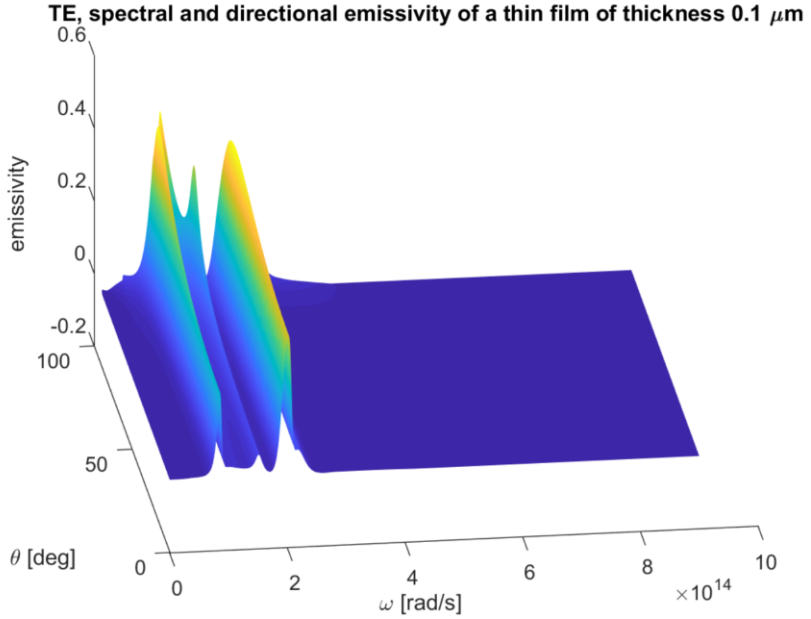
Figure 5.18   of spectral and directional emissivity of TE mode of a 100 nm thin film.
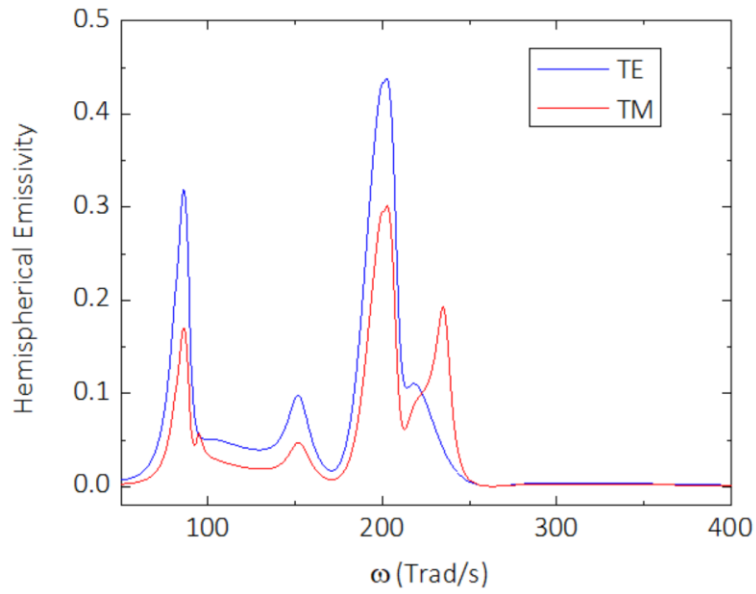
Figure 5.19   Plots of hemispherical emissivity of TE and TM mode of a 100 nm thin film.
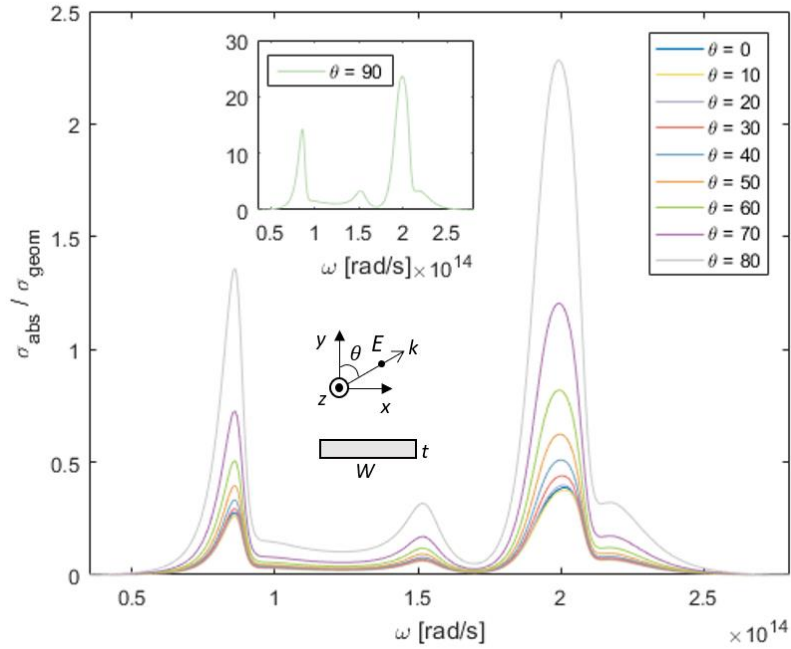
Figure 5.20   Plots of spectral absorption efficiency of nanoribbon (W = 5 µm) with various incident angles, where the polarized electric fields are on the planes including the length.
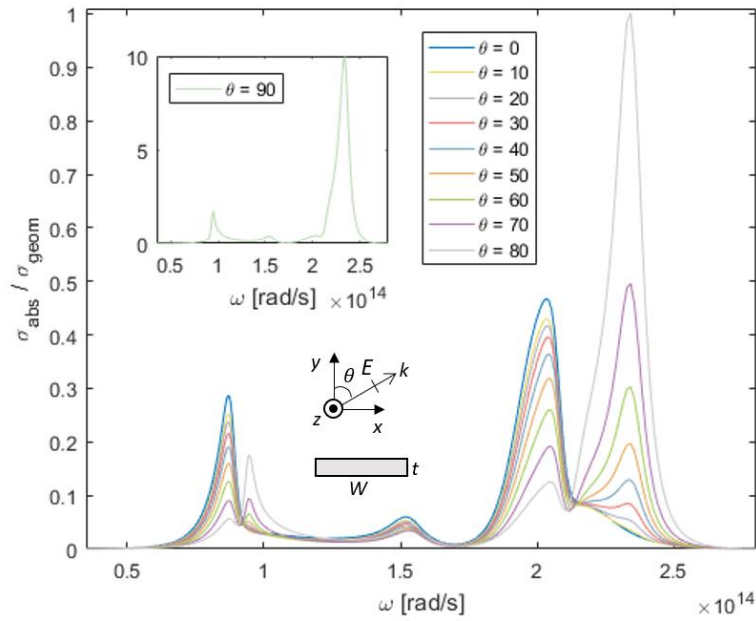
Fiture 5.21   Plots of spectral absorption efficiency of nanoribbon (W = 5 µm) with various incident angles, where the polarized electric fields are on the plane normal to the length.
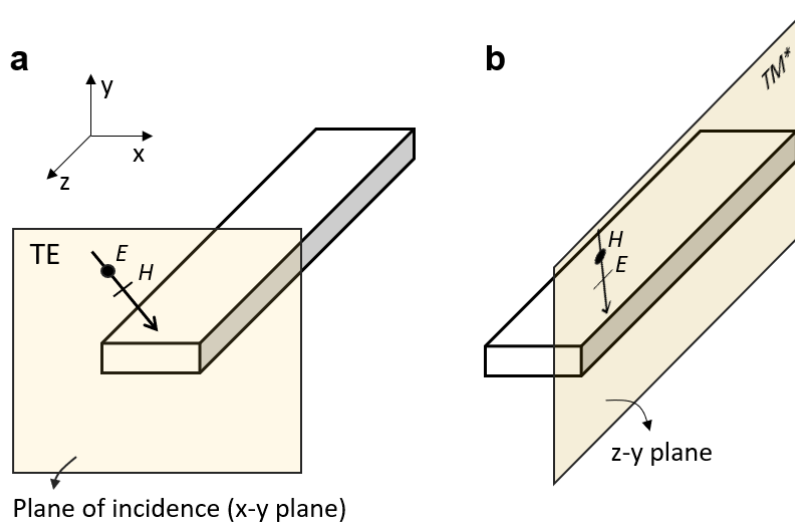
Figure 5.22   Relative polarization modes at different facets.

Our modeling was done with the fixed incident TE or TM polarized wave while rotating the ribbons by different angles. Unlike the infinite film which has only one finite dimension in thickness, the nanoribbon structures have two finite dimensions in both width and thickness. Therefore, although we have an incident wave with the TE or TM polarization for one specific facet, the other perpendicular planes will meet a different polarization, relatively defined by φ and θ.

For instance, here we draw an explicit case where it showed the opposite polarizations with the rotated structures. Figure 5.22(a) shows incident TE wave on the x-y plane, which is normal to the length. On the plane of incidence, the TE wave does not have an electric field component which is polarized normal to the surface (width or thickness) on x-y plane. On the other hand, as the nanoribbons are 3D structures, we can move our view point to one of perpendicular planes to see how different faces are affected by the TE incident on x-y plane. Figure 5.22(b) shows the example on the z-y plane. In this normal plane to x-y plane, there is an electric field component polarizing across the surface. Therefore, one incident wave can excite both TE and TM modes in the 3D structures.

5.7.5 Dispersion Relation
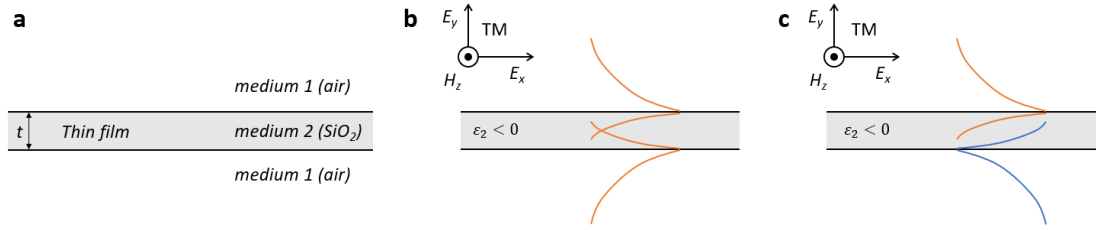
Figure 5.23 Schematics of (a) a thin film structure consisting of a medium 2 (SiO₂) surrounded by medium 1 (air), and (b) symmetric and (c) asymmetric configurations of TM polarized surface waves.

Electromagnetic interactions between two adjunct surfaces can be significant with the poles of the reflective coefficient, r, determined by the Fresnel equation,

$$r_{TM} = \frac{\varepsilon_2 k_{t,1} - \varepsilon_1 k_{t,2}}{\varepsilon_2 k_{t,1} + \varepsilon_1 k_{t,2}} \qquad (5.35)$$

where ε_i is the complex permittivity, $k_{t,i}$ is the transverse vector ($k_{t,i}^2 + k_p^2 = \varepsilon_i k_0^2$) in the medium i, k_p is the propagating vector along the surface ($k_p = q + i\kappa$), where q and κ are the real and imaginary part of the momentum vector, respectively), and k_0 is the free space vector. To figure out the fundamental modes with two surfaces, we solve

$$1 - r^2 e^{2ik_{t,2}t} = 0. \qquad (5.36)$$

The above equation yields solutions for the poles of the complex reflectivity. TM polarization can support surface phonon polaritons when the real part of permittivity is negative. The analytical solutions for the above equations can be achieved by considering two different

configurations of surface waves at each one of the two interfaces. For the symmetric electric field configuration of TM polarization as shown in Fig. 5.23(b),

$$r_{\mathrm{TM}} = e^{ik_{t,2}t} = \frac{\varepsilon_2 k_{t,1} - \varepsilon_1 k_{t,2}}{\varepsilon_2 k_{t,1} + \varepsilon_1 k_{t,2}} \tag{5.37}$$

$$\left(\varepsilon_2 k_{t,1} + \varepsilon_1 k_{t,2}\right) e^{ik_{t,2}t} = \varepsilon_2 k_{t,1} - \varepsilon_1 k_{t,2} \tag{5.38}$$

$$\varepsilon_2 k_{t,1}\left(1 - e^{ik_{t,2}t}\right) = \varepsilon_1 k_{t,2}\left(1 + e^{ik_{t,2}t}\right) \tag{5.39}$$

$$\frac{\varepsilon_2}{\varepsilon_1} = -\frac{k_{t,2}}{k_{t,1}}\coth\left(\frac{t}{2i}k_{t,2}\right). \tag{5.40}$$

In the thin film regime ($k_{t,2}t \ll 2$), the equation can be simplified in the form of:

$$\frac{\varepsilon_2}{\varepsilon_1} = -\frac{2i}{t}\frac{1}{k_{t,1}}. \tag{5.41}$$

where $k_{t,1}$ is positive. In the case where the highly confined guided modes ($k_{t,i} = \sqrt{\varepsilon_i k_0^2 - k_p^2} \approx ik_p$) are supported, the further simplified form follows:

$$k_p = -\frac{2}{t}\frac{\varepsilon_1}{\varepsilon_2}. \tag{5.42}$$

Note that this algebraically simplified equation only counts the zeroth order mode. With the consideration of the Fabry-Perot resonance, the equation can be shown as[176]:

$$k_p = q(\omega) + i\kappa(\omega) = \frac{i}{t}\left[2\arctan\left(i\frac{\varepsilon_1}{\varepsilon_2}\right) + \pi l\right] \tag{5.43}$$

where l is an integer for the higher order modes, and the dispersion curves of fundamental modes were shown in Fig. 5.24 with l=0.

Similarly, for the asymmetric electric field configuration for TM polarization as shown in Fig. 5.23(c),

$$r_{\text{TM}} = -e^{ik_{t,2}t} = -\frac{\varepsilon_2 k_{t,1} - \varepsilon_1 k_{t,2}}{\varepsilon_2 k_{t,1} + \varepsilon_1 k_{t,2}} \tag{5.44}$$

$$\frac{\varepsilon_2}{\varepsilon_1} = -\frac{k_{t,2}}{k_{t,1}} \tanh\left(\frac{t}{2i} k_{t,2}\right). \tag{5.45}$$

In the thin film regime ($k_{t,2}t \ll 2$), the aforementioned equation can be simplified in the forms of:

$$\frac{\varepsilon_2}{\varepsilon_1} = -\frac{t}{2i} \frac{k_{t,2}^2}{k_{t,1}} \tag{5.46}$$

where $k_{t,1}$ is positive.

By comparing the simplified equations from symmetric and asymmetric dispersions, it is clear that two distinct fundamental modes have opposite thickness-dependent behaviors. While the symmetric mode possesses more bounded modes as the film thickness decreases, the asymmetric mode becomes closer to the light line with decreasing film thickness, as shown in Figs. 5.24(a)-(b). The thickness-dependent behaviors are clearly shown in the Reststrahlen band ranging from 200 to 220 Trad/s, and the features become deviating from the light line with the dominant confinement effect on the surface. Therefore, we believe it is plausible that surface phonon polaritons are supported. The shrunk wavelength along the surface, unlike the free-space wavelength, efficiently enhances the absorption cross-section. Correspondingly, the higher confinement (high q) yields shorter propagating length (Fig. 5.24(c)), which implies more efficient absorption.
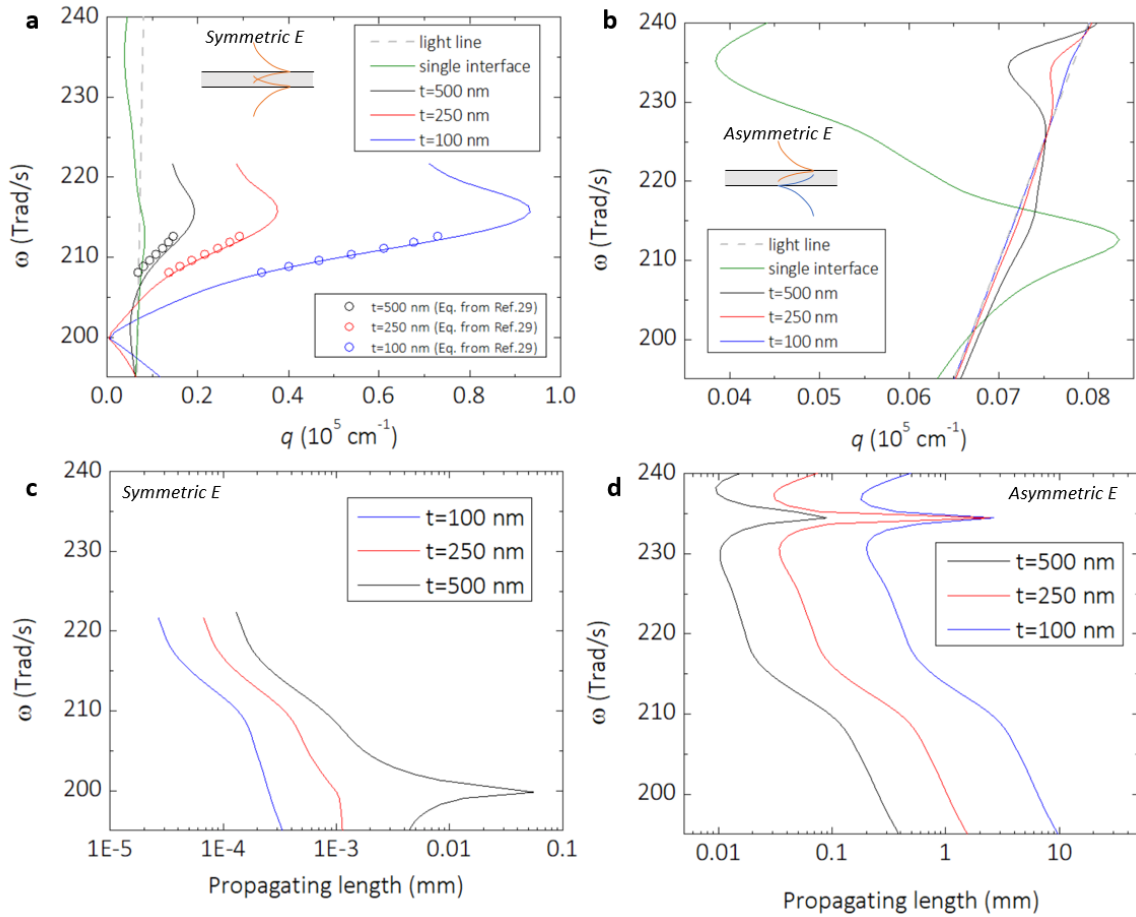
Figure 5.24 Dispersion relations of thin films with various thicknesses, in the cases of symmetric (a) and asymmetric (b) configurations of electric fields. (c,d) Plots of propagating length, $1/(2\kappa)$, of symmetric (c) and asymmetric (d) modes, respectively. TM polarization was considered as described in Fig 5.23.
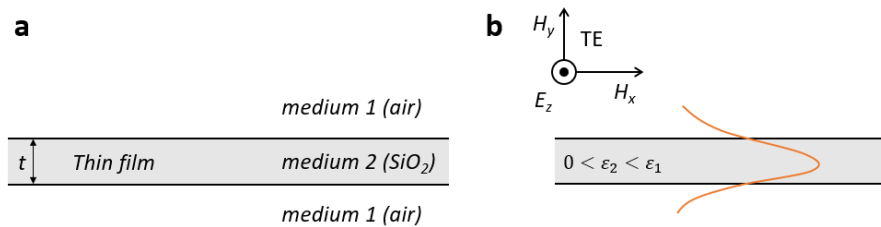
Figure 5.25 Schematics of (a) a thin film structure consisting of a medium 2 surrounded by 1, and (b) TE wave guide mode.

TE polarization does not have an electric field component normal to the surface as shown in Fig. 5.25, thus it cannot support surface waves unless permeability, μ has negative values to form polaritons by magnetic fields in an infinite slab while it still makes reflection at the interface as:

$$r_{TE} = -\frac{\mu_2 k_{t,1} - \mu_1 k_{t,2}}{\mu_2 k_{t,1} + \mu_1 k_{t,2}}, \text{ where } \mu_1 = \mu_2 = 1. \tag{5.47}$$

The only available solution to satisfy positive $k_{t,1}$ is following:

$$r_{TE} = -e^{ik_{t,2}t} = -\frac{k_{t,1} - k_{t,2}}{k_{t,1} + k_{t,2}} \tag{5.48}$$

$$1 = -\frac{k_{t,2}}{k_{t,1}} \tanh\left(\frac{t}{2i} k_{t,2}\right) \tag{5.49}$$

$$1 = -\frac{t}{2i} \frac{k_{t,2}^2}{k_{t,1}}, \text{ in the thin film limit } (k_{t,2}t \ll 2). \tag{5.50}$$

The analytically calculated dispersions were shown in Fig. 5.26(a). There is a sharp change in the propagating vector, q at around 200 Trad/s, deviating from the light line. More specifically right below ω_{LO} (200 Trad s^{-1}), the real part of ε_{SiO_2} becomes smaller than that of air ($\varepsilon_{air} = 1$) down to 199 Trad s^{-1}. In this regime, the repeated internal reflections within the SiO$_2$ can generate the guided modes in the SiO$_2$. However, the effective energy range is very narrow to meet $\varepsilon_{SiO_2} < \varepsilon_{air}$, furthermore, the thin structure diminishes the guiding effect. The lowest order of the guide modes requires a half of the wavelength at least in dimensions. In addition to the guiding effect, the SiO$_2$ also can be considered as a lossy dielectric layer with high refractive index, especially at around 190 Trad/s because of the peaks of both real and

imaginary parts of permittivity. Therefore, the effective refractive index of a thin film surrounded by air will be closer to that of air with smaller lossy volume.
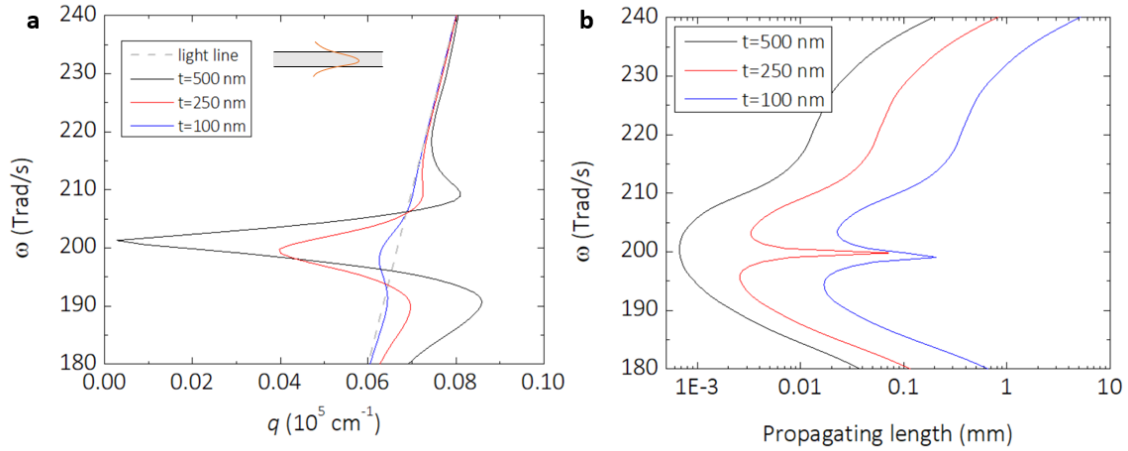
Figure 5.26   (a) Dispersion relations and (b) propagating length of thin films with various thickness, in the case of TE polarized wave-guided modes.

Based on the mode analysis from a 2D infinite slab, it is concluded that the confinement effect with a small thickness (e.g. 100 nm in our experiments) is highly dominant by symmetric modes of TM polarization. The smaller wavelength of surface phonon polaritons, compared to that of free space, enhances absorption efficiency, which is determined by the ratio of absorption cross-section to geometric cross-section. Owing to the shrunk wavelength along the surface (λ_{SPhP}), the absorption efficiency increases with the thinner thickness within the Reststrahlen band. On the other hand, in the regime where the SiO_2 behaves as a lossy dielectric absorber, rather than a metal, it shows higher absorption with the larger volume.
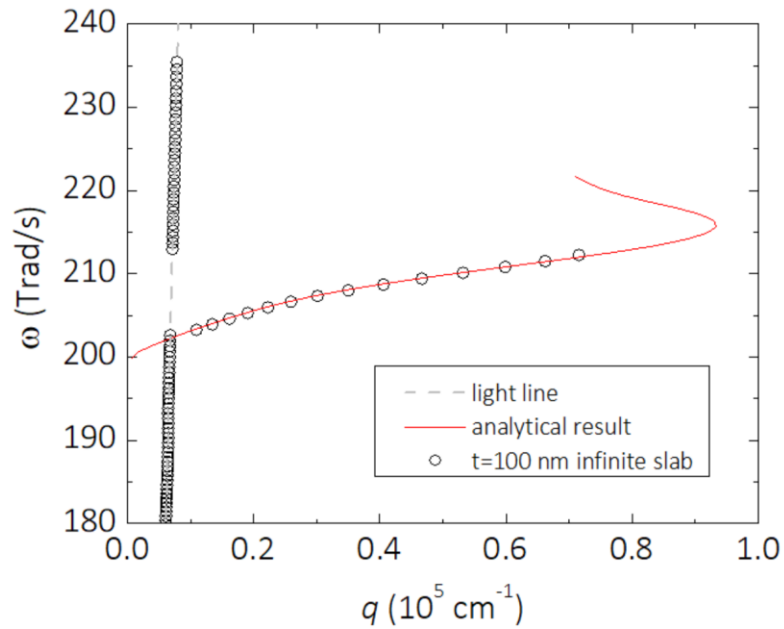
Figure 5.27   Dispersion of an infinite slab by numerical modelling with 100 nm thickness.
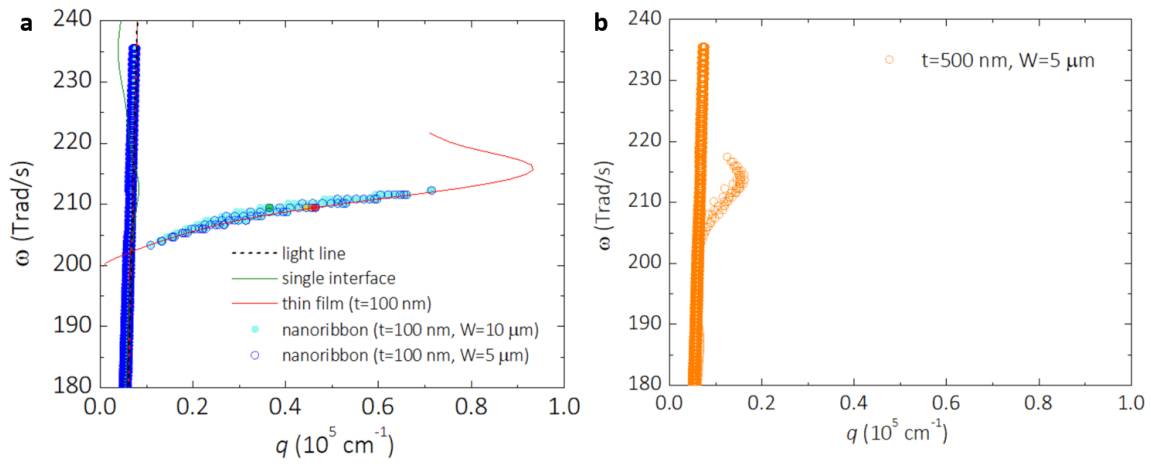
Figure 5.28   Dispersions of nanoribbons by numerical modelling with (a) 100 nm and (b) 500 nm thickness.

5.8 Conclusions

In summary, we studied the coherent thermal emission in the far field via anisotropic dimension control of polaritonic nanoribbons. The combination of heat-transfer measurements and optical modelling provided a new platform to precisely engineer and quantify the coherent thermal emission of an individual nanoscale object. This developed technique enabled us to determine that the anisotropic polaritonic nanoribbon design provides an extra degree of freedom to realise a nanoscale coherent thermal emitter with no design limitation in terms of its length. The thin structure effectively suppressed incoherent emission in the broad range of the spectrum, and the controlled width of the nanoribbon enhanced the coherent emission mediated by SPhPs. Furthermore, we observed a higher coherent enhancement factor (CEF up to 8.5) at lower temperature, which clearly emphasises the dominant coherent emission in the nanoribbon structures. The upper limit of the CEF can be further improved by engineering the dispersion of the emitter. Use of the grating effect by periodically arranging the nanoribbons[154,161] and/or metamaterials can lead to more confined surface modes by SPhPs with a higher Q factor. In addition, the spatial distribution of coherent thermal emission can be controlled by selectively limiting polarisation. Such coherent thermal emitters with a selective spectral/spatial band could find wide-ranging applications for thermal management, energy conversion, bio/chemical sensing, light emission, and micro/nanomanufacturing.[154,161,193-197]

Acknowledgements

Chapter 6

Plasmonically-Enhanced Thermal Radiation by Surface Phonon Polaritons

6.1   Introduction

Recent efforts to manipulate heat as light have spurred intensive researches on radiative heat transfer.[149,160,161,165] Unlike the traditional concept of heat which is incandescent, thermal emission via surface polaritonic resonance arisen from light-matter interaction has been considered as a promising way to effectively utilize the ubiquitous thermal energy by converting it into the coherent energy source.[161,198] Owing to the fact that the surface wave can carry the highly confined energy beyond the diffraction limit, there have been extensive theoretical and experimental studies on near-field thermal radiation[149,151,199]. To intensify radiative heat flux, nanogaps smaller than the thermal wavelength (λ_T) have been used to enhance constructive interference of the evanescent waves from the two opposing surfaces. Sub 100 nm gaps have been experimentally achieved, and it has been proved that the thermally excited surface wave generates strong near-field radiation breaking the limit of black body radiation described by the Planck's law[200,201].

Unlike the evanescent near-field radiation, far-field radiation with nanoscale objects has been generally considered to be far below the black-body limit because the smaller

dimension than the skin depth (δ) lowers the capability to absorb the electromagnetic waves, ultimately yielding low emission followed by Kirchhoff's law. This is so-called the volumetric effect[165]. Recent theoretical and experimental studies have shown the promise of anisotropic nanostructures to exceed the blackbody limit within the selected angular and spectral ranges using optical guide modes[162,163,198]. In another aspect, an individual nano-object can maximize the view-factor of radiation, so-called absorption cross-section. Especially, highly anisotropic structures would have a stronger antenna-effect, which could potentially yield super-Planckian features in a certain directional and/or spectral range. Our previous work reported that long nano-ribbon structures of SiO_2 enhanced emissivity (ε) beyond the thin film limit via the confined surface energy of SPhPs[198]. The ε of an individual nano-object was measured using a sensitive thermometry platform. The quantitative study revealed the contribution of SPhPs to enhance thermal radiation with anisotropic structures. Importantly, the enhancement by polaritons ensures photonic engineering of heat transport by manipulating the optical properties of surroundings and emitters. However, the experimental study of nanoemitters for efficient heat transfer is still at an early stage, and the reported ε of ~0.2, albeit higher than the thin film value of 0.062[198], is still much lower than the blackbody limit. To achieve high emission, broadened spectral absorption near the peak of Planckian distribution is required as well as high energy confinement to enhance the optical cross-section.

It is clearly beneficial to employ SPhPs to manipulate radiative heat transfer at room temperature owing to the fact that the dominant thermal wavelength at 300 K (i.e., ~10 μm) is located within the Reststrahlen band energy regime where SPhPs can be supported. SPhP has narrow spectral response within the Reststrahlen band bounded by two resonance

frequencies of transverse and longitudinal optical phonons (e.g., ω_{TO} and ω_{LO}). At the same time, compared to surface plasmon polaritons, SPhP has low loss at around ω_{TO}, which can lead to high quality (Q) factor of >100s. While it implies selective feature of SPhPs, the narrow band response and lower imaginary part of permittivity limit the total energy flux that can be absorbed or emitter from a single object, which is the product of the integration over the entire spectral range. On the contrary, SPPs can support more broadband spectral response due to its high loss below their characteristic frequency, so-called plasmonic resonant frequency (ω_P). However, there is a giant discrepancy between the ω_P (usually in the UV-vis regime) and the thermal wavelength at room temperature (in the mid infrared regime). Therefore, most the previous studies showing noticeable effect of SPPs on far-field thermal radiation have been done at high temperature.[156,157]

In this study, we employ a metal-dielectric metasurface to tune the energy dispersive property at the surface by using hybrid modes of SPhPs and SPPs. For example, Au NPs of ~50 nm diameters are dispersed on SiO_2 nanoribbons (NRs) (i.e., 100 nm thickness, 10 μm width and 400 μm length) as shown in Fig. 6.1. Although the SPP mode itself does not efficiently support the thermal emission in the IR regime due to the strong reflection of the surface with high refractive index (n~10), the metallic surface of Au nanoparticles (NPs) allows localized energy confinement at the SiO_2 surface over the broader spectral enhancement compared to the energy dispersion of SiO_2 only.

6.2 Results and Discussion

6.2.1 Comparison of Dispersion Relations

Metals and polar dielectrics present different optical property, determined by the Drude and the Lorentz model, respectively. Figures 6.1(d,e) show the distinct permittivity of Au and SiO$_2$. The plasmonic resonant frequency (ω_P) of Au corresponds to ~ 300 nm wavelength, thus, SPP modes lead to the maximum peak of emittance in the UV regime. At frequencies below ω_P, both real (ε') and imaginary (ε'') parts of the permittivity show monotonic increase (Fig. 6.1(d)). The surface modes can still be supported over the broad energy range, but the high refractive index results in strong reflection at the surface. High reflectance blocks absorption in the emitter, so it reduces the emission enhancement by SPP modes in the IR regime. On the other hand, SiO$_2$ presents two resonant frequencies by optical phonons at around 10 μm (i.e., 8 μm and 9.5 μm for transverse optical (*TO*) and longitudinal optical (*LO*) phonons, respectively), and the two frequencies are closely located. The refractive index becomes zero at the resonant frequencies, thus the energy dispersion of the polar dielectrics involves sharp transitions near the boundary of the Reststrahlen band, as shown in the permittivity of SiO$_2$ (Fig. 6.1(e)). Evidently, SPPs and SPhPs have highly dissimilar energy dispersions. However, metasurfaces with hybridized SPPs and SPhPs can provide a novel approach to manipulate the energy dispersion to engineer the thermal emission.

To study the energy dispersive property of the metasurfaces, we modeled the dispersion relations of various surface structure using a finite element method (COMSOL Multiphysics). The anisotropic structures with high aspect ratios require extensive numerical

calculation. Here we employed 2D modeling to understand the physical mechanisms. We consider three cases in the model: A SiO$_2$ NR with infinite length was considered with and without an Au array on top of it, as well as Au array only (no SiO$_2$ substrates). In Fig. 6.2(a), the solid lines represent the analytical modeling results of thin films of SiO$_2$ and Au, both with 100 nm thickness and infinite lateral dimensions , and the numerical results (symbols) of the Au array, SiO$_2$ NR and Au/SiO$_2$ hybrid structure were overlaid for comparison. As expected, Au and SiO$_2$ layers induce the confined surface modes with a peak in the propagating vector, q, in the UV-vis and IR regime, respectively. The peak intensity is much higher for SPhPs with SiO$_2$ but the effective energy range is much narrower. Interestingly, the hybrid Au/SiO$_2$ layer could effectively combine two different features from SPP and SPhP modes. The hybrid mode sustains the peaks near the resonant frequencies of each mode, and more interestingly, the confined dispersion in the IR regime by SPhPs is broadened. Thus, the spectral emittance can be enhanced over the broader mid-infrared range, and enhance the ε.

Introducing the Au layer on top of SiO$_2$ enables further localization of the electromagnetic waves at the surface in the broadened energy regime. For instance, the metal NPs introduces a highly reflective surrounding (e.g., n~10 for Au at 10 μm wavelength) on the SiO$_2$ surface. The cavity-like feature leads to a stronger localized effect (Fig. 6.2(c)), and decrease the propagating length (Fig. 6.2(e)). It is interesting that while the intrinsic Au has almost zero ε due to the strong reflection, it can be used to support efficient emission of SiO$_2$ in the IR regime. Figures 6.2(c-d) show the cross-sectional views of the ribbon structures and the polarization configurations of the magnetic field. Indeed, the field intensity is stronger at

the SiO$_2$ surface with Au arrays, and ultimately, it reduces the propagating length by making

the surface modes more lossy(Fig. 6.2(e)).
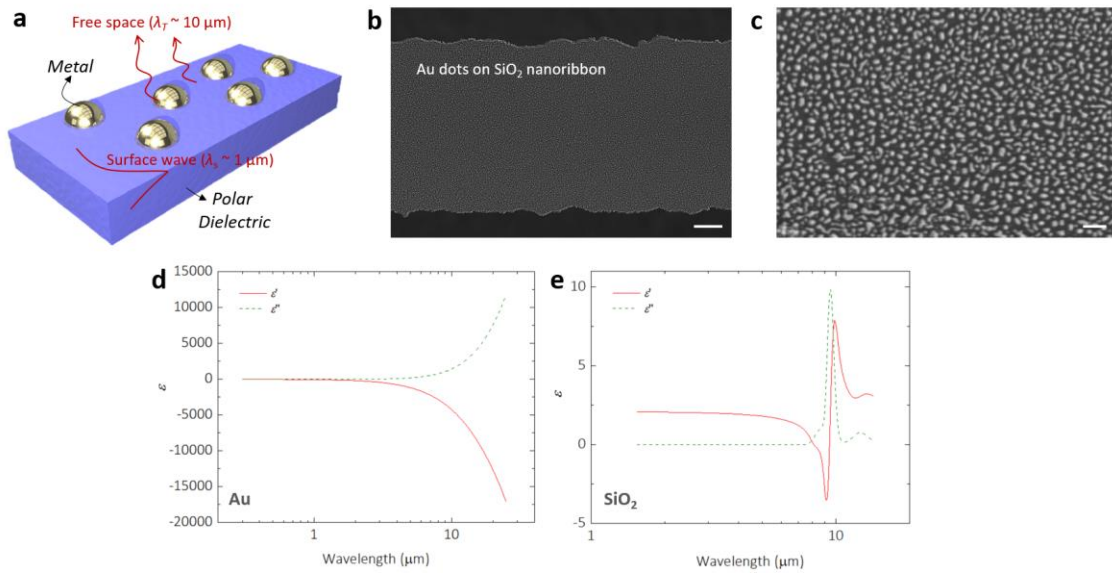
Figure 6.1   (a) Schematic of metasurfaces, consisting of metal NPs on a polar dielectric NR. (b,c) SEM images of Au dots deposited on the SiO$_2$ NR. The scale bars indicate 2 μm and 200 nm for (b) and (c), respectively. Permittivity of Au (d) and SiO$_2$ (e) as a function of wavelength.
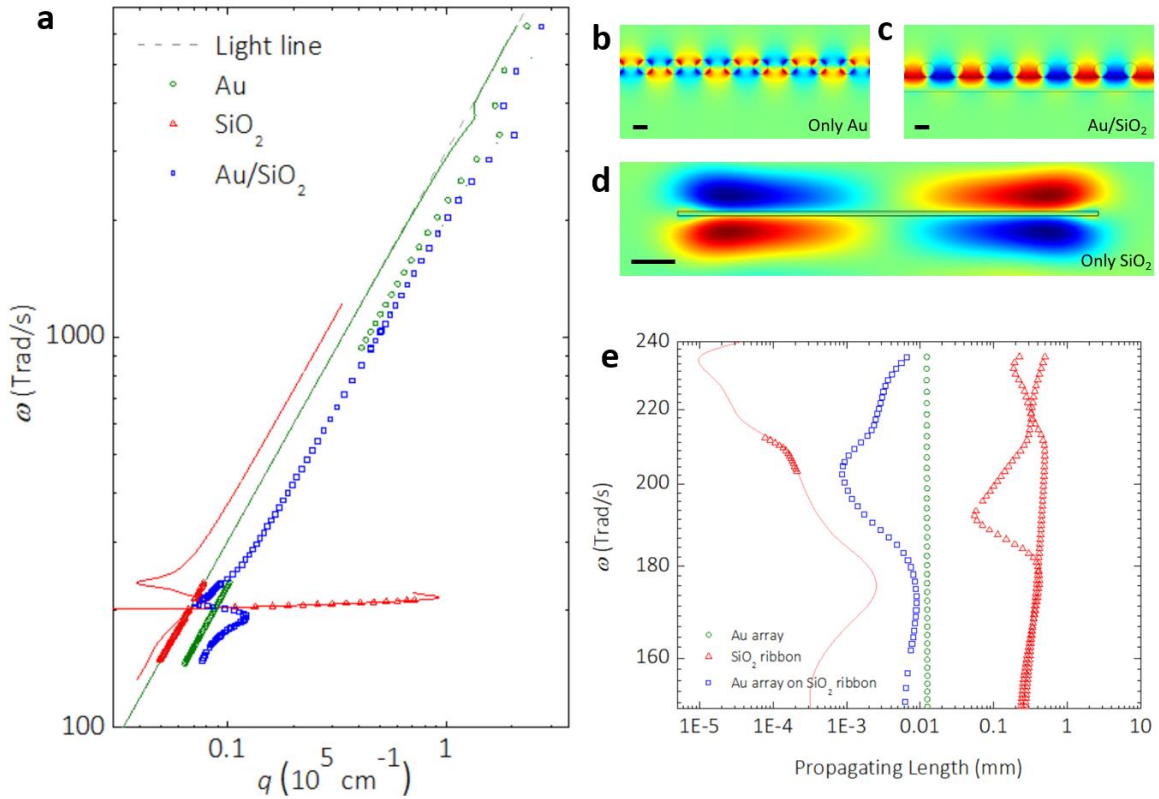
Figure 6.2   (a) Plots of energy dispersions of the sole Au or SiO$_2$ structures and hybrid Au-SiO$_2$. Magnetic field images at 9 μm wavelength for the sole Au (b) and hybrid Au-SiO$_2$ surface (c) and the sole SiO$_2$ (c). (e) Plots of propagating lengths.

6.2.2   Heat Transfer Measurement

The figure of merit for far-field thermal radiation can be indicated by the ε value. Now, we seek to experimentally measure the ε with the metasurfaces. There has been a lack of direct thermal probing methods to study far-field thermal radiation from nanoscale objects. Most of the experimental methods have been the optical characterization of spectral and spatial features of thermal radiation, such as scattering type scanning near-field optical microscope (s-SNOM) and thermal radiation scanning tunneling microscope (TRSTM),

etc.[158,164,170] The scanning techniques enables the detection of the local near-field interaction of polar dielectric objects with lateral size down to 10 nm[171], where a strong resonance peak and a high local electromagnetic energy density were observed due to SPhPs. Also, direct heat flux measurement of energy exchange due to evanescent waves of SPhPs in the near-field regime has been carried out[149,150], which proved that SPhPs generate strong near-field radiation breaking the Planckian limit. On the other hand, the near-field study limits the available investigations to the surface with nanoscale gaps. The developed local probes and near-field heat transfer experiments are infeasible yet to evaluate the resonant effect in the far-field. The intensity of the evanescent wave would exponentially decay with the distance from the surface, and eventually, the enhanced radiative intensity becomes negligible. Similarly, more common optical methods to study far-field radiation, based on Fourier-transform infrared spectroscopy (FTIR) could not quantify absolute emissive power from nanostructures, as it needs to deal with the diffraction limit.

To avoid the issues in optical measurements, we directly applied Joule heating to a micro-fabricated heater (Fig. 6.3(a)). By making the heater suspended and connected to the reservoirs at both ends, we can locally heat it up with a peak temperature rise in the middle of the metal beam as shown in Fig. 6.3(a). The temperature rise can be controlled by electric current (I) and thermal conductance of the heater (G_{beam}).

$$\frac{I^2 R_{beam}}{2} = G_{beam}(T_h - T_0) = G_{beam}\theta_h \tag{6.1}$$

where R_{beam} is the resistance of the heater, T_h is the temperature at the center of the beam, T_0 is ambient temperature, and θ_h is a temperature rise intensity at the heating side with AC heating.
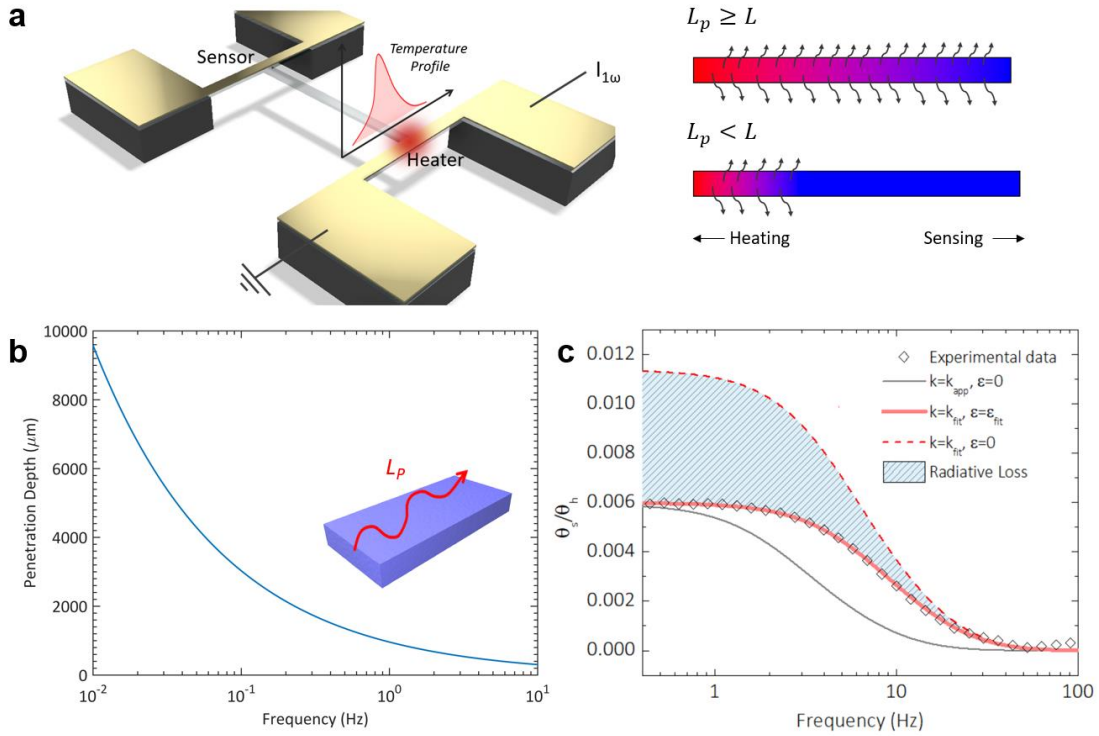
Figure 6.3   Schematics of the measurement platform (a) and thermal penetration depth (L_p). (b) A plot of the penetration depth as a function of the heating frequency. (c) Plots of the temperature rise ratio with experimental data (symbols) and fitted results (lines), where the shaded area indicate the influence of radiative loss.

The hybrid emitter (e.g. Au/SiO$_2$) is located across the two suspended metal beams (Fig. 6.3(a)). We probe the temperature rise (θ_s) at a sensing beam by measuring the resistance change. Typical metals (i.e., Au and Pt) have a linear relation of resistance and temperature, and the degree (e.g., slope) is defined as the temperature coefficient of resistance (*TCR*).

$$TCR = \left(\frac{dR}{dT}\right)\Big/ R_0 \tag{6.2}$$

where R_0 is resistance at room temperature. In this study, we used a thin Pt layer (~80 nm) with an adhesive Ti layer for both sensing and heating beams. Heat transport along the ribbon

144

is dominated by radiation and conduction. Convection heat transfer is negligible with a high vacuum level of the enclosed measurement chamber ($\sim 10^{-6}$ Torr). Therefore, we used a fin model to analyze the measured temperature rise (θ) by characterizing radiative and conductive heat transport.

Our previous work introduced the measurement platform to quantify the ε of SiO$_2$ NRs[198]. The ε was extracted with various lengths of the NRs. The length-dependent measurement requires a negligible variation in the material properties (namely, thermal conductivity κ and emissivity ε) among the multiple samples to extract a single ε value. Amorphous SiO$_2$ sustains a bulk-like κ even at nanoscale due to the short phonon mean free path. However, in a complex system, such as the metasurfaces, their thermal properties have not been well-studied and could depend on geometry or vary from sample to sample. In particular, our Au NPs were prepared by annealing a sputtered Au layer on the SiO$_2$ NRs, so they were randomly shaped. Since it is difficult to prepare the identical Au structures for the length-dependent study, in this work, we developed the heat transfer measurement platform in the frequency domain. This new methodology enables us to characterize the ε value in a single experimental sample. In addition, the platform allows us to obtain κ and ε simultaneously, thus it does not require to know thermal conduction to reveal radiation using a fin model.

A controlled heating frequency affects thermal penetration depth (L_p) as:

$$L_p = \sqrt{\frac{\alpha}{\omega}} = \sqrt{\frac{\kappa}{\rho C \omega}} \tag{6.3}$$

where α, ω, κ, ρ and C are thermal diffusivity, angular frequency, thermal conductivity, density and specific heat capacity, respectively. In the low frequency regime where the L_p

becomes much longer than the sample length (L), the radiative heat loss would be effective over the entire sample length. As increasing the heating frequency, the L_p is reduced which decreases the effective surface area to contribute to radiation. The controlled frequency study works as an alternative way to which is an alternative way to effectively change the relative contribution of heat conduction and thermal radiation, as we have done by varying the physical length of the specimen in our earlier work presented in Chapter 5. For instance, as shown in Fig. 6.3(c), we can calculate the temperature rise ratios as a function of heating frequency, and compare the experimental data with fitted lines with κ and ε. We can expect a larger contribution of the radiative heat loss at the low frequency regime due to the longer thermal penetration depth, and it results in mismatch in heat transfer modeled results with and without radiative heat loss (see lines in Fig. 6.3(a)).

Now, we consider the fin model in the time domain (Fig. 6.4):

$$\frac{\partial T(x,t)}{\partial t} = \alpha \frac{\partial^2 T(x,t)}{\partial x^2} - \frac{hP}{\rho CA}\left[T(x,t) - T_0\right] \tag{6.4}$$

$$\frac{\partial \Delta T}{\partial t} = \alpha \frac{\partial^2 \Delta T}{\partial x^2} - \frac{hP}{\rho CA} \Delta T \tag{6.5}$$

where $\Delta T \equiv T - T_0$, h is a radiative heat transfer coefficient ($= 4\varepsilon\sigma T^3$), P is a perimeter, and A is a cross-sectional area In the frequency domain, by setting $\Delta T(x,t) = \theta(x)e^{j\omega t}$, Eq. (6.5) becomes:

$$j\omega\theta(x)e^{j\omega t} = \alpha \frac{d^2\theta(x)}{dx^2}e^{j\omega t} - \frac{hP}{\rho CA}\theta(x)e^{j\omega t} \tag{6.6}$$

$$j\omega\theta(x) = \alpha \frac{d^2\theta(x)}{dx^2} - \frac{hP}{\rho CA}\theta(x) \tag{6.7}$$

$$\frac{d^2\theta(x)}{dx^2} - \frac{j\omega}{\alpha}\theta(x) - \frac{hP}{\rho CA\alpha}\theta(x) = 0 \tag{6.8}$$

$$\frac{d^2\theta(x)}{dx^2} - \frac{j\omega}{\alpha}\theta(x) - \frac{hP}{\kappa A}\theta(x) = 0 \tag{6.9}$$

$$\frac{d^2\theta(x)}{dx^2} - a^2\theta(x) = 0 \tag{6.10}$$

with $a^2 = \dfrac{j\omega}{\alpha} + \dfrac{hP}{\kappa A}$.

$$\theta_i(x) = C_i' \cosh(a_i x) + C_i'' \sinh(a_i x) \tag{6.11}$$

where C' and C'' are constants, and $i=1,2$ for the heating beam and the NR (sample), respectively. For the sample with $-L < x < 0$,

$$\theta_2(x) = C_2' \cosh(a_2 x) + C_2'' \sinh(a_2 x) \tag{6.12}$$

$$(a_2)^2 = \frac{j\omega}{\alpha_2^{~2}} + \frac{h_2 P_2}{\kappa_2 A_2}. \tag{6.13}$$

For the metal beam with $L < x < L_b$,

$$\theta_1(x) = C_1' \cosh(a_1 x) + C_1'' \sinh(a_1 x) \tag{6.14}$$

$$(a_1)^2 = \frac{j\omega}{\alpha_1^{~2}} \tag{6.15}$$

with a negligible radiative heat loss for metals have a low ε close to zero. At $x = 0$,

$$\theta_1(0) = C_1' = \theta_s \tag{6.16}$$

$$\theta_2(0) = C_2' = \theta_s \tag{6.17}$$

$$-\kappa_2 A_2 \left.\frac{dT_2}{dx}\right|_{x=0} = -\kappa_1 A_1 \left.\frac{dT_1}{dx}\right|_{x=0} \tag{6.18}$$

$$-\kappa_2 A_2 C_2'' a_2 = -\kappa_1 A_1 C_1'' a_1. \tag{6.19}$$
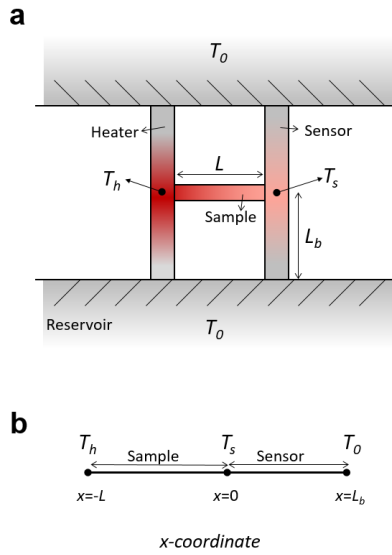
Figure 6.4   A schematic (a) and the corresponding thermal circuit diagram of a suspended device.

At $x = L_b$,

$$\theta_1(L_b) = C_1' \cosh(a_1 L_b) + C_1'' \sinh(a_1 L_b) = 0 \tag{6.20}$$

$$\theta_1(L_b) = \theta_s \cosh(a_1 L_b) + C_1'' \sinh(a_1 L_b) = 0. \tag{6.21}$$

At $x = -L$,

$$\theta_2(-L) = \theta_s \cosh(-a_2 L) + C_2'' \sinh(-a_2 L) = \theta_h \tag{6.22}$$

$$\theta_2(-L) = \theta_s \cosh(a_2 L) - C_2^{"} \sinh(a_2 L) = \theta_h. \tag{6.23}$$

$$C_1^{"} = -\theta_s \frac{\cosh(a_1 L_1)}{\sinh(a_1 L_1)} \tag{6.24}$$

$$C_2^{"} = \frac{\theta_s \cosh(a_2 L) - \theta_h}{\sinh(a_2 L)} \tag{6.25}$$

$$-\kappa_2 A_2 a_2 \frac{\theta_s \cosh(a_2 L_2) - \theta_h}{\sinh(a_2 L_2)} = -\kappa_1 A_1 a_1 \frac{-\theta_s \cosh(a_1 L_1)}{\sinh(a_1 L_1)} \tag{6.26}$$

$$\theta_s \left(\kappa_1 A_1 a_1 \frac{\cosh(a_1 L_1)}{\sinh(a_1 L_1)} + \kappa_2 A_2 a_2 \frac{\cosh(a_2 L_2)}{\sinh(a_2 L_2)} \right) = \theta_h \frac{\kappa_2 A_2 a_2}{\sinh(a_2 L_2)} \tag{6.27}$$

Finally, we can summarize the temperature rise ratio as

$$\frac{\theta_s}{\theta_h} = \frac{1}{\dfrac{\kappa_1 A_1 a_1}{\kappa_2 A_2 a_2} \dfrac{\sinh(a_2 L_2)}{\tanh(a_1 L_1)} + \cosh(a_2 L_2)}. \tag{6.28}$$
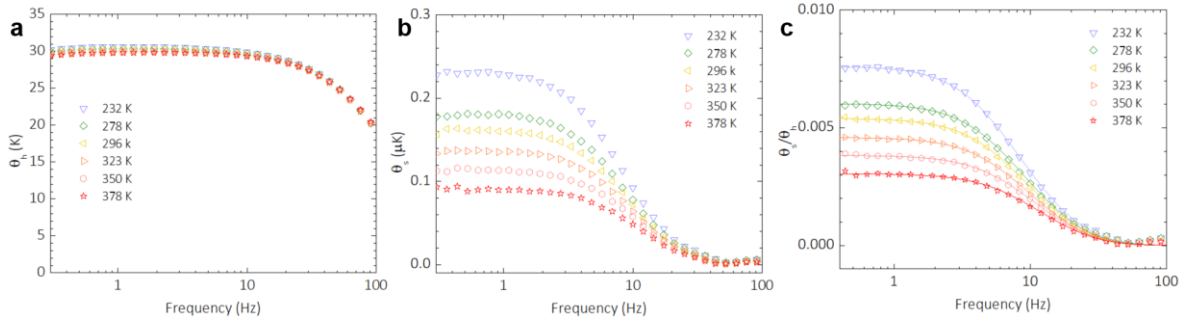
Figure 6.5   Plots of the measured θ_h (a), θ_s (b) and θ_h/θ_s (c) as a function of heating frequency at various temperatures. Fitted lines are overlaid in (c).

As shown in Fig. 6.5, we detected the temperature rise in the heater and sensor with the modulated Joule heating. The experimentally obtained temperature rise ratios (θ_h/θ_s) were fitted with the modeled results based on Eq. 6.28. In Fig. 6.5(c), the solid lines are fitted curves, and the results are well overlapped with the experimental data. The extracted κ and ε are discussed in the following section.

6.2.3   Emissivity Enhancement

Figure 6.6 shows the experimentally measured apparent thermal conductivity (κ_{app}), fitted thermal conductivity (κ) and ε as a function of temperature. The κ_{app} is determined in the low frequency regime where the θ_h/θ_s is saturated, and it is proportional to the θ_h/θ_s as

$$\frac{\theta_s}{\theta_h} = \frac{G_{app}}{G_{beam} + G_{app}} \tag{6.29}$$

$$G_{app} = \kappa_{app} \frac{A_c}{L} \tag{6.30}$$

where G_{app} and G_{beam} are apparent and beam thermal conductance, respectively. In the absence of radiative heat loss, the κ_{app} would be the κ determined by heat conduction only. Our samples include significant radiation, which can be comparable to heat conduction. Radiative heat transport reduces the κ_{app} by exponentially decaying the temperature while heat transports along the sample from the heater to the sensor. The degree of exponential reduction is weighted by a_2 as described in Eqs. 6.13 and 6.28. Hence, we can see the larger deviation between κ_{app} and κ at the higher temperature with the increased influence of radiation in Fig. 6.6(a).
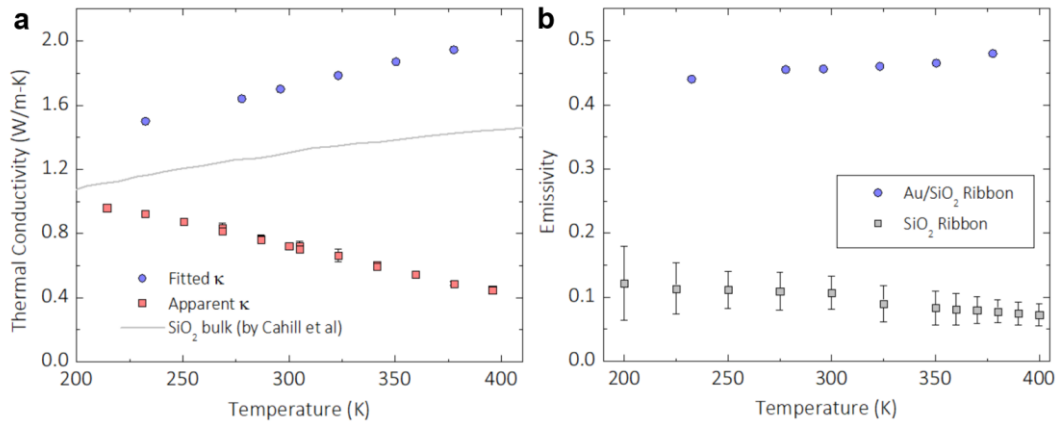
Figure 6.6   Plots of apparent and fitted thermal conductivity (a) and emissivity (b) of 400 µm long Au/SiO₂ NR.

Unlike the bare SiO_2 emitter which sustains bulk-like thermal conductivity in nanoscales, the randomly distributed Au NPs on SiO_2 makes it difficult to predict the κ. To characterize two unknown parameters (e.g., κ and ε) simultaneously from the measured θ_h/θ_s, we studied the θ_h/θ_s with various heating frequencies which control the L_p (Eq. 6.3). By fitting the experimental data in Fig. 6.6(c) using Eq. 6.28, we could extract both κ_{app} and ε as shown in Fig. 6.6(a) and 6.6(c), respectively. The κ_{app} was compared to the bulk thermal conductivity of SiO_2. The existence of Au NPs slightly increases the conductivity, but due to the discontinuous feature of the Au layer, the κ is still close to that of SiO_2. We also analyzed the ε of the Au/SiO₂ emitter as shown in Fig. 6.6(b). The Au coated sample showed considerably higher ε of 0.46 compared to the bare SiO_2 sample at 300 K (e.g., ε of 0.11 with 10 µm wide SiO_2 ribbon at 300 K). The presence of Au NPs significantly enhances the ε by a factor of 4.

The enhancement at near 300 K is the result of coupled SPP and SPhP effect that modify the SPhP dispersions in the IR regime.

To directly visualize the enhanced thermal emissivity of SiO_2 with gold NPs, we also measured the IR thermal images with patterned SiO_2 structures with and without the Au NPs as shown in Figs. 6.7 (a,b). The SiO_2 layer was patterned into 'UCSD' letters using standard photolithography and etching processes. The patterns were prepared on top of a Si wafer substrate with a Cu block for uniform thermal background. The entire device was placed on the hot plate at 135 °C for thermal imaging. We could clearly see the 'UCSD' patterned word in Figs. 6.7(d,f) with the Au layer. It is because the high ε at the metasurface could effectively radiate the thermal energy.
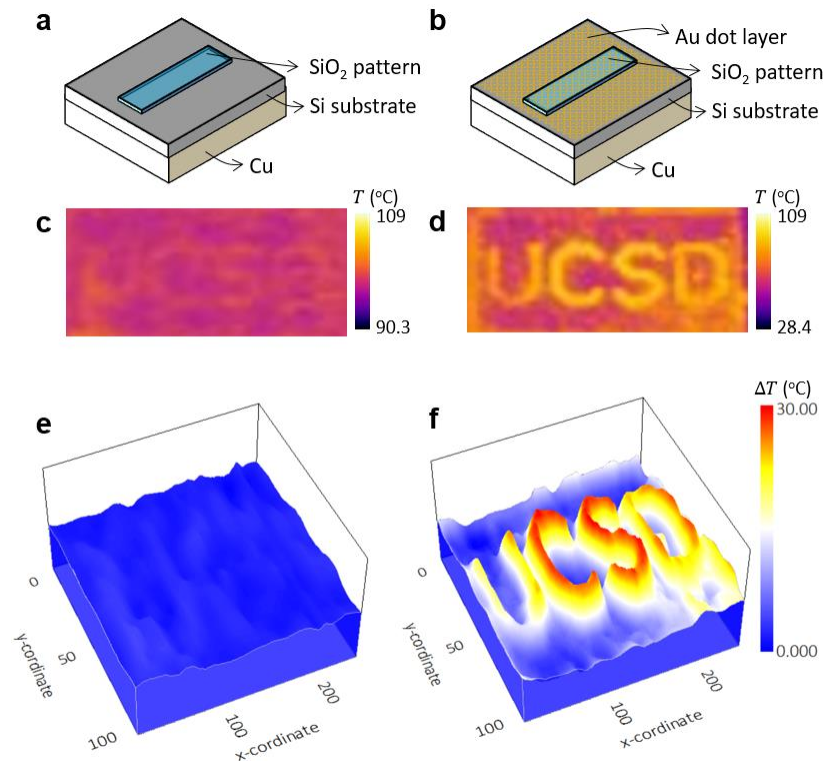
Figure 6.7   Schematics of a Si substrate patterned by SiO_2 only (a) and Au/SiO_2 (b). IR thermal imaging of SiO_2 only (a,e) and Au/SiO_2 (b,f) surfaces, measured at 135 °C.

6.3 Conclusions

In this study, we employed a novel metasurface of Au/SiO$_2$ to engineer the energy dispersion of SPhP in the mid-infrared regime. We developed a facile, frequency domain heat transfer measurement platform by integrating the emitter to the micro-fabricated heater and sensor. We controlled the thermal penetration depth with AC heating. Our novel analysis using a fin model could simultaneously get κ and ε from one single sample. Importantly, we observed significantly enhanced ε of the Au/SiO2 metasurface at near the room temperature, a factor of 4 enhancement over the bare SiO$_2$ NR, due to the coupled SPP and SPhP modes. The resultant dispersion possesses strong confinement effect with short propagating length in the mid-IR regime by virtue of the SPhP surface modes, but the effective energy range becomes broader with the existence of Au NPs which supports SPPs. This work provides a clear pathway to enhance far-field thermal radiation in a nanoscale phonon polariton emitter.

Acknowledgements

Chapter 7

Quasi-Ballistic Polaritonic Heat Conduction: Shedding "Light" on Thermal Transport

7.1   Introduction

In classical textbooks of thermal physics, there are three modes of thermal transport: conduction, radiation, and convection. And it is no secret that conduction and radiation are treated as two separated worlds as they have vastly distinct characteristics: Heat conduction in solids is normally described by a diffusion process with short mean free path (Λ) associated with the main heat carriers, such as phonons and electrons. Extraordinary (non-diffusive) heat conduction has only been observed in exotic systems under unusual conditions, such as ballistic and divergent heat conduction in one dimensional (1D) carbon nanotubes [202,203] and 2D graphene [204], quantized heat conduction in nanoscale phononic or electronic waveguides at sub-Kelvin temperature [205,206] or in atomic junctions [207], coherent transport in epitaxial superlattice [195,196]. Photons for radiation (e.g., infrared thermal radiation), on the other hand, usually have very long propagating length unless they are scattered by disordered media. However, photons are typically not confined and their energy intensity is orders of magnitude lower than that of heat conduction in solids (the effective thermal conductivity of even the near-field radiation heat transfer in a 1-nm gap [199,200] is lower than that of air).

However, these two separated worlds can intersect in the form of surface phonon polariton (SPhP), which emerges due to the collective oscillation of atoms on the surface of a polar dielectric induced by electromagnetic waves, i.e., coupling between optical phonon and photon. The coupling converts the incandescent background into a coherent wave guided along the surface due to the resonance, a new regime of heat conduction mediated by SPhP. SPhP modes exist in polar dielectric solids with a negative refractive index of the solid ($\varepsilon_2 <$ 0) surrounded by a medium with a positive refractive index ($\varepsilon_1 > 0$) [160], such as amorphous and crystalline SiO_2 (glass [208] and quartz [209]), SiC [210], hexagonal BN [211], and III-V semiconductors [212], with the spectral range lying between the longitudinal (*LO*) and transverse optical (*TO*) phonon frequencies, or the so-called "Reststrahlen" band.

We seek to explore extraordinary polaritonic heat conduction in polar dielectric nanostructures made from ordinary materials such as glass (amorphous SiO_2) and SiC. Unlike incoherent thermal radiation of a blackbody, the evanescent surface wave by SPhPs is highly confined and can directionally propagate along the interface between the polar dielectric solid (which is metallic in the interested IR regime) and its surrounding such as air. The directional radiation guided by the structure blurs the boundary of heat conduction and radiation. Instead of distinct definitions from each one of them, heat transport by SPhPs can be best understood as a coupled mode. The physical cross-section for the energy transfer is not limited to the solid, but rather expands into the free space (air or vacuum) with radiative nature, but the heat flux would be intensified at the surface and thus it can result in heat conduction as a 1D channel. More interestingly, under suitable conditions, SPhP can also have extremely long propagation lengths (>*mm*) even at room and high temperature [160,213,214], and therefore, can exhibit extraordinary behaviors over a much longer distance, such as non-

diffusive, divergent thermal conductance, quantum transport, and surface/interface dominated thermal conductivity.

The most notable use of SPhPs in thermal transport so far is perhaps in near-field radiation heat transfer, where the tunneling of evanescent SPhPs can greatly enhance the energy transfer through a near-field nanogap, with the heat conduction greatly exceeding the Planckian limit [149,151,153,199]. Besides radiative heat transfer that occurs across a vacuum gap between two interfaces, energy transport *via* SPhP *along* the interface could also be significant. Theoretical studies have suggested that SPhP could lead to efficient heat conduction with the long-range guided modes in the forms of thin films [160,214], two-dimensional pores [215], and nanowires [213]. Experimentally, however, there has been no direct measurement unambiguously showing the thermal conductivity contributed by SPhPs.

7.2   Experimental Designs for Heat Transfer Measurement

To experimentally investigate the heat transport by SPhPs, distinct thermal conductance by SPhPs (G_{SPhP}) needs to be designed compared to the contributions from other heat conducting routes, such as phononic conduction in a solid (G_{Phonon}) and grey body radiation (G_{Rad}) out of the surface. We estimated the conductance by each mechanism separately, using the following equations.

$$G_{Phonon} = \kappa \frac{A_c}{L} \tag{7.1}$$

$$G_{Rad} = 4\varepsilon\sigma A T^3 \tag{7.2}$$

$$G_{SPhP,0} = G_0 = \frac{\pi^2 k_B^2 T}{3h} \tag{7.3}$$

where κ is the phononic thermal conductivity, A_c is the cross-sectional area, L is the length, ε is the emissivity, σ is the Stefan-Boltzmann constant, A is the surface area, T is the temperature, k_B is the Boltzmann constant and h is the Planck constant. It should be noted that the G_{SPhP} has not been observed experimentally and thus we used G_0 (in Eq. (7.3)) to design the suitable L to observe the contributions of G_{SPhP} in heat conduction. Here, G_0 is the quantum conductance per mode. Theoretical studies have shown long mean free paths (Λ) of SPhPs[160,214], as shown in Fig. 7.2. With $L \ll \Lambda$, the heat transport by SPhPs is in the ballistic regime. Therefore, we used G_0 as the maximum limit per mode under the ballistic transport condition. In reality, G_{SPhP} might support multiple higher order modes which depend on polarization of electromagnetic waves. In addition, each mode may lead to a conductance less than G_0 due to various loss mechanisms. Understanding the length-dependent behaviors of different heat transport mechanism is an important factor to be considered to design the SPhP waveguide. Here, we fixed the width and thickness as 250 nm and 50 nm, respectively, and varied the length. The controlled length shows a window to observe dominant contributions by SPhPs, as seen in Fig. 7.1.

Based on this estimation (Fig. 7.1), we fabricated high-aspect-ratio SiO_2 nanowires with narrow cross-section (50 nm and 250 nm in thickness and width, respectively) and variable L, ranging from 50 to 300 μm. To eliminate the potential impact of thermal contact resistance between the nanowire and the thermal reservoirs, the nanowires were monolithically integrated with the thermal reservoirs (made of large SiO_2 beams covered with metal layers) (Fig.7.2). The SiO_2 nanowires were fabricated from an e-beam lithography (EBL) process that defined nanowires from a 50-nm thermal oxide layer on a Si wafer. Metal beams and electrodes (10 nm Ti/ 70 nm Pt) were patterned using photolithography, followed

by dry reactive ion etching (RIE) of the SiO$_2$ layer and eventually the release of the entire

suspended structure (nanowire and the beams) using XeF$_2$ dry etching. We were able to

fabricate devices with 250 nm in the width, and 50 μm to 300 μm in the length.
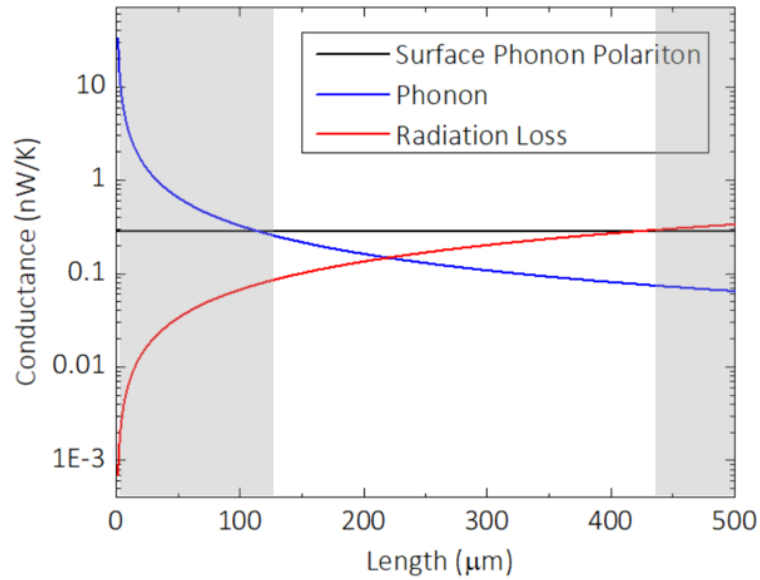
Figure 7.1   Plots of thermal conductance by SPhPs, phononic conduction and radiation as a function of the sample length. Width and thickness are constant (e.g., 250 nm and 50 nm, respectively).
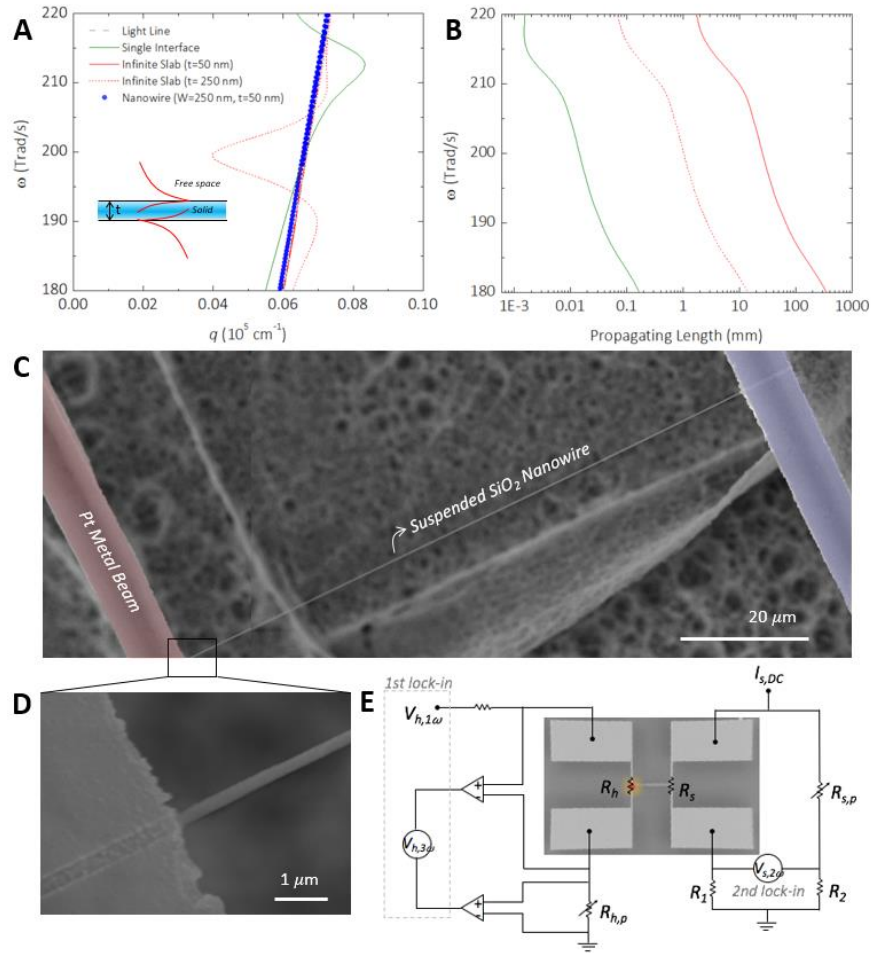
Figure 7.2   (A) Dispersion relation of SPhP by infinite slabs (thin films) of different thickness and a nanowire. (B) SPhP propagating length for different thickness of infinite slabs, corresponding to the dispersion curves in (A). (C) SEM image of the device showing a suspended SiO$_2$ nanowire integrated with the heating and sensing electrodes, and zoomed-in image in (D). (E) AC modulated heating scheme.

Since the nanowires are designed to be very long (over 50 μm) to suppress the phonon conductance, the total thermal conductance will be small, about 0.1-1 nW/K at 300 K. We have devised a highly sensitive thermometry and calorimetry technique to measure such a small thermal conductance, as demonstrated in our earlier publications.[216-218] Briefly, as

shown in Fig. 7.2(E), an AC current at frequency 1ω is applied to one of the metal beams (heating beam), which induces a heat current at 2ω *via* Joule heating. The small portion of this heat current is conducted along the nanowire (by both SPhP and phonon conduction contributions) and raise the temperature of the other beam (sensing beam). By using lock-ins to measure the temperature rises at 3ω and 2ω for the heating and sensing beams respectively (through monitoring the resistance changes of the metal beams), we can obtain the thermal conductance of the nanowires. The high sensitivity is enabled by two features: (1) the long and suspended beams (SiO$_2$+Ti/Pt) provides good thermal insulation with a thermal conductance of ~300 nW/K, which can lead to an appreciable temperature rise (>3 mK) on the sensing beam even for a very small nanowire conductance (e.g., 0.1. nW/K), if the heating beam is heated up by ~10 K; (2) the heating flux is modulated at 2ω and the thermometry on the sensing beam is performed using the lock-in technique, which greatly improves the thermometry and calorimetry sensitivity (<0.1 mK and ~pW/K).

7.3   Results and Discussion

7.3.1   Enhanced Absorption Cross-Section

The metallic surface of polar dielectrics in the Reststrahlen band reflects IR waves at the surface. It makes larger spatial distribution of SPhP energy in the free space (Fig. 7.2(A) inset), rather than in the solid. Further, an antisymmetric configuration of electric fields at the two top and bottom surfaces in a thin slab makes negligible contributions in solid. Therefore, it prevents the energy penetration into the lossy solid, and results in light-like

dispersion of the surface modes with a long Λ (Fig. 7.2(B)). This dispersion points to the possibility of ballistic heat transport.

A suspended single nanowire with high aspect ratios assures strong directionality of thermal emission along the nanowire length direction. Owing to the nature of radiation, the spatial energy distribution would not be restricted by the physical cross-sections of the tiny nanowire, but rather it is guided by the polar dielectric nanowire, analogous to light guided through an optical fiber. Especially, when the dimension becomes comparable to or smaller than the thermal wavelength, λ_T (~10 µm at 300 K), the actual across section for energy transport will extend into the free space with the length scale of λ_T, which could be much larger than the physical diameter of the nanowire. Figure 7.3 shows the cross-section enhancement factor by normalizing the extinction cross-section (σ_{ext}) with the geometrical cross-section (σ_{geom}), or $\sigma_{ext}/\sigma_{geom}$. The σ_{ext} was determined using COMSOL, by considering both absorption and scattering cross-sections. Our fabricated nanowires consist of two different cross-section dimensions, 250 nm in width and 50 nm in thickness. Therefore, we conducted two separate 2D modeling with a plane wave. As we aim to characterize the surface modes in a plane, the 2D models can provide insight to analyze spectral and length-dependent behaviors. The cross-section enhancement factors for nanowires of 300 µm length are summarized in Figs. 7.3 (A,B) for σ_{geom} of 250 nm and 50 nm, respectively. The spectral σ_{ext} has the maximum peak within the Reststrahlen band. The enhancement factor over 300 in both 250 nm and 50 nm cross-sections can be further increased with the longer lengths as shown in Figs. 7.3(c,d). It indeed confirms that the surface modes have much longer Λ than 300 µm as the enhancement factor was not saturated even with the length of 500 µm.

Importantly, the giant enhancement proved that the surface wave can carry highly confined

energy, and the picture is similar to an optical antenna.
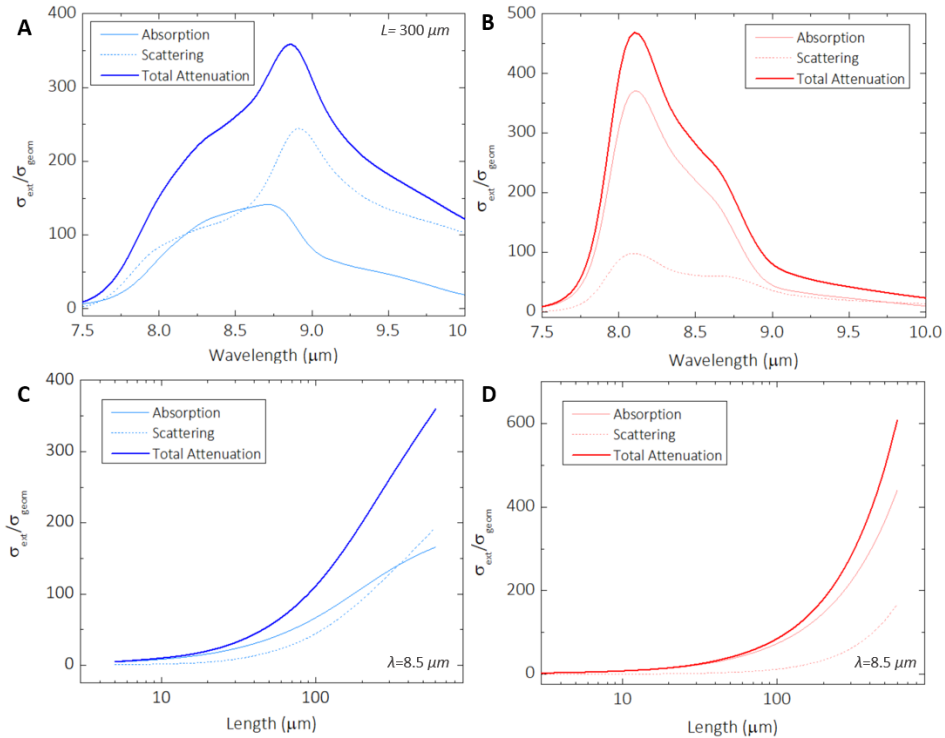
Figure 7.3   Plots of 2D modeled enhancement factor of cross-section, defined as the ratio between the extinction cross-section σ_{ext} and the geometrical cross-section , σ_{geom}, as a function of wavelength for a 300 μm long sample for (A) σ_{geom} =250 nm, (B) σ_{geom}=50 nm. Enhancement factor as a function of L for (C) σ_{geom}=250 nm and (D) σ_{geom}=50 nm at wavelength $\lambda = 8.5 \ \mu m$.

Next, we seek to understand the length-dependent behavior of the absorbed power.

For ballistic transport with G_0, it is necessary to achieve perfect transmission of the thermal

energy from the heater to the sensor. On the other hand, a Λ much shorter than the sample

length would result in diffusive transport. As shown in Fig. 7.4, we modeled the absorption

power normalized by the incident power with various lengths. The height of the unit cell for modeling was fixed with 50 µm. Similar to the calculation in Fig. 7.3, we conducted 2D modeling but the geometry of heating and sensing beams was also considered as indicated in insets of Fig. 7.4(A) and (B). We compared three different cases, including bulk, nanowire and empty channel bridging the heater and sensor. The normalized power ($P = P_{abs}/P_{in}$) from the numerical modeling was compared to the analytical estimation using Eqs. (7.4) and (7.5).

$$P_{abs} = P_{in}(1 - e^{-kL})$$ (7.4)

$$k = \frac{1}{2\Lambda}$$ (7.5)

where P_{abs} is the absorbed power, P_{in} is the incident power, and k is the damping constant. In the calculation, 8.5 µm wavelength was used for all the cases. To quantify the Λ, our numerical modeling calculated absorption in medium only for bulk and nanowire cases. For the empty medium, we included absorption in the beam and we shall discuss it later by comparing far-field radiation with a vacuum gap and with a guided mode. The increasing rate of P with longer lengths is weighted by Λ. By comparing the numerical and analytical models, it is found that the Λ for bulk and 250 nm cross-section nanowire is 0.83 and 200 µm, respectively, and the Λ for 50 nm cross-section nanowire (Fig. 7.4 (B)) is in the range of 625 to 833 µm. It implies that a thinner structure would be closer to the ballistic regime.
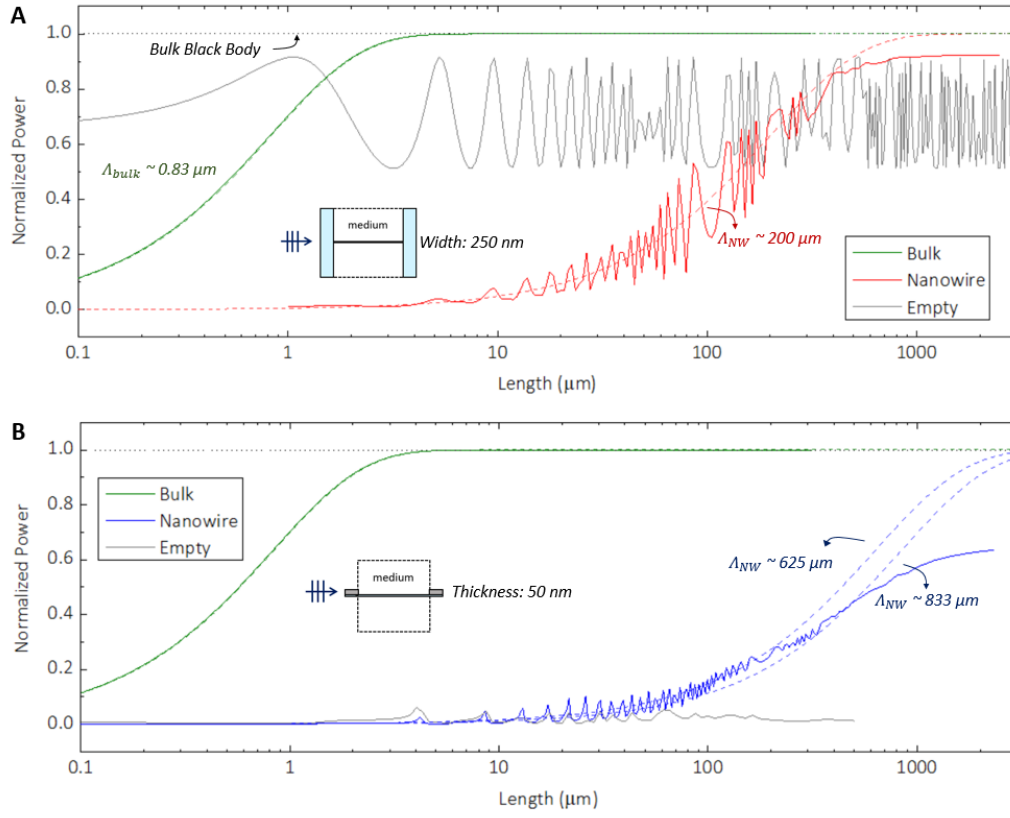
Figure 7.4   Length-dependent power absorption with 250 nm (A) and 50 nm (B) in the cross-section by 2D COMSOL modeling.

To detect polaritonic heat transport using the thermometer, the propagating energy needs to be absorbed while the carriers possess the long Λ. The best scenario to observe ballistic transport would be no absorption within the medium but perfect absorption at the sensor. It describes far-field radiation with the vacuum gap, integrated with a blackbody receiver. However, the receiver needs to be massive to collect the radiating wave from all directions. The modeling results with an empty medium in Figs. 7.4(A) and 7.4(B) clearly shows different absorption efficiency with different geometry of beams. In Fig. 7.4(A), the incident wave propagates on the plane, parallel to the top vies of the suspended device.

Therefore, the long beam length of 240 μm ensures the incoming wave absorbed in the beam. On the other hand, when the wave propagates in the plane parallel to the side view of the suspended device, the majority area consists of free space due to the thin structure, resulting in high transmission. In this study, a nanowire with a long Λ is integrated. With $L \ll \Lambda$, the nanowire involves negligible absorption, thus the detected heat flux at the sensor would be identical to the case of far-field radiation in free-space. However, as the L increases, it starts to have absorption but as the L is not long enough to be considered with Rosseland approximation which assumes a perfect absorber to contribute the power to diffusive heat transport[214]. Hence, we can expect our experimental observation with the designed L (50 to 300 μm) is in the quasi-ballistic regime by SPhPs.

More importantly, the absorbed power by a nanowire can be as significant as bulk. For instance, the nanowire with 50 nm cross-section and 100 μm length can absorb ~20% of a blackbody with 50 μm thickness. It indicates a giant absorption cross-section enhancement factor, and is consistent with what we observed in Fig. 7.3, where the SiO_2 nanowire has much longer Λ than the bulk (e.g., ~833 and ~0.83 μm for the nanowire and the bulk, respectively). Strictly speaking, with the picture of quasi-ballistic transport with the surface modes, we cannot categorize its physical picture to either far-field radiation or conduction separately, but rather should consider it as the hybridized modes, precisely the name of surface phonon polariton suggests! On one hand, it is non-classical heat conduction which can carry the energy beyond the physical cross-section. On the other hand, it is directional far-field radiation with a solid medium to guide the electromagnetic surface wave.

7.3.2 Length-dependent Thermal Conductivity
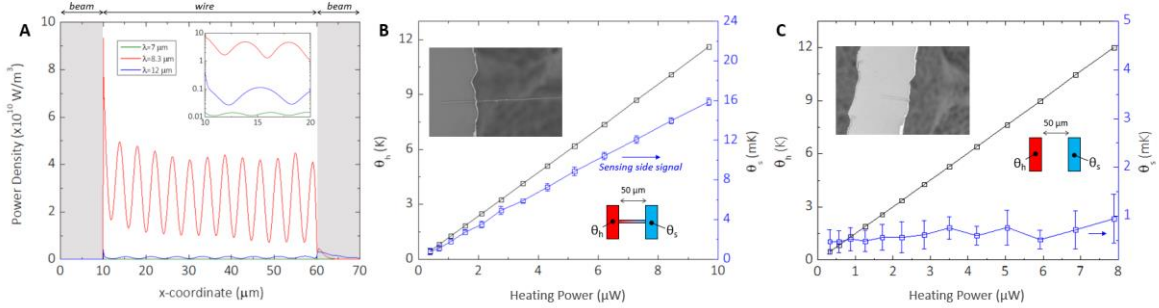
Figure 7.5   (A) Modeled absorbed power density with various wavelength. Measured temperature rises as a function of heating power with (B) and without (C) a nanowire.

The existence of a guided heat channel makes significant energy transport. The enhancement is distinguishable with the energy within the Reststrahlen band (Fig. 7.5(A)). As mentioned before, without designing a highly absorbing sensor, we would not be able to detect high heat flux because the majority of the energy goes through the suspended thin beam. To quantify the contribution from the far-field, we measured temperature rises at heating and sensing sides with a nanowire, and re-measured the identical sample after we removed the nanowire. As shown in Figs. 7.5(B,C), we heated up one side of the metal beam by Joule heating with the power up to ~10 µW. It resulted in the temperature rise at the heating side up to 12 K. The heating conditions were the same in two separate measurements with and without the nanowire. While the nanowire could transport the heat from the heater to sensor and increase the sensing side temperature up to 16 mK, the sensing side temperature without the nanowire did not increase. It indicates that the sole far-field radiation through the vacuum gap is negligible without the aid of the nanowire in our device.

166
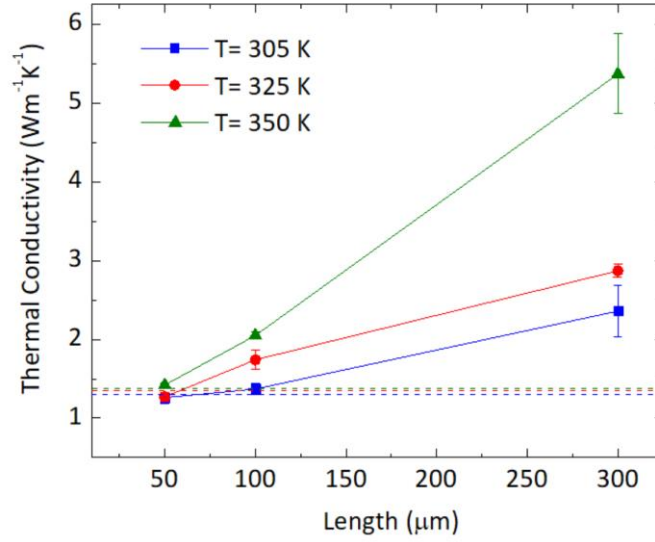
Figure 7.6   Length-dependent thermal conductivity at various temperatures.

Furthermore, we can determine the effective length-dependent thermal conductivity κ, which can be attributed to classical phonons in solid and the SPhP modes:

$$\kappa = \left(G_{Phonon} + G_{SPhP}\right)\frac{L}{A} = \kappa_{Phonon} + \kappa_{SPhP} \qquad (7.6)$$

The κ_{Phonon} and κ_{SPhP} have different length-dependent behaviors. With Λ of ~1 nm for phonons in SiO_2,[188,219] phononic conduction is diffusive in the fabricated nanowires that are longer than 50 µm. It has been shown that κ of nanostructured SiO_2 with dimensions even down to 7 nm follows the bulk κ.[178] Thus, κ_{Phonon} is independent on the length. The κ_{Phonon} is indicated in Fig. 7.6 with dash lines using the bulk SiO_2 thermal conductivity.

The length-dependent plot can distinguish ballistic and diffusive transport mechanisms. By comparing the measured κ and κ_{Phonon}, we could extract the κ_{SPhP}. With $L=50$ µm, the measured total κ is close to κ_{Phonon}. The lack of absorption in the nanowire led to little

energy collection in the sensing beam. However, the contributions by SPhPs became apparent with the increasing L. We could observe total κ of 2.36 ($\pm$0.329) W/m-K with 300 μm at 305 K. Furthermore, we measured κ at higher temperatures up to 350 K, and interestingly the κ increased further up to 5.37 ($\pm$0.508) W/m-K. It shows that heat conduction by SPhPs is fundamentally radiation in nature, as expected. It is important in that the quasi-ballistic transport by polaritons can be used at room temperature and even the mechanism becomes stronger at higher temperature due to the radiative nature, while ballistic features by other carriers such as phonons and electrons tend to be diminished at higher temperature.

7.4   Conclusions

In this Chapter, we investigated coupled heat radiation and conduction by SPhPs. Highly anisotropic nanowire designs with high aspect ratios (length:diameter >1000:1) was chosen to ensure the dominant heat conduction via the surface mode, relative to solid heat conduction and radiation heat loss. Asymmetric configuration of electric fields at the top and bottom surfaces of a nanowire with a thickness smaller than the λ_T resulted in the long Λ. In addition, the giant enhancement factor in the absorption-cross section allows high heat flux by the small nanowires. Our heat transfer experiment combined with 2D optical modeling revealed the importance of an efficient absorber as well as long Λ to thermally detect the surface wave in the sensor beam. We measured the effective κ of SiO_2 nanowires with various lengths. With the quasi-ballistic transport picture, the highest κ of 5.37 W/m-K was observed with the longest length (300 μm) at 350 K. Heat conduction by SPhPs could be understood

with the optical transport behavior. It clearly showed that the polaritonic conduction does not have an apparent boundary of radiation and conduction. Due to the radiative behavior, the polaritonic contribution showed distinctly different feature compared to phonon heat conduction: first, it increased at higher temperatures due to the radiative nature; second, the effective thermal conductivity is quasi-ballistic, or increases with length. The experimental observations suggest a new heat transport mechanism by surface phonon polaritons.

Acknowledgements

Chapter 8

Conclusions and Future Work

Active control of thermal transport is of significant interest for a wide-range of applications, such as thermoregulation (for individuals, buildings, vehicles, batteries, and so on), energy conversion, bio/chemical sensing, and micro/nanomanufacturing. However, the diffusive nature of heat conduction, which is caused by the incoherence of heat carriers (phonons and electrons), hinders excellent controllability. This dissertation showed experimental investigations of efficient energy converters using thermo-electric engineering and a novel heat transport by polaritons using thermo-photonic engineering. The interdisciplinary approach can be further extended, such as thermo-mechanical engineering, as well as thermo-electric and thermo-photonic engineering with nanotechnology. In the following paragraphs, I elaborate three examples of future research directions.

The ongoing effort to reduce the energy conception of climate control systems has mainly focused on the development of more efficient thermoregulation technologies. Typically, cooling and heating represents the biggest part of building energy consumption. Along the fact that traditional approaches to air conditioning the entire buildings waste substantial amount of energy, interests in personalized thermoregulation devices have been growing. It can deliver a precise thermal dose to the target spots on individual and consequently reduce the cooling volume drastically. It also can be applied to enhance personal thermal comfort for outdoor activities and health care.

In particular, TE devices are attractive for the personalized object as they are solid state with small form factors and the cooling power can be easily adjusted. However, the development of wearable cooling devices is far more challenging and largely unexplored, compared to rigid TE generators. High-performance cooling devices still require high ZT at the material-level and also advanced thermal designs for effective heat dissipation in device-level studies. A key challenge is how to adapt the thermal designs into wearable forms. The demonstration of high-performance wearable thermo-regulators at device-level can be conducted, combined with the high-performance printable TE materials on flexible fabrics developed in this dissertation work.

This dissertation work on heat transfer by SPhPs has demonstrated the promise of coherent heat transport which improves the controllability of thermal engineering. The conducted experimental efforts with an ordinary materials, i.e., glass (amorphous SiO_2), showed the feasibility of coherent, directional, and ballistic polaritonic heat conduction, beyond the classical regime of diffusive heat conduction, using the novel measurement platform. Built upon these encouraging results, extraordinary heat conduction phenomena can be further explored, which also can be used for novel thermal management devices. Specifically, systematic study of polaritonic heat conduction should be conducted in rationally designed nanostructures of various polar materials, such as SiO_2, SiC and a wide range of 2D materials (i.e., hBN and graphene). Moreover, the phenomena in photonic metasurfaces can be used to provide another degree of freedom to tailor the photonic density of states. In particular, the existence of SPhPs can be controlled by modulating the optical property of the surrounding or heat carrying channel itself, so as to tune the thermal transport, which is otherwise very difficult, if not impossible, to achieve in the diffusive thermal

171

transport paradigm. More interestingly, heat transfer mediated by SPhP is expected to be more important at high temperature, similar to radiative heat transfer. Therefore, the polaritonic thermal transport phenomena could be used for thermal management of a wide range of high-temperature electronic devices such as laser diode, light emitting diodes (LEDs), and high-power inverters, which are increasingly more widely used in many industries such as defense, aerospace, and energy.

In a different class of materials compared to polar inorganic materials, nanostructures of soft materials with tunable thermomechanical properties can be studied. Tremendous interests in the use of soft materials have led to wide-range applications in wearable devices, soft robotics, artificial skins using elastomers, etc. In particular, heat-involving phase transition of polymers at relatively low temperatures has attracted applications in actuators, thermal switches, and desalinations by yielding morphological changes. Yet, the thermo-responsive study in nanostructures is still at the nascent stage due to the lack of advanced characterization tools to elucidate the thermo-mechanical mechanisms at micro/nanoscales. By adopting and developing the thermometry used for single nanowires, dynamic thermal actuation of polymer nanofibers and thin films upon structural phase transition can be studied and measured through the accompanied thermal property changes. Especially, this work can reveal significant contributions to the research field of bio-mimicking artificial muscle fibers, as well as broader impacts to the study on thermo-responsive soft materials by providing a quantitative measurement platform to study the thermodynamics and thermomechanical coupling at nanometer scale.

Reference

1   Malen, J. A., Yee, S. K., Majumdar, A. & Segalman, R. A. Fundamentals of energy transport, energy conversion, and thermal properties in organic-inorganic heterojunctions. *Chem Phys Lett* **491**, 109-122 (2010).

2   Yee, S. K., Coates, N. E., Majumdar, A., Urban, J. J. & Segalman, R. A. Thermoelectric power factor optimization in PEDOT:PSS tellurium nanowire hybrid composites. *Phys Chem Chem Phys* **15**, 4024-4032 (2013).

3   Wan, C. L. *et al.* Flexible n-type thermoelectric materials by organic intercalation of layered transition metal dichalcogenide TiS_2. *Nat Mater* **14**, 622-627 (2015).

4   Oh, J. Y. *et al.* Effect of PEDOT Nanofibril Networks on the Conductivity, Flexibility, and Coatability of PEDOT:PSS Films. *Acs Appl Mater Inter* **6**, 6954-6961 (2014).

5   Sanchez, C. *et al.* Designed hybrid organic-inorganic nanocomposites from functional nanobuilding blocks. *Chem Mater* **13**, 3061-3083 (2001).

6   Bahk, J. H., Fang, H. Y., Yazawa, K. & Shakouri, A. Flexible thermoelectric materials and device optimization for wearable energy harvesting. *J Mater Chem C* **3**, 10362-10374 (2015).

7   Kim, S. J., We, J. H. & Cho, B. J. A wearable thermoelectric generator fabricated on a glass fabric. *Energ Environ Sci* **7**, 1959-1965 (2014).

8   Wang, Y., Zhang, S. M. & Deng, Y. Flexible low-grade energy utilization devices based on high-performance thermoelectric polyaniline/tellurium nanorod hybrid films. *J Mater Chem A* **4**, 3554-3559 (2016).

9   Yang, Y., Xie, S. H., Ma, F. Y. & Li, J. Y. On the effective thermoelectric properties of layered heterogeneous medium. *J Appl Phys* **111** (2012).

10   Park, G. O. *et al.* Enhanced thermoelectric properties of germanium powder/poly(3,4-ethylenedioxythiophene):poly(4-styrenesulfonate) composites. *Thin Solid Films* **566**, 14-18 (2014).

11   Song, H. J. *et al.* Improved Thermoelectric Performance of Free-Standing PEDOT:PSS/Bi_2Te_3 Films with Low Thermal Conductivity. *J Electron Mater* **42**, 1268-1274 (2013).

12   Wang, Y. Y., Cai, K. F. & Yao, X. Facile Fabrication and Thermoelectric Properties of PbTe-Modified Poly(3,4-ethylenedioxythiophene) Nanotubes. *Acs Appl Mater Inter* **3**, 1163-1166 (2011).

13   Bubnova, O. *et al.* Optimization of the thermoelectric figure of merit in the conducting polymer poly(3,4-ethylenedioxythiophene). *Nat Mater* **10**, 429-433 (2011).

14   Lim, H. C. *et al.* Self-Assembled Poly(3,4-ethylene dioxythiophene):Poly(styrenesulfonate)/Graphene Quantum Dot Organogels for Efficient Charge Transport in Photovoltaic Devices. *Acs Appl Mater Inter* **7**, 11069-11073 (2015).

15   Hull, D. & Clyne, T. *An introduction to composite materials*.   (Cambridge university press, 1996).

16   Laine, R. M., Choi, J. W. & Lee, I. Organic-inorganic nanocomposites with completely defined interfacial interactions. *Adv Mater* **13**, 800-803 (2001).

17   Coates, N. E. *et al.* Effect of Interfacial Properties on Polymer-Nanocrystal Thermoelectric Transport. *Adv Mater* **25**, 1629-1633 (2013).

18   Xu, N., Xu, Y. & Zhu, J. Topological insulators for thermoelectrics. *Npj Quantum Mater* **2** (2017).

19   Bergman, D. J. & Fel, L. G. Enhancement of thermoelectric power factor in composite thermoelectrics. *J Appl Phys* **85**, 8205-8216 (1999).

20   Wang, Y. X., Xu, N., Li, D. Y. & Zhu, J. Thermal Properties of Two Dimensional Layered Materials. *Adv Funct Mater* **27** (2017).

21   Dresselhaus, M. S. *et al.* New directions for low-dimensional thermoelectric materials. *Adv Mater* **19**, 1043-1053 (2007).

22   Zhang, T. *et al.* Mechanically Durable and Flexible Thermoelectric Films from PEDOT:PSS/PVA/Bi0.5Sb1.5Te3 Nanocomposites. *Adv Electron Mater* **3**, 160054 (2017).

23   Ko, J. *et al.* Nanograined thermoelectric Bi2Te2.7Se0.3 with ultralow phonon transport prepared from chemically exfoliated nanoplatelets. *J Mater Chem A* **1**, 12791-12796 (2013).

24   Cahill, D. G. *et al.* Nanoscale thermal transport. II. 2003-2012. *Appl Phys Rev* **1**, 011305 (2014).

25   Xu, K. L., Chen, G. M. & Qiu, D. Convenient construction of poly(3,4-ethylenedioxythiophene)-graphene pie-like structure with enhanced thermoelectric performance. *J Mater Chem A* **1**, 12395-12399 (2013).

26   Wang, L. M. *et al.* Large thermoelectric power factor in polyaniline/graphene nanocomposite films prepared by solution-assistant dispersing method. *J Mater Chem A* **2**, 11107-11113 (2014).

27   Zhang, B., Sun, J., Katz, H. E., Fang, F. & Opila, R. L. Promising Thermoelectric Properties of Commercial PEDOT:PSS Materials and Their Bi2Te3 Powder Composites. *Acs Appl Mater Inter* **2**, 3170-3178 (2010).

28   Du, Y., Cai, K. F., Chen, S., Cizek, P. & Lin, T. Facile Preparation and Thermoelectric Properties of Bi2Te3 Based Alloy Nanosheet/PEDOT:PSS Composite Films. *Acs Appl Mater Inter* **6**, 5735-5743 (2014).

29   Liu, Y. *et al.* Preparation of bulk AgNWs/PEDOT:PSS composites: a new model towards high-performance bulk organic thermoelectric materials. *Rsc Adv* **5**, 45106-45112 (2015).

30   Culebras, M., Garcia-Barbera, A., Serrano-Claumarchirant, J. F., Gomez, C. M. & Cantarero, A. Hybrids composites of NCCO/PEDOT for thermoelectric applications. *Synthetic Met* **225**, 103-107 (2017).

31   Yoshida, A. & Toshima, N. Thermoelectric Properties of Hybrid Thin Films of PEDOT-PSS and Silver Nanowires. *J Electron Mater* **45**, 2914-2919 (2016).

32   Koch, N. *et al.* Conjugated organic molecules on metal versus polymer electrodes: Demonstration of a key energy level alignment mechanism. *Appl Phys Lett* **82**, 70-72 (2003).

33   Haneman, D. Photoelectric Emission and Work Functions of Insb, Gaas, Bi2te3 and Germanium. *J Phys Chem Solids* **11**, 205-214 (1959).

34   Crispin, X. *et al.* The origin of the high conductivity of poly(3,4-ethylenedioxythiophene)-poly(styrenesulfonate) (PEDOT- PSS) plastic electrodes. *Chem Mater* **18**, 4354-4360 (2006).

35   Nardes, A. M., Janssen, R. A. J. & Kemerink, M. A morphological model for the solvent-enhanced conductivity of PEDOT : PSS thin films. *Adv Funct Mater* **18**, 865-871 (2008).

36   Crispin, X. *et al.* Conductivity, morphology, interfacial chemistry, and stability of poly(3,4-ethylene dioxythiophene)-poly(styrene sulfonate): A photoelectron spectroscopy study. *J Polym Sci Pol Phys* **41**, 2561-2583 (2003).

37   Kim, G. H., Shao, L., Zhang, K. & Pipe, K. P. Engineered doping of organic semiconductors for enhanced thermoelectric efficiency. *Nat Mater* **12**, 719-723 (2013).

38   Gasiorowski, J., Menon, R., Hingerl, K., Dachev, M. & Sariciftci, N. S. Surface morphology, optical properties and conductivity changes of poly(3,4-ethylenedioxythiophene): poly(styrenesulfonate) by using additives. *Thin Solid Films* **536**, 211-215 (2013).

39   Takano, T., Masunaga, H., Fujiwara, A., Okuzaki, H. & Sasaki, T. PEDOT Nanocrystal in Highly Conductive PEDOT:PSS Polymer Films. *Macromolecules* **45**, 3859-3865 (2012).

40   Kim, J. Y., Jung, J. H., Lee, D. E. & Joo, J. Enhancement of electrical conductivity of poly(3,4-ethylenedioxythiophene)/poly(4-styrenesulfonate) by a change of solvents. *Synthetic Met* **126**, 311-316 (2002).

41   Nguyen, P. K. *et al.* Spark erosion: a high production rate method for producing Bi0.5Sb1.5Te3 nanoparticles with enhanced thermoelectric performance. *Nanotechnology* **23**, 415604 (2012).

42   Shin, S. *et al.* High-Performance Screen-Printed Thermoelectric Films on Fabrics. *Sci Rep-Uk* **7** (2017).

43   Israelachvili, J. N. *Intermolecular and surface forces*.   (Academic press, 2011).

44   Nakama, T., Burkov, A. T., Heinrich, A., Oyoshi, T. & Yagasaki, K. Experimental set-up for thermopower and resistivity measurements at 100-1300 K. *Xvii International Conference on Thermoelectrics, Proceedings Ict 98*, 266-269 (1998).

45   Pettes, M. T., Maassen, J., Jo, I., Lundstrom, M. S. & Shi, L. Effects of Surface Band Bending and Scattering on Thermoelectric Transport in Suspended Bismuth Telluride Nanoplates. *Nano Lett* **13**, 5316-5322 (2013).

46   Chen, C. Y. *et al.* Robustness of topological order and formation of quantum well states in topological insulators exposed to ambient environment. *P Natl Acad Sci USA* **109**, 3694-3698 (2012).

47   Ouyang, L. Q., Musumeci, C., Jafari, M. J., Ederth, T. & Inganas, O. Imaging the Phase Separation Between PEDOT and Polyelectrolytes During Processing of Highly Conductive PEDOT:PSS Films. *Acs Appl Mater Inter* **7**, 19764-19773 (2015).

48   Yunker, P. J., Still, T., Lohr, M. A. & Yodh, A. G. Suppression of the coffee-ring effect by shape-dependent capillary interactions. *Nature* **476**, 308-311 (2011).

49   Bulman, G. *et al.* Superlattice-based thin-film thermoelectric modules with high cooling fluxes. *Nat Commun* **7** (2016).

50   Majumdar, A. THERMOELECTRIC DEVICES Helping chips to keep their cool. *Nat Nanotechnol* **4**, 214-215 (2009).

51   Zhao, L. D. *et al.* Ultralow thermal conductivity and high thermoelectric figure of merit in SnSe crystals. *Nature* **508**, 373 (2014).

52   Rhyee, J. S. *et al.* Peierls distortion as a route to high thermoelectric performance in In4Se3-delta crystals. *Nature* **459**, 965-968 (2009).

53   Hochbaum, A. I. *et al.* Enhanced thermoelectric performance of rough silicon nanowires. *Nature* **451**, 163-168 (2008).

54   Boukai, A. I. *et al.* Silicon nanowires as efficient thermoelectric materials. *Nature* **451**, 168-171 (2008).

55   Venkatasubramanian, R., Siivola, E., Colpitts, T. & O'Quinn, B. Thin-film thermoelectric devices with high room-temperature figures of merit. *Nature* **413**, 597-602 (2001).

56   Snyder, G. J. & Toberer, E. S. Complex thermoelectric materials. *Nat Mater* **7**, 105-114 (2008).

57   Zhao, L. D. *et al.* Ultrahigh power factor and thermoelectric performance in hole-doped single-crystal SnSe. *Science* **351**, 141-144 (2016).

58   Bell, L. E. Cooling, heating, generating power, and recovering waste heat with thermoelectric systems. *Science* **321**, 1457-1461 (2008).

59   Poudel, B. *et al.* High-thermoelectric performance of nanostructured bismuth antimony telluride bulk alloys. *Science* **320**, 634-638 (2008).

60   Du, Y. *et al.* Thermoelectric Fabrics: Toward Power Generating Clothing. *Sci Rep-Uk* **5** (2015).

61   Bahk, J.-H., Fang, H., Yazawa, K. & Shakouri, A. Flexible thermoelectric materials and device optimization for wearable energy harvesting. *Journal of Materials Chemistry C* **3**, 10362-10374 (2015).

62   Kim, J., Kumar, R., Bandodkar, A. J. & Wang, J. Advanced Materials for Printed Wearable Electrochemical Devices: A Review. *Advanced Electronic Materials* **3**, 1600260 (2017).

63   See, K. C. *et al.* Water-Processable Polymer-Nanocrystal Hybrids for Thermoelectrics. *Nano Lett* **10**, 4664-4667 (2010).

64   Kim, M. K., Kim, M. S., Lee, S., Kim, C. & Kim, Y. J. Wearable thermoelectric generator for harvesting human body heat energy. *Smart Mater Struct* **23** (2014).

65   Madan, D., Wang, Z. Q., Wright, P. K. & Evans, J. W. Printed flexible thermoelectric generators for use on low levels of waste heat. *Appl Energ* **156**, 587-592 (2015).

66   Madan, D., Wang, Z. Q., Chen, A., Wright, P. K. & Evans, J. W. High-Performance Dispenser Printed MA p-Type Bi0.5Sb1.5Te3 Flexible Thermoelectric Generators for Powering Wireless Sensor Networks. *Acs Appl Mater Inter* **5**, 11872-11876 (2013).

67   Wang, Z. *et al.* Integration of dispenser-printed ultra-low-voltage thermoelectric and energy storage devices. *J Micromech Microeng* **22** (2012).

68   Chen, A., Madan, D., Wright, P. K. & Evans, J. W. Dispenser-printed planar thick-film thermoelectric energy generators. *J Micromech Microeng* **21** (2011).

69   Madan, D., Chen, A., Wright, P. K. & Evans, J. W. Dispenser printed composite thermoelectric thick films for thermoelectric generator applications. *J Appl Phys* **109** (2011).

70   Madan, D., Chen, A., Wright, P. K. & Evans, J. W. Printed Se-Doped MA n-Type Bi2Te3 Thick-Film Thermoelectric Generators. *J Electron Mater* **41**, 1481-1486 (2012).

71   Madan, D. *et al.* Enhanced Performance of Dispenser Printed MA n-type Bi2Te3 Composite Thermoelectric Generators. *Acs Appl Mater Inter* **4**, 6117-6124 (2012).

72   Madan, D. *et al.* Dispenser printed circular thermoelectric devices using Bi and Bi0.5Sb1.5Te3. *Appl Phys Lett* **104** (2014).

73   Lu, Z. Y. *et al.* Fabrication of Flexible Thermoelectric Thin Film Devices by Inkjet Printing. *Small* **10**, 3551-3554 (2014).

74   Navone, C., Soulier, M., Plissonnier, M. & Seiler, A. L. Development of (Bi,Sb)(2)(Te,Se)(3)-Based Thermoelectric Modules by a Screen-Printing Process. *J Electron Mater* **39**, 1755-1759 (2010).

75   Navone, C., Soulier, M., Testard, J., Simon, J. & Caroff, T. Optimization and Fabrication of a Thick Printed Thermoelectric Device. *J Electron Mater* **40**, 789-793 (2011).

76   Varghese, T. *et al.* High-performance and flexible thermoelectric films by screen printing solution-processed nanoplate crystals. *Sci Rep-Uk* **6** (2016).

77   We, J. H., Kim, S. J., Kim, G. S. & Cho, B. J. Improvement of thermoelectric properties of screen-printed Bi2Te3 thick film by optimization of the annealing process. *J Alloy Compd* **552**, 107-110 (2013).

78   Kim, S. J., We, J. H., Kim, J. S., Kim, G. S. & Cho, B. J. Thermoelectric properties of P-type Sb2Te3 thick film processed by a screen-printing technique and a subsequent annealing process. *J Alloy Compd* **582**, 177-180 (2014).

79   Kato, K., Hagino, H. & Miyazaki, K. Fabrication of Bismuth Telluride Thermoelectric Films Containing Conductive Polymers Using a Printing Method. *J Electron Mater* **42**, 1313-1318 (2013).

80   Bae, E. J., Kang, Y. H., Jang, K. S. & Cho, S. Y. Enhancement of Thermoelectric Properties of PEDOT:PSS and Tellurium-PEDOT:PSS Hybrid Composites by Simple Chemical Treatment. *Sci Rep-Uk* **6** (2016).

81   Lee, H. B. *et al.* Thermoelectric properties of screen-printed ZnSb film. *Thin Solid Films* **519**, 5441-5443 (2011).

82   Lee, H. B. *et al.* Thin-Film Thermoelectric Module for Power Generator Applications Using a Screen-Printing Method. *J Electron Mater* **40**, 615-619 (2011).

83   Hoong, L. J., Keat, Y. C., Chik, A. & Leng, T. P. Band structure and thermoelectric properties of inkjet printed ZnO and ZnFe2O4 thin films. *Ceram Int* **42**, 12064-12073 (2016).

84   Li, X. G., Huang, M. R. & Bai, H. Thermal decomposition of cellulose ethers. *J Appl Polym Sci* **73**, 2927-2936 (1999).

85   Nguyen, P. K. *et al.* Spark erosion: a high production rate method for producing Bi0.5Sb1.5Te3 nanoparticles with enhanced thermoelectric performance. *Nanotechnology* **23** (2012).

86   Moon, J. *et al.* High performance multi-scaled nanostructured spectrally selective coating for concentrating solar power. *Nano Energy* **8**, 238-246 (2014).

87   Cui, Z. & Cui, Z. in *Printed Electronics*   1-20 (John Wiley & Sons Singapore Pte. Ltd, 2016).

88   van der Pauw, L. J. A method of measuring specific resistivity and Hall effect of discs of arbitrary shape. *Philips Res. Rept.* **13**, 1 (1958).

89   van der Pauw, L. J. A method of measuring the resistivity and Hall coefficient on Lamellae of arbitrary shape. *Philips Res. Rept.* **13**, 220 (1959).

90   Zhu, Y. Heat-loss modified Angstrom method for simultaneous measurements of thermal diffusivity and conductivity of graphite sheets: The origins of heat loss in Angstrom method. *Int J Heat Mass Tran* **92**, 784-791 (2016).

91   Chen, X. *et al.* Thermal expansion coefficients of Bi2Se3 and Sb2Te3 crystals from 10 K to 270 K. *Appl Phys Lett* **99** (2011).

92   Cahill, D. G. Thermal-Conductivity Measurement from 30-K to 750-K - the 3-Omega Method. *Rev Sci Instrum* **61**, 802-808 (1990).

93   Bahmani, S. A., East, G. C. & Holme, I. The application of chitosan in pigment printing. *J Soc Dyers Colour* **116**, 94-99 (2000).

94   Wang, H. X., Guo, T. & Li, H. B. Evaluation of viscosity and printing quality of chitosan-based flexographic inks: The effect of chitosan molecular weight. *J Appl Polym Sci* **133** (2016).

95   Choi, P. S. R., Yuen, C. W. M., Ku, S. K. A. & Kan, C. W. Digital ink-jet printing for chitosan-treated cotton fabric. *Fiber Polym* **6**, 229-234 (2005).

96   Kangwansupamonkon, W., Suknithipol, M., Phattanarudee, S. & Kiatkamjornwong, S. Inkjet printing: effects of binder particle size and chitosan pretreatment on the qualities of silk fabric. *Surf Coat Int* **94**, 216-225 (2011).

97   Noppakundilograt, S., Buranagul, P., Graisuwan, W., Koopipat, C. & Kiatkamjornwong, S. Modified chitosan pretreatment of polyester fabric for printing by ink jet ink. *Carbohyd Polym* **82**, 1124-1135 (2010).

98   Dechaumphai, E. *et al.* Near-surface thermal characterization of plasma facing components using the 3-omega method. *J Nucl Mater* **455**, 56-60 (2014).

99   Dechaumphai, E. *et al.* Ultralow Thermal Conductivity of Multilayers with Highly Dissimilar Debye Temperatures. *Nano Lett* **14**, 2448-2455 (2014).

100   Kim, H. S., Gibbs, Z. M., Tang, Y. L., Wang, H. & Snyder, G. J. Characterization of Lorenz number with Seebeck coefficient measurement. *Apl Mater* **3** (2015).

101   Kim, W. *et al.* Thermal conductivity reduction and thermoelectric figure of merit increase by embedding nanoparticles in crystalline semiconductors. *Phys Rev Lett* **96** (2006).

102   Yu, B. *et al.* Enhancement of Thermoelectric Properties by Modulation-Doping in Silicon Germanium Alloy Nanocomposites. *Nano Lett* **12**, 2077-2082 (2012).

103   Sun, K. *et al.* Metasurface Optical Solar Reflectors Using AZO Transparent Conducting Oxides for Radiative Cooling of Spacecraft. *ACS Photonics* **5**, 495-501 (2018).

104   Kou, J.-l., Jurado, Z., Chen, Z., Fan, S. & Minnich, A. J. Daytime radiative cooling using near-black infrared emitters. *ACS Photonics* **4**, 626-630 (2017).

105   Raman, A. P., Anoma, M. A., Zhu, L., Rephaeli, E. & Fan, S. Passive radiative cooling below ambient air temperature under direct sunlight. *Nature* **515**, 540 (2014).

106   Babulanam, S., Eriksson, T., Niklasson, G. & Granqvist, C. Thermochromic VO2 films for energy-efficient windows. *Solar energy materials* **16**, 347-363 (1987).

107 Karas, D. E., Byun, J., Moon, J. & Jose, C. Copper-oxide spinel absorber coatings for high-temperature concentrated solar power systems. *Solar Energy Materials and Solar Cells* **182**, 321-330 (2018).

108 Kim, T. K. *et al.* Copper-alloyed spinel black oxides and tandem-structured solar absorbing layers for high-temperature concentrating solar power systems. *Solar Energy* **132**, 257-266 (2016).

109 Xu, C. Y., Stiubianu, G. T. & Gorodetsky, A. A. Adaptive infrared-reflecting systems inspired by cephalopods. *Science* **359**, 1495-1500 (2018).

110 Akbari, H., Pomerantz, M. & Taha, H. Cool surfaces and shade trees to reduce energy use and improve air quality in urban areas. *Solar energy* **70**, 295-310 (2001).

111 Lenert, A. *et al.* A nanophotonic solar thermophotovoltaic device. *Nat Nanotechnol* **9**, 126-130 (2014).

112 Park, K. T. *et al.* Lossless hybridization between photovoltaic and thermoelectric devices. *Sci Rep-Uk* **3** (2013).

113 Rinnerbauer, V. *et al.* Metallic Photonic Crystal Absorber-Emitter for Efficient Spectral Control in High-Temperature Solar Thermophotovoltaics. *Adv Energy Mater* **4** (2014).

114 Shin, S.-M., Jung, J.-Y., Park, M.-J., Song, J.-W. & Lee, J.-H. Catalyst-free hydrogen evolution of Si photocathode by thermovoltage-driven solar water splitting. *Journal of Power Sources* **279**, 151-156 (2015).

115 Chen, Z., Zhu, L., Raman, A. & Fan, S. Radiative cooling to deep sub-freezing temperatures through a 24-h day–night cycle. *Nature communications* **7**, 13729 (2016).

116 Krishna, A. & Lee, J. Morphology-Driven Emissivity of Microscale Tree-like Structures for Radiative Thermal Management. *Nanosc Microsc Therm* **22**, 124-136 (2018).

117 Zhu, L., Raman, A. P. & Fan, S. Radiative cooling of solar absorbers using a visibly transparent photonic crystal thermal blackbody. *Proceedings of the National Academy of Sciences* **112**, 12282-12287 (2015).

118 Li, P. *et al.* Large-Scale Nanophotonic Solar Selective Absorbers for High-Efficiency Solar Thermal Energy Conversion. *Advanced Materials* **27**, 4585-4591 (2015).

119   Li, P. *et al.* Boron nitride nanoresonators for phonon-enhanced molecular vibrational spectroscopy at the strong coupling limit. *arXiv preprint arXiv:1801.02897* (2018).

120   Ye, H., Meng, X. & Xu, B. Theoretical discussions of perfect window, ideal near infrared solar spectrum regulating window and current thermochromic window. *Energy and Buildings* **49**, 164-172 (2012).

121   Ye, H., Long, L., Zhang, H. & Gao, Y. The energy saving index and the performance evaluation of thermochromic windows in passive buildings. *Renewable Energy* **66**, 215-221 (2014).

122   Xiao, L. *et al.* Fast adaptive thermal camouflage based on flexible VO2/graphene/CNT thin films. *Nano Lett* **15**, 8365-8370 (2015).

123   Kim, H. *et al.* Flexible thermochromic window based on hybridized VO2/graphene. *ACS nano* **7**, 5769-5776 (2013).

124   Fan, D., Li, Q., Xuan, Y., Tan, H. & Fang, J. Temperature-dependent infrared properties of Ca doped (La, Sr) MnO3 compositions with potential thermal control application. *Applied Thermal Engineering* **51**, 255-261 (2013).

125   Chandrasekhar, P. *et al.* Large, Switchable Electrochromism in the Visible Through Far-Infrared in Conducting Polymer Devices. *Advanced Functional Materials* **12**, 95-103 (2002).

126   Riley, C. T. *et al.* Plasmonic tuning of aluminum doped zinc oxide nanostructures by atomic layer deposition. *physica status solidi (RRL)-Rapid Research Letters* **8**, 948-952 (2014).

127   Kanehara, M., Koike, H., Yoshinaga, T. & Teranishi, T. Indium tin oxide nanoparticles with compositionally tunable surface plasmon resonance frequencies in the near-IR region. *Journal of the American Chemical Society* **131**, 17736-17737 (2009).

128   Mirshafieyan, S. S. & Gregory, D. A. Electrically tunable perfect light absorbers as color filters and modulators. *Sci Rep-Uk* **8**, 2635 (2018).

129   Taylor, R. A., Hewakuruppu, Y., DeJarnette, D. & Otanicar, T. P. Comparison of selective transmitters for solar thermal applications. *Applied optics* **55**, 3829-3839 (2016).

130   Ando, E. & Miyazaki, M. Moisture resistance of the low-emissivity coatings with a layer structure of Al-doped ZnO/Ag/Al-doped ZnO. *Thin Solid Films* **392**, 289-293 (2001).

131   Giovannetti, F., Föste, S., Ehrmann, N. & Rockendorf, G. High transmittance, low emissivity glass covers for flat plate collectors: applications and performance. *Solar energy* **104**, 52-59 (2014).

132   Ohtaki, M., Araki, K. & Yamamoto, K. High thermoelectric performance of dually doped ZnO ceramics. *Journal of Electronic Materials* **38**, 1234-1238 (2009).

133   Hu, J. & Gordon, R. G. Textured aluminum-doped zinc oxide thin films from atmospheric pressure chemical-vapor deposition. *Journal of Applied Physics* **71**, 880-890 (1992).

134   Lu, J. *et al.* Carrier concentration dependence of band gap shift in n-type ZnO: Al films. *Journal of Applied Physics* **101**, 083705 (2007).

135   Ong, K. P., Singh, D. J. & Wu, P. Analysis of the thermoelectric properties of n-type ZnO. *Physical Review B* **83**, 115110 (2011).

136   Naik, G. V., Liu, J. J., Kildishev, A. V., Shalaev, V. M. & Boltasseva, A. Demonstration of Al:ZnO as a plasmonic component for near-infrared metamaterials. *P Natl Acad Sci USA* **109**, 8834-8838 (2012).

137   Pradhan, A. K. *et al.* Extreme tunability in aluminum doped Zinc Oxide plasmonic materials for near-infrared applications. *Sci Rep-Uk* **4** (2014).

138   Fountaine, K. T., Cheng, W.-H., Bukowsky, C. R. & Atwater, H. A. Near-unity unselective absorption in sparse InP nanowire arrays. *ACS Photonics* **3**, 1826-1832 (2016).

139   Wang, Y. *et al.* Spectrally selective solar absorber with sharp and temperature dependent cut-off based on semiconductor nanowire arrays. *Applied Physics Letters* **110**, 201108 (2017).

140   Shi, N. N. *et al.* Keeping cool: Enhanced optical reflection and radiative heat dissipation in Saharan silver ants. *Science* **349**, 298-301 (2015).

141   Zandavi, S. H. *et al.* in *Frontiers in Optics.*   FM4D. 6 (Optical Society of America).

142 Chaudhri, B. P., Ceyssens, F., De Moor, P., Van Hoof, C. & Puers, R. A high aspect ratio SU-8 fabrication technique for hollow microneedles for transdermal drug delivery and blood extraction. *Journal of Micromechanics and Microengineering* **20**, 064006 (2010).

143 Wang, P., Luo, L. & Chung, T.-S. Tri-bore ultra-filtration hollow fiber membranes with a novel triangle-shape outer geometry. *Journal of Membrane Science* **452**, 212-218 (2014).

144 Mayers, B., Jiang, X., Sunderland, D., Cattle, B. & Xia, Y. Hollow nanostructures of platinum with controllable dimensions can be synthesized by templating against selenium nanowires and colloids. *Journal of the American Chemical Society* **125**, 13364-13365 (2003).

145 Ma, T. *et al.* 3D Printed Hollow-Core Terahertz Optical Waveguides with Hyperuniform Disordered Dielectric Reflectors. *Advanced Optical Materials* **4**, 2085-2094 (2016).

146 Liu, S., Li, Y. & Li, N. A novel free-hanging 3D printing method for continuous carbon fiber reinforced thermoplastic lattice truss core structures. *Materials & Design* **137**, 235-244 (2018).

147 Xu, S. *et al.* Assembly of micro/nanomaterials into complex, three-dimensional architectures by compressive buckling. *Science* **347**, 154-159 (2015).

148 Planck, M. *The theory of heat radiation*. (Courier Corporation, 2013).

149 Song, B. *et al.* Radiative heat conductances between dielectric and metallic parallel plates with nanoscale gaps. *Nat Nanotechnol* **11**, 509-514 (2016).

150 Narayanaswamy, A., Shen, S. & Chen, G. Near-field radiative heat transfer between a sphere and a substrate. *Phys Rev B* **78** (2008).

151 Shen, S., Narayanaswamy, A. & Chen, G. Surface Phonon Polaritons Mediated Energy Transfer between Nanoscale Gaps. *Nano Lett* **9**, 2909-2913 (2009).

152 Cui, L. J. *et al.* Study of radiative heat transfer in angstrom ngstrom- and nanometre-sized gaps. *Nat Commun* **8** (2017).

153 Rousseau, E. *et al.* Radiative heat transfer at the nanoscale. *Nat Photonics* **3**, 514-517 (2009).

154   LeGall, J., Olivier, M. & Greffet, J. J. Experimental and theoretical study of reflection and coherent thermal emission by a SiC grating supporting a surface-phonon polariton. *Phys Rev B* **55**, 10105-10114 (1997).

155   Brar, V. W. *et al.* Electronic modulation of infrared radiation in graphene plasmonic resonators. *Nat Commun* **6** (2015).

156   Au, Y. Y., Skulason, H. S., Ingvarsson, S., Klein, L. J. & Hamann, H. F. Thermal radiation spectra of individual subwavelength microheaters. *Phys Rev B* **78** (2008).

157   Ingvarsson, S., Klein, L., Au, Y. Y., Lacey, J. A. & Hamann, H. F. Enhanced thermal emission from individual antenna-like nanoheaters. *Opt Express* **15**, 11249-11254 (2007).

158   Alfaro-Mozaz, F. J. *et al.* Nanoimaging of resonating hyperbolic polaritons in linear boron nitride antennas. *Nat Commun* **8** (2017).

159   Schuller, J. A., Taubner, T. & Brongersma, M. L. Optical antenna thermal emitters. *Nat Photonics* **3**, 658-661 (2009).

160   Ordonez-Miranda, J. *et al.* Anomalous thermal conductivity by surface phonon-polaritons of polar nano thin films due to their asymmetric surrounding media. *J Appl Phys* **113** (2013).

161   Greffet, J. J. *et al.* Coherent emission of light by thermal sources. *Nature* **416**, 61-64 (2002).

162   Fernandez-Hurtado, V., Fernandez-Dominguez, A. I., Feist, J., Garcia-Vidal, F. J. & Cuevas, J. C. Super-Planckian far-field radiative heat transfer. *Phys Rev B* **97** (2018).

163   Thompson, D. *et al.* Hundred-fold enhancement in far-field radiative heat transfer over the blackbody limit. *Nature*, 1 (2018).

164   Hillenbrand, R., Taubner, T. & Keilmann, F. Phonon-enhanced light-matter interaction at the nanometre scale. *Nature* **418**, 159-162 (2002).

165   Golyk, V. A., Kruger, M. & Kardar, M. Heat radiation from long cylindrical objects. *Phys Rev E Stat Nonlin Soft Matter Phys* **85**, 046603 (2012).

166   Wuttke, C. & Rauschenbeutel, A. Thermalization via Heat Radiation of an Individual Object Thinner than the Thermal Wavelength. *Phys Rev Lett* **111** (2013).

167   Agdur, B., Ohman, Y., Sellberg, F. & Boling, G. Scattering, Absorption, and Emission of Light by Thin Metal Wires. *Phys Rev* **130**, 996 (1963).

168   Oehman, Y. Polarized Thermal Emission from Narrow Tungsten Filaments. *Nature* **192**, 254 (1961).

169   Singer, S. B., Mecklenburg, M., White, E. R. & Regan, B. C. Polarized light emission from individual incandescent carbon nanotubes. *Phys Rev B* **83** (2011).

170   De Wilde, Y. *et al.* Thermal radiation scanning tunnelling microscopy. *Nature* **444**, 740-743 (2006).

171   Brites, C. D. S. *et al.* Thermometry at the nanoscale. *Nanoscale* **4**, 4799-4829 (2012).

172   Zhao, Z. W., Wu, H. W. & Zhou, Y. Surface-confined edge phonon polaritons in hexagonal boron nitride thin films and nanoribbons. *Optics Express* **24**, 22930-22942 (2016).

173   Bayer, M. & Forchel, A. Temperature dependence of the exciton homogeneous linewidth in In0.60Ga0.40As/GaAs self-assembled quantum dots. *Phys Rev B* **65** (2002).

174   Pine, A. S. & Tannenwald, P. E. Temperature Dependence of Raman Linewidth and Shift in Alpha-Quartz. *Phys Rev* **178**, 1424 (1969).

175   Palik, E. D. Handbook of Optical Constants of Solids (Academic, Orlando, 1985).

176   Dai, S. *et al.* Tunable phonon polaritons in atomically thin van der Waals crystals of boron nitride. *Science* **343**, 1125-1129 (2014).

177   Li, D. Y. *et al.* Thermal conductivity of individual silicon nanowires. *Appl Phys Lett* **83**, 2934-2936 (2003).

178   Kwon, S., Zheng, J. L., Wingert, M. C., Cui, S. & Chen, R. K. Unusually High and Anisotropic Thermal Conductivity in Amorphous Silicon Nanostructures. *Acs Nano* **11**, 2470-2476 (2017).

179   Zheng, J. L., Wingert, M. C., Dechaumphai, E. & Chen, R. K. Sub-picowatt/kelvin resistive thermometry for probing nanoscale thermal transport. *Review of Scientific Instruments* **84** (2013).

180   Larkin, J. M. & McGaughey, A. J. H. Thermal conductivity accumulation in amorphous silica and amorphous silicon. *Phys Rev B* **89** (2014).

181   Yang, L. *et al.* Ballistic Phonon Penetration Depth in Amorphous Silicon Dioxide. *Nano Lett* **17**, 7218-7225 (2017).

182 Olego, D. & Cardona, M. Temperature-Dependence of the Optical Phonons and Transverse Effective Charge in 3c-Sic. *Phys Rev B* **25**, 3889-3896 (1982).

183 Laroche, M. *et al.* Highly directional radiation generated by a tungsten thermal source. *Opt Lett* **30**, 2623-2625 (2005).

184 Guo, R., Jho, Y.-D. & Minnich, A. J. Coherent control of thermal phonon transport in van der Waals superlattices. *Nanoscale* (2018).

185 Chen, J., Zhang, G. & Li, B. W. Phonon coherent resonance and its effect on thermal transport in core-shell nanowires. *Journal of Chemical Physics* **135** (2011).

186 Mills, A. F. & Coimbra, C. *Basic heat transfer*. (Temporal Publishing, LLC, 2015).

187 Zheng, J. L., Wingert, M. C., Moon, J. & Chen, R. K. Simultaneous specific heat and thermal conductivity measurement of individual nanostructures. *Semicond Sci Tech* **31** (2016).

188 Yang, L. *et al.* Ballistic phonon penetration depth in amorphous silicon dioxide. *Nano Lett* **17**, 7218-7225 (2017).

189 Goodson, K., Flik, M., Su, L. & Antoniadis, D. Prediction and measurement of the thermal conductivity of amorphous dielectric layers. *Journal of Heat Transfer* **116**, 317-324 (1994).

190 Cahill, D. G. Thermal conductivity measurement from 30 to 750 K: the 3ω method. *Review of scientific instruments* **61**, 802-808 (1990).

191 Taflove, A., Oskooi, A. & Johnson, S. G. *Advances in FDTD computational electrodynamics: photonics and nanotechnology*. (Artech house, 2013).

192 Craig, F. B., Bohren, F. & Huffman, D. Absorption and scattering of light by small particles. *Inc: John Wiley & Sons, New York, USA* (1983).

193 Raman, A. P., Anoma, M. A., Zhu, L., Rephaeli, E. & Fan, S. Passive radiative cooling below ambient air temperature under direct sunlight. *Nature* **515**, 540-544 (2014).

194 Kou, J. L., Jurado, Z., Chen, Z., Fan, S. H. & Minnich, A. J. Daytime Radiative Cooling Using Near-Black Infrared Emitters. *Acs Photonics* **4**, 626-630 (2017).

195   Ravichandran, J. *et al.* Crossover from incoherent to coherent phonon scattering in epitaxial oxide superlattices. *Nat Mater* **13**, 168 (2014).

196   Luckyanova, M. N. *et al.* Coherent phonon heat conduction in superlattices. *Science* **338**, 936-939 (2012).

197   Maire, J. *et al.* Heat conduction tuning by wave nature of phonons. *Science advances* **3**, e1700027 (2017).

198   Shin, S., Elzouka, M., Prasher, R. & Chen, R. Far-field coherent thermal emission from polaritonic resonance in individual anisotropic nanoribbons. *Nat Commun* **10**, 1377 (2019).

199   Song, B., Fiorino, A., Meyhofer, E. & Reddy, P. Near-field radiative thermal transport: From theory to experiment. *AIP advances* **5**, 053503 (2015).

200   Kim, K. *et al.* Radiative heat transfer in the extreme near field. *Nature* **528**, 387 (2015).

201   Fiorino, A. *et al.* Giant enhancement in radiative heat transfer in sub-30 nm gaps of plane parallel surfaces. *Nano Lett* **18**, 3711-3715 (2018).

202   Yu, C., Shi, L., Yao, Z., Li, D. & Majumdar, A. Thermal conductance and thermopower of an individual single-wall carbon nanotube. *Nano Lett* **5**, 1842-1846 (2005).

203   Lee, V., Wu, C.-H., Lou, Z.-X., Lee, W.-L. & Chang, C.-W. Divergent and ultrahigh thermal conductivity in millimeter-long nanotubes. *Phys Rev Lett* **118**, 135901 (2017).

204   Xu, X. *et al.* Length-dependent thermal conductivity in suspended single-layer graphene. *Nat Commun* **5**, 3689 (2014).

205   Schwab, K., Henriksen, E. A., Worlock, J. M. & Roukes, M. L. Measurement of the quantum of thermal conductance. *Nature* **404**, 974-977 (2000).

206   Jezouin, S. *et al.* Quantum limit of heat flow across a single electronic channel. *Science* **342**, 601-604 (2013).

207   Cui, L. *et al.* Quantized thermal transport in single-atom junctions. *Science* **355**, 1192-1195 (2017).

208   Chen, D.-Z. A. & Chen, G. Measurement of silicon dioxide surface phonon-polariton propagation length by attenuated total reflection. *Appl Phys Lett* **91**, 121906 (2007).

209   Ordonez-Miranda, J. *et al.* Effects of anisotropy and size of polar nano thin films on their thermal conductivity due to surface phonon-polaritons. *Applied Physics Express* **7**, 035201 (2014).

210   Tiwald, T. E. *et al.* Carrier concentration and lattice absorption in bulk and epitaxial silicon carbide determined using infrared ellipsometry. *Phys Rev B* **60**, 11464 (1999).

211   Caldwell, J. D. *et al.* Atomic-scale photonic hybrids for mid-infrared and terahertz nanophotonics. *Nature nanotechnology* **11**, 9 (2016).

212   Haraguchi, M., Fukui, M. & Muto, S. Experimental observation of attenuated-total-reflection spectra of GaAs/AlAs superlattice. *Phys Rev B* **41**, 1254 (1990).

213   Ordonez-Miranda, J. *et al.* Quantized thermal conductance of nanowires at room temperature due to Zenneck surface-phonon polaritons. *Phys Rev Lett* **112**, 055901 (2014).

214   Chen, D.-Z. A., Narayanaswamy, A. & Chen, G. Surface phonon-polariton mediated thermal conductivity enhancement of amorphous thin films. *Phys Rev B* **72**, 155435 (2005).

215   Hammonds Jr, J. S. Thermal transport via surface phonon polaritons across a two-dimensional pore. *Appl Phys Lett* **88**, 041912 (2006).

216   Zheng, J., Wingert, M. C., Dechaumphai, E. & Chen, R. Sub-picowatt/kelvin resistive thermometry for probing nanoscale thermal transport. *Review of Scientific Instruments* **84**, 114901 (2013).

217   Zheng, J., Wingert, M. C., Moon, J. & Chen, R. Simultaneous specific heat and thermal conductivity measurement of individual nanostructures. *Semiconductor Science and Technology* **31**, 084005 (2016).

218   Wingert, M. C., Chen, Z. C., Kwon, S., Xiang, J. & Chen, R. Ultra-sensitive thermal conductance measurement of one-dimensional nanostructures enhanced by differential bridge. *Review of Scientific Instruments* **83**, 024901 (2012).

219   Larkin, J. M. & McGaughey, A. J. Thermal conductivity accumulation in amorphous silica and amorphous silicon. *Phys Rev B* **89**, 144303 (2014).